Correlations between manganese valence and catalytic oxygen evolution of $Li_xMn_2O_4$

Dissertation

zur Erlangung des mathematisch-naturwissenschaftlichen Doktorgrades
'Doctor rerum naturalium'
der Georg-August-Universität
im Promotionsstudiengang Physik
der Georg-August University School of Science (GAUSS)

vorgelegt von

Max Baumung
aus Göttingen

Göttingen, 2021

Betreuungsausschuss

Dr. Marcel Risch, Institut für Materialphysik und Helmholtz-Zentrum Berlin

Prof. Cynthia A. Volkert, PhD, Institut für Materialphysik

Prof. Dr. Sven Schneider, Insitut für anorganische Chemie

Mitglieder der Prüfungskommssion

Referent: Dr. Marcel Risch, Institut für Materialphysik und Helmholtz-Zentrum Berlin

Korreferentin: Prof. Cynthia A. Volkert, PhD, Institut für Materialphysik

Weitere Mitglieder der Prüfungskommssion

Prof. Dr. Hans-Christian Hofsäss, II. Physikalisches Institut

Prof. Dr. Christian Jooß, Institut für Materialphysik

Prof. Dr. Wolfram Kollatschny, Institut für Astrophysik

Prof. Dr. Vasily Moshnyaga, I. Physikalisches Institut

Tag der mündlichen Prüfung: 28.06.2021

Abstract

This doctoral thesis deals with the mechanistic insights in catalysing the oxygen evolution reaction (OER) in alkaline solution by using a tuneable $Li_xMn_2O_4$ spinel as a model catalyst, motivated by the challenging step to control the OER for the long-time storage of electricity from renewables in chemical energy carriers.

By using a RRDE-setup it was possible to identify the origin of the total electrode current as the sum of the oxygen evolution and the manganese loss at a defined reference potential and could evaluate its impact on the catalytic behaviour for different particle sizes in NaOH (pH 13). The initial observed disk current decay is assigned to the manganese loss reaction while a constant amount of oxygen is detected at the ring electrode. Changing the electrolyte to LiOH reveals a different behaviour of the catalyst as pronounced redox peaks in electrolytes below pH 14 indicates an oxidation by delithiation. This in-situ oxidation during the OER was confirmed by XAS and has an impairing influence on the catalytic activity as implied by the shifted onset of the oxygen detection current to higher overpotentials. In contrast to the initial material, ex-situ delithiated $Li_xMn_2O_4$ particles have a different origin of the total disk current. Thus, the Faradaic efficiency increases from 75(2)% to 96(5)% because of a negligible corrosion process.

These results highlight the meaning of side reaction as they may influence the catalytic activity, as demonstrated in the delithiation reaction, thus it leads to a chemical different catalyst and in contrast to that the manganese loss reaction which has no effect on the OER, however could get negligible which leads to an increase in the Faradaic efficiency. The Faradaic efficiency may help to identify model catalysts, which do not have a significant side reaction current contribution. This could be the pathway to a deeper mechanistic insight, as these catalysts only produced the focused product, and no side reactions may interfere with the OER mechanism.

Zusammenfassung

Diese Doktorarbeit befasst sich mit den mechanistischen Erkenntnissen bei der Katalyse der Sauerstoffentwicklungsreaktion (OER) in alkalischer Lösung unter Verwendung eines einstellbaren $Li_xMn_2O_4$-Spinells als Modellkatalysator. Motiviert durch den herausfordernden Schritt, die OER für die Langzeitspeicherung von Strom aus erneuerbaren Energien in chemischen Energieträgern zu kontrollieren.
Mit Hilfe eines RRDE-Aufbaus war es möglich, den Ursprung des gesamten Elektrodenstroms als Summe der Sauerstoffentwicklung und des Manganverlusts bei einem definierten Referenzpotential zu identifizieren und seinen Einfluss auf das katalytische Verhalten für verschiedene Partikelgrößen in NaOH (pH 13) zu bestimmen. Der anfänglich beobachtete Abfall des Scheibenstroms, wird der Manganverlustreaktion zugeordnet, während eine konstante Sauerstoffmenge an der Ringelektrode detektiert wird. Der Wechsel des Elektrolyten zu LiOH zeigt ein anderes Verhalten des Katalysators, da ausgeprägte Redox-Peaks in Elektrolyten unter pH 14 auf eine Oxidation durch Delithierung hindeuten. Diese Oxidation wurde durch XAS bestätigt und beeinträchtigt die katalytische Aktivität, wie durch den zu höheren Überpotentialen verschobenen Beginn des Sauerstoffdetektionsstroms impliziert wird. Im Gegensatz zum Ausgangsmaterial haben ex-situ delithierte $Li_xMn_2O_4$-Partikel einen anderen Strombeitrag zum Gesamtelektrodenstrom, wodurch die Faraday'sche Effizienz, aufgrund eines vernachlässigbaren Korrosionsprozesses, von 75(2)% auf 96(5)% steigt.
Diese Ergebnisse verdeutlichen die Bedeutung der Nebenreaktion, da sie die katalytische Aktivität beeinflussen können. So kann eine Delithierung z.B. zu einem chemisch anderen Katalysator führen und im Gegensatz dazu die Manganverlustreaktion, die keinen Einfluss auf den OER hat. Dieser Manganverlusst wird mit dem Grad der Delithierung jedoch vernachlässigbar, wodurch die Faraday'sche Effizienz erhöht wird. Mithilfe der Faraday'schen Effizienz können Modelkatalysatoren identifiziert werden, bei denen Nebenreaktionen vernachlässigbar klein sind, um so einen detaillierteren Einblick in die Mechanismen der OER zu erlangen, die nicht durch Nebenreaktionen beeinträchtigt ist.

List of abbreviations

CV	cyclic voltammetry
EC/DMC	ethylene carbonate/ dimethyl carbonate (50:50)
ECSA	electrochemical surface area
EELS	electron energy loss spectroscopy
EXAFS	extended X-ray absorption fine structure
F	Faraday constant
HER	hydrogen evolution reaction
$LiPF_6$	lithium hexafluorophosphate
OEC	oxygen-evolution complex
OER	oxygen evolution reaction
PTFE	polytetrafluoroehylene
RHE	reversible hydrogen electrode
RLS	rate limiting step
RRDE	rotating ring disk-electrode
SEM	scanning electron microscope
TEM	transmission electron microscope
TEY	total electron yield
THF	tetrahydrofuran
XANES	X-ray absorption near-edge structure
XAS	X-ray absorption spectroscopy
XPS	X-ray photoelectron spectroscopy
XRD	X-ray diffraction

Contents

1. Introduction and Motivation

"*Water will be the coal of the future.*" – Jules Vernes 1874

Already more than 145 years ago, Jules Vernes devised a clean and sustainable energy supply base on a hydrogen economy, after the end of a fossil fuel depending era in his science fiction novel *The Mysterious Island*.[1] As a result of climate change and a more and more tense political situation in the oil producing countries, the way to green energy becomes more important. One crucial step in advancing renewable energies is solving the current issue of storage and availability on demand. A suitable possibility to face this challenge, is to chemically store the energy obtained in times of overproduction. A promising application is offered by splitting water into its components hydrogen and oxygen and re-convert them back to electricity in a fuel cell, when there is a demand for energy (Fig. 1.1).[2, 3] Furthermore, this strategy to store energy in hydrogen gas has the advantage of being an option for mobile as well as stationary applications.

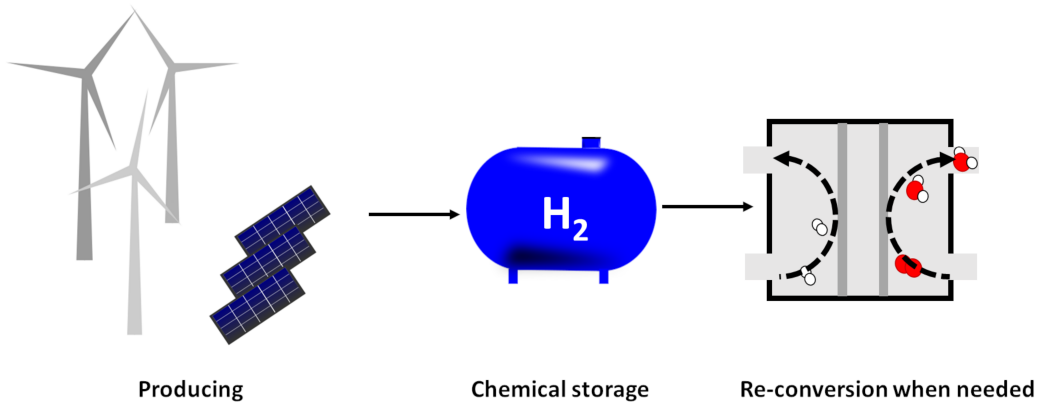

Figure 1.1.: Schematic example for storing green energy from e.g. solar and wind in times of overproduction in hydrogen. The excess electricity is used to split water into its components. Later the stored hydrogen can be re-converted in a fuel cell, when there is a demand in electricity.

Therefore, offering crucial improvement and new steps in regards to energy mobility, off-grid energy supply and a smart electricity grid based on hydrogen economy. However, the electrochemical process of splitting water to produce this energy vector (Eq. 1.1) is thermodynamically limited by the stagnant oxygen evolution reaction (OER). For application use, a catalyst to drive this reaction efficiently in an up-scaled process, needs to be developed. Therefore, we aim to control and mechanistically understand this multi-electron transfer reaction.

$$2H_2O \longrightarrow O_2 + 4H^+ + 4e^- \tag{1.1}$$

The benchmarking transition metal oxides catalysts are RuO_2 and IrO_2 [4, 5], however these metals are rare and therefore expensive. Hence, abundant transition metal oxides are often considered as an alternative. One of these alternatives is manganese, as it has a rich redox chemistry, which influences the catalytic activity due to a tuneable change in electronic properties (e.g. oxidation state) and additional structural properties (e.g. Jahn-Teller distortion).[6]

To compare different catalysts and their activity, their material properties are generalized to a proposed fundamental characteristic (descriptor) that correlate with OER activity. In the past years, a variety of different descriptors and corresponding models have been published, in an effort to predict catalytic activity.[7–12]
The state of the art descriptor model is the e_g occupancy of the 3d orbitals of transition metal oxides, introduced by Suntivich et al.,[10] as these orbitals of the catalyst are involved in the σ-bonds with the absorbed oxygen species of the electrolyte. This model is in good agreement with previous models, which correlate the activity of manganese with the oxidation state.[7–9, 13] However, contradictory results which can not be explained within the descriptors of the e_g occupancy, as shown by Schönewald et al..[14] Here, a change in the e_g occupancy introduced by tetrahedral antisite manganese defects in $LiMn_2O_4$ does not affect the OER activity.

To further investigate this apparent contradiction within different models and descriptors, it is essential to gain mechanistic insights into the catalysis of this multi-electron transfer reaction. The transition metal oxide spinel lithium manganese oxide $Li_xMn_2O_4$ ($0 \leq x \leq 1$) serves as model catalyst. It has the advantage of being a well-studied cathode material for secondary batteries, i.e., material properties, such as the chemical composition and

thereby the manganese valence state can be electrochemically tuned by (de)intercalation without changing the nominal manganese bonding environment.

The goal of this thesis is to gain mechanistic insight into the OER through modification of the model catalyst to unravel the influence of changes of structural and electronic properties on the performance of catalytic water oxidation. Therefore, I propose the following three hypotheses:

1. *The total disk current consists of the sum of at least two specific current contributions — namely the oxygen detection current and the manganese detection current due to manganese loss as a side reaction.*
   This hypothesis addresses the selectivity of a catalyst. It enables to assess the proportion of the main product (here oxygen) in relation to the turnover of the entire catalytic reaction and therefore to describe the catalytic behaviour of the material for each cycle.

2. *An oxidation by delithiation of the volume of $Li_xMn_2O_4$ particles decreases the oxygen detection current at a defined overpotential.*
   This hypothesis deals with a decrease in activity due to an oxidation of the catalyst and under which conditions the catalyst oxidized, i.e., the stability of the catalyst.

3. *The oxidation by delithiation of $Li_{1-x}Mn_2O_4$ increases the Faradaic efficiency due to a negligible current contribution of the manganese detection.*
   This appeals the impact of an oxidation of the catalyst on its selectivity, as an oxidation not only affects the activity but side reactions as well.

To tackle these research goals, the catalytic behaviour of $Li_xMn_2O_4$ in the initial state (x=1), as well as modified particles, on the OER in alkaline solution is evaluated by a rotating ring disk-electrode (RRDE)-setup. This advanced electrochemical setup enables a measurement of activity and stability, i.e. oxygen evolution and corrosion of the catalyst. Pristine as well as electrochemically modified particles (x<1) are characterized by various X-ray and microscopy techniques to correlate the determined properties with the electrocatalytic activity.
In a first step, the activity of two commercial $Li_xMn_2O_4$ powders in their initial state (x=1) with different particle sizes and the apparent influence of particle sizes on the OER were characterized in a sodium hydroxide electrolyte. Within this investigation[15], it was possible to determine the origin of the electrode current. This demonstrates the impact

of side reactions e.g. leaching of manganese on the OER.
To determine the influence of oxidation by delithiation, two different experiments were performed. First, $LiMn_2O_4$ was in-situ delithiated in low concentrated lithium hydroxide electrolyte.[16] Through this, it was possible to establish a model that predicts the stability of the $LiMn_2O_4$ and to correlate it with the catalytic activity. Secondly, $Li_xMn_2O_4$ was ex-situ electrochemically delithiated ($0 \leq x \leq 1$) by battery techniques and the catalytic performance was characterized by RRDE in NaOH. X-ray diffraction (XRD), X-ray absorption spectroscopy (XAS) and transmission electron microscope (TEM) as structural methods are used to correlate the catalytic activity with the manganese valence.

2. Scientific Background

This chapter deals with the scientific background and is divided into three parts. The first part introduces the fundamentals of the oxygen evolution reaction and the challenging aspects of this four-electron transfer reaction. Besides, different proposed mechanisms of the OER are provided. In the second part, an overview over the state of the art of using manganites as a catalyst for the OER is provided to the reader. Especially, focussing on the correlation between catalytic activity and material properties (e.g. e_g occupancy), i.e. descriptors to characterize and predict catalytic activity. Additionally, the here used lithium manganese (III, IV) oxide and its properties, as well as the access to its electronic structure as a control tactic to tune the catalytic activity by (de)lithiation, is introduced. In the end of this chapter, the electrochemical fundamentals, i.e. the governing equations and models as the Nernst equation, the theory of the double layer and its significance for the electrode surface and the fundaments of the kinetics are provided to the reader. Through these governing equations and models, it is possible to gain a mechanistic insight into the OER.

2.1. The Oxygen Evolution Reaction (OER)

When splitting water (Eq. 1.1) into its components hydrogen and oxygen, two half reactions arise. The reduction of in water bonded hydrogen from oxidation state +1 to neutral — the so called hydrogen evolution reaction (HER) (Eq. 2.1) — occurs at the cathode.

$$2H_2O + 2e^- \rightleftharpoons H_2 + 2OH^- \tag{2.1}$$

In the HER the energy vector (hydrogen) which is needed for storing and re-converting is produced. In order, to ensure charge neutrality of the water splitting reaction, another half reaction is needed: the anodic oxygen evolution reaction, in which the oxygen of a hydroxide molecule (in alkaline solutions) is oxidized from oxidation state -2 to

neutral.[17]

$$4OH^- \rightleftharpoons O_2 + 2H_2O + 4e^- \tag{2.2}$$

The theoretical thermodynamic potential, at which the OER (Eq. 2.2) appears, amounts to 1.23 V vs. the reversible hydrogen electrode (RHE). However, the additional needed potential to overcome the thermodynamic and kinetic limitation, i.e. the overpotential (η) causes a higher overall potential to drive this reaction (Fig. 2.1). This overpotential of the OER (η_{OER}=0.4 V)[18] is almost twice the needed overpotential of the HER (η_{HER}=0.2-0.3 V).[19]

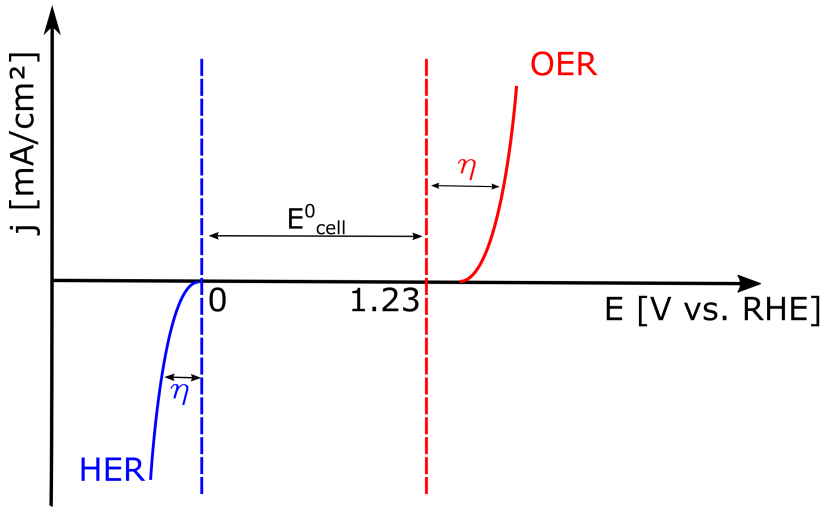

Figure 2.1.: Polarisation curve of the HER and the OER. The overpotential η is needed to reach the same current density in each reactions.

As both reactions arise at the same time, the OER limits the turnover of the entire water splitting reaction, which makes this half reaction the rate limiting step.[20–22] Thus, the use of catalysts to lower the needed potential for the OER is worthwhile and requires a fundamental understanding of the limiting half reaction — the OER.

2.2. Mechanism for the OER

As introduced in the previous chapter 2.1, two half cell reactions — namely the OER and HER — are involved in the water splitting reaction. For the OER (Eq. 2.2), four electrons have to be transferred in four separate reaction steps.[23] Different mechanisms

are discussed in literature. For oxide spinels, like the here used $LiMn_2O_4$, Sun et al.[12] proposed an *oxygen absorption mechanism*, shown in figure 2.2.

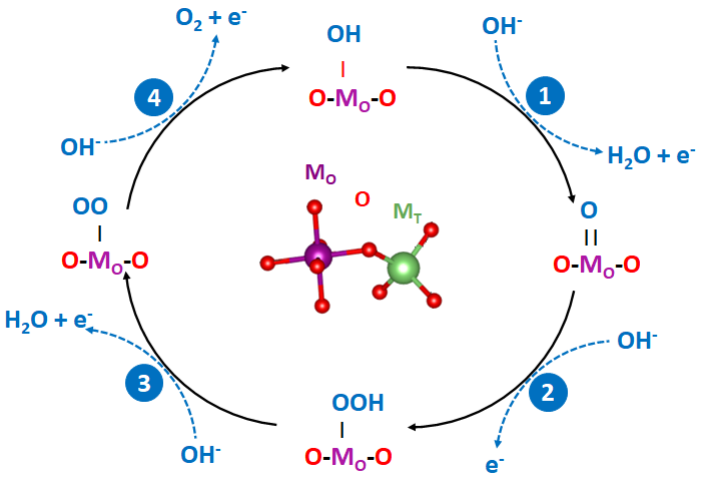

Figure 2.2.: (a) Schematic cycle of absorption mechanism explicitly for transition oxide spinels as described by Sun et al.[12]. For this class of catalyst, the octahedral coordinated (M_O) sites are identified as catalytically active [24]. Figure adopted and reproduced with permission from [12]. M_T-O-M_O lattice motif visualized by Vesta.[25]

In the proposed mechanism, a hydroxyl ion (OH^-) of the electrolyte is absorbed by the metal center, forming a hydroxyl.

$$4OH^- \rightleftharpoons 3OH^- + OH^* + e^- \tag{2.3}$$

In the next step, the absorbed hydroxyl ion deprotonates, while another hydroxyl ion accepts this proton by forming water (Eq. 2.4).

$$3OH^- + OH^* + e^- \rightleftharpoons O^* + H_2O + 2OH^- + 2e^- \tag{2.4}$$

In the third step, the absorbed oxygen absorbs another hydroxyl ion by forming a peroxide (Eq. 2.5).

$$O^* + H_2O + 2OH^- + 2e^- \rightleftharpoons OOH^* + H_2O + OH^- + 3e^- \tag{2.5}$$

In the final step, this absorbed peroxide deprotonates and oxygen releases from the cata-

lyst's surface (Eq. 2.6).

$$OOH^* + H_2O + OH^- + 3e^- \rightleftharpoons O_2 + H_2O + 4e^- \tag{2.6}$$

Throughout this proposed sequence the valance state of the metal cation changes between +3 and +4.[12, 26, 27]

Besides the *oxygen absorption mechanism*, other mechanisms like the *oxygen coupling mechanism* by Bockris[28] or the *oxygen vacancy mechanism* proposed by Wohlfahrt et al.[29] are known. These three mechanisms are mostly discussed in the context of perovskite catalysts.[30]

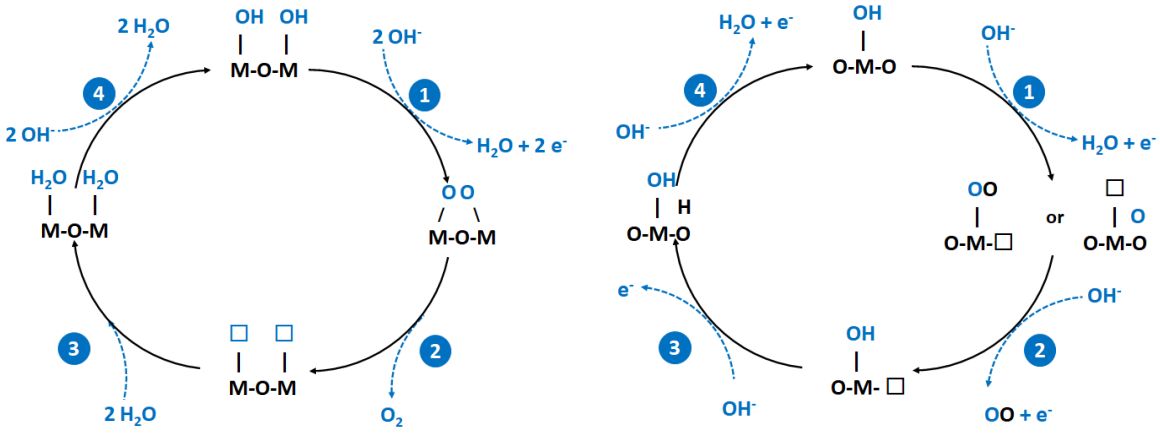

(a) (b)

Figure 2.3.: (a) Schematic cycle of the oxygen coupling mechanism and (b) the oxygen vacancy mechanism.

In the oxygen coupling mechanism (Fig. 2.3a) two neighbouring metals are bonding hydroxyl ions of the electrolyte. These hydroxy groups are deprotonated to form water. In the next step the remaining bonded oxygen are coupling and forming molecular oxygen which is detached from the catalyst causing vacant sites at the metal. In the following step theses vacancies are occupied by water, which is deprotonated to form a hydroxy group. In this proposed mechanism manganese would be oxidized from +3 to +4 and reduced to +2.[28, 31]

For the oxygen vacancy mechanism (Fig. 2.3b), the initial situation is the same as in

the absorption mechanism. A hydroxyl ion is absorbed by the metal and is deprotonated. However, in the next step two different intermediate states are possible: an oxygen of the catalyst is forming an OO species at the metal center resulting in an oxygen vacancy in the oxide structure or the absorbed oxygen is forming the OO species directly at the catalyst, i.e. by forming a vacancy at the metal. In the next step molecular oxygen is evolved and a hydroxyl ion is replacing one vacancy. Another hydroxyl ion is replacing the other vacancy in the following step. Finally, the oxygen atom of the oxide structure is deprotonated.[29, 32]

Independent of the proposed mechanism, all OER cycles involve the absorption of hydroxyl from the electrolyte, the formation of intermediates to lower energy barriers, the formation of oxygen bonds and finally the release of oxygen,[30] However, only one of these reaction steps is the rate limiting step. Therefore, the properties of the catalyst and its environment are crucial.
For the reaction intermediates (Eq. 2.3-2.6), there is the theory of *scaling relationships*, which relates the binding energies of these intermediates across the catalyst's surface.[23, 33, 34] Recently, it has been shown by DFT calculation, that there is a linear scaling relationship between the binding energies of the reaction intermediates OH^*, OOH^* (Eq. 2.3 and 2.5) and O^* (Eq. 2.6) on the catalyst's surface. This indicates, that there is only one parameter which determines the OER activity.[35]

2.3. State of the art for manganites as catalysts for the OER

Due to their electronic properties, transition metal oxides are widely discussed for technical applications as catalysts for water splitting.[36] The benchmark electrode materials are IrO_2 and RuO_2, however these electrode materials contain of precious elements, which drawbacks its usage in up-scaled processes.[37]

Hence, 3d metal oxides — especially cobalt oxides — are studied as an alternative. However, because of cobalt's toxicity and high price, manganese oxides get more and more attractive due to their high abundance, which makes them cost effective.[38] The most eminent transition metal catalyst for the OER is Mn_4CaO_5, as it is the oxygen-evolution complex (OEC) in natural photosynthesis.[39] In the past years, Mn_3O_4, Mn_2O_3 and

MnO_2, as well as derivatives of that, which contain redox-inactive cations (e.g. $LiMn_2O_4$ chapter 2.4), get more attention.

To evaluate the catalytic activity of different materials and to generalize these finding, proxies which describe e.g. structural or electronic properties are used and correlated with the OER activity. The used proxies — in the following *descriptors* — changed in the last years, as new insights in fundamental mechanisms of catalysis arose.

From a chronological perspective, starting in the 1970s, the *oxidation state* was used as a descriptor for the catalytic activity, when Shafirovich et al.[13] postulated a correlation between the manganese valence state and its catalytic performance. Thereby, they realized the advantage of manganese as a catalyst, as it is capable to change its oxidation state from Mn^{2+} to Mn^{7+} by five units. For manganese oxides, Takashima et al.[7, 8] identified Mn^{3+} as starting state for the OER and thereby the most active manganese valence state. This discovery of the catalytic most active state is crucial as Mn^{3+} is only stable in an alkaline environment and would disproportionate into Mn^{2+} and Mn^{4+} in electrolytes with a pH<9.[7, 8]
Ramirez et al.[9] investigated the catalytic activity of Mn^{3+} (α-Mn_2O_3) and mixed manganese valence states $Mn^{3+/4+}$ (MnO_x) and $Mn^{2+/3+}$ (Mn_3O_4), where the highest activity was indeed observed for Mn^{3+}, which is in agreement with other later studies. [7, 8, 10] They were able to identify $Mn^{2+/3+}$ as the least active manganese species in their study, which the authors explain by additional *structural properties* like different Mn-O bonding distances.

The concept to use the electronic property of a catalyst as a descriptor was later refined and modified by Sunitivich et al.[10], who uses the *occupancy of the 3d e_g orbital* of perovskite transition metal oxides as a descriptor for OER activity. As the e_g orbitals of the transition metals at the surface are involved in the σ-bonds with the absorbed oxygen species of the electrolyte (e.g. OH^-), they predict the maximum OER activity for oxides with an e_g occupancy close to one, i.e. the OER activity increases continuously up to an e_g occupancy of one and decreases for higher e_g occupancies. In case of manganese, these findings correspond with a predicted highest activity at an oxidation state of +3 and a decrease in activity for higher or lower oxidation states, which basically coincides with the prediction that the manganese valence state serves as a descriptor.[7–9]

The catalyst with perovskite crystal structure used in the study of Sunitivich et al.[10] has the general formula ABO_3. Here, the A-cation is either a rare-earth metal in an oxidation state of +3 or an alkaline earth metal in oxidation state of +2. The B-cation is a transition metal, which bonds with the oxygen ligands in an octahedral configuration. Therefore, the manganese valence state systematically vary with chemical composition without drastic changes in the structure.[10, 21, 38, 40, 41]

Using epitaxial (100) oriented $La_{0.6}Sr_{0.4}MnO_3$ (LSMO) thin films on Nb-doped SrTiO3 substrates, Scholz et al.[42] could correlate the concentration of manganese surface atoms with the activity. Thus, manganese could be clearly identified as the active site of these LSMO films. For $Pr_{1-x}Ca_xMnO_3$ (PCMO) Mierwaldt et al.[40] illustrated that calcium doping does not cause a mixed manganese valence of $Mn^{3+/4+}$ rather than an intermediate $Mn^{3+\delta}$ state, which emphasises a covalence contribution.[43]

Recently the model of Suntivich et al.[10] was adopted and modified for catalysts with spinel structure by Wei et al.[44]. In their study, they used the e_g occupancy as a descriptor and extended this model to the *e_g occupancy of the octahedral sites*, as these are the catalytically active sites. They predicted the highest OER activity for an e_g occupancy of these octahedral sites of about one and a decrease in the activity for higher or lower occupancies. This is explained by a reduced proton removal of absorbed OOH^- for low filled e_g orbital (e_g <1) and a retard formation of O-O bonds for higher filled e_g orbital (e_g >1) during the catalytic cycle.
The concept of Sun et al.[12] considers *electronic properties* of the investigated spinel structures, namely the covalence of the *structural* M_T-O-M_O lattice motif, as it is responsible for the possibility of bond breaking and subsequent absorption of a hydroxyl ion of the electrolyte to start the catalytic cycle (Fig. 2.2). Therefore, they correlated the OER activity with the covalency, which was quantified by the energy difference between the centers of the metal d and oxygen p bands and used this energy difference as descriptor. For small energy differences Sun et al. assumed a strong covalency, which makes a bond breakage to create an active site unlikely and therefore causes a less active catalyst. On the other hand, a low covalency due to a high energy difference, which results in an insufficient overlap, leads to easy bond breaking and a formation of highly polar new bonds. Therefore, Sun et al. identified a moderate energy difference between the metal d to oxygen p bands of around 3 eV as an optimum for highly active catalysts. Even if the impact

of covalence was discussed in a focused way and proven by simulations and experiments, to develop this model to predict the activity of spinel oxides on the OER — the influence of covalence was already mentioned as a requirement by Suntivich et al.[10] and their e_g occupancy descriptor model.

In previous studies, the use of $LiMn_2O_4$ as a catalyst for the OER is controversily discussed. Cady et al.[45] investigated the electrocatalytic properties of different spinel nanocrystals in 1 M sodium hydroxide. In their study it was not possible to demonstrate a catalytic activity of $LiMn_2O_4$ which could be explained by the high concentration of Nafion as binder on the electrode surface which probably sealed the electrocatalytic active surface with this polymer, thus no electron transfer to the electrolyte was possible. In contrast, other studies proved the catalytic activity of $LiMn_2O_4$.[46–49] Even if Robinson et al.[47] characterized $LiMn_2O_4$ not as a catalyst for the OER, they investigated the cubic spinel structure of λ-MnO_2 by delithiating $LiMn_2O_4$ in nitric acid and used it successfully as OER catalyst. Furthermore, they suggested the strategy to actively change the chemical composition of $LiMn_2O_4$. Köhler et al.[48] performed a pH dependent investigation of nano-sized $LiMn_2O_4$ in sodium hydroxide. They showed, that the material is capable of being used as catalyst for the OER and compared their results with the active site of photosystem II of the plants to gain mechanistic insights.
In the study of Wei et al.[24] $Li_xMn_2O_4$ with x=0.74 and x=1 was investigated as a catalyst for the OER and confirmed the correlation between activity and manganese valence state. Karakya et al.[37] further optimized $LiMn_2O_4$ electrodes for the OER by incorporating additional cobalt to the structure, which improved the kinetics of the catalysed OER. They explained their findings by an "electronic synergy" between cobalt and manganese, as both provide two electrons for the water splitting reaction.

The latest study, which was focused on $LiMn_2O_4$ and the use of descriptors by Schönewald et al.[14] provided a critical insight in the usage of descriptors. They discovered by STEM-EELS a core-shell structure of the nano-sized particles with a reduced shell with respect to the core. This reduced shell vanishes after catalysing the OER in alkaline solution, i.e., the surface was oxidized during the OER. However, this has no impact on the catalytic activity, which contradicts the previous mentioned descriptor models. By using EELS simulations, the reduced shell could be identified as an antisite manganese defect, in which manganese is coordinated in the tetrahedral sites. This tetrahedral coordinated

manganese is catalytically inactive and acts as electron donor similar to lithium. Surprisingly, a change in the e_g occupancy introduced by this tetrahedral coordinated manganese has no impact on the OER activity. This emphasizes, that the e_g occupancy is not the only characteristic which influences catalytic activity. Therefore, it is not suitable as a universal OER descriptor.

2.4. Lithium manganese oxide as a model for the OER

This section introduces the here used model material: $Li_xMn_2O_4$. In the first subsection, the structure and its meaning for the OER is presented. Afterwards, in the second subsection the possibility of tuning the composition of $LiMn_2O_4$ by battery techniques is explained, as this allows a direct access to the electronic structure and therefore an access to the catalytic activity as predicted in literature as mentioned in the previous chapter (chapter 2.3).

2.4.1. Structure of the initial $LiMn_2O_4$

Lithium manganese (III, IV) oxide is an inorganic transition metal oxide. In the initial state, it has the stoichiometric composition $Li_1Mn_2O_4$ and has a cubic spinel structure (Fd3m) (Fig. 2.4) with lattice constant of 8.2476 Å at room temperature.[50, 51] In this lattice structure lithium resides in oxygen tetrahedrons and manganese resides in oxygen octahedrons.

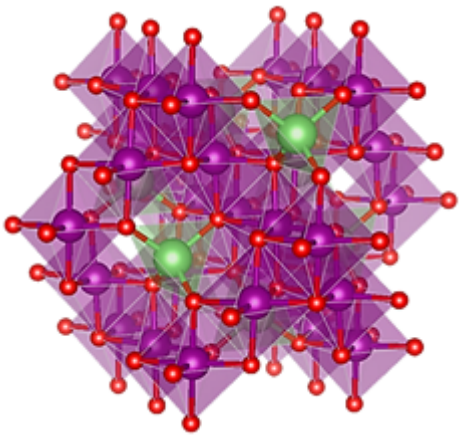

Figure 2.4.: Cubic spinel lattice structure of $Li_1Mn_2O_4$ with manganese in purple, lithium in green and oxygen in red (visualized by Vesta [25])

In the initial state within the bulk, $LiMn_2O_4$ reveals a mixed manganese valences of Mn^{3+} and Mn^{4+}, thus an average manganese valence of +3.5.[52] The cubic lattice motif of $Li_1Mn_2O_4$ is similar to the OEC ($CaMn_4O_5$) of the photosystem II (PSII). $CaMn_4O_5$ is well studied as catalyst for the OER and often used as a blueprint for solar fuel catalysts.[2] By changing the stoichiometric lithium content of this manganese oxide it is possible to access the electronic properties of the material as demonstrated in the following chapter 2.4.2.

In this thesis, a commercial nano-sized $LiMn_2O_4$ powder from Sigma-Aldrich (725129-25G, Lot# MKCF4145) as starting material was used. The particle size is specified with <0.5 μm by the manufacturer. The exact particle distribution is shown in chapter 4. All experiments concerning nano-sized material are done with starting material from the same batch, which was stored at room temperature under environmental conditions.

2.4.2. Tailoring the electronic and chemical structure of $LiMn_2O_4$

As introduced in chapter 2.3, the electronic properties, independent of the used descriptor model, have a tremendous impact on a catalyst's activity. The advantage of $Li_xMn_2O_4$ as a model catalyst for OER is that these properties are electrochemically easily accessible, as it is a well-known cathode material for lithium-ion batteries. Through this, it is possible to remove and insert lithium from the material and thereby control the electronic structure of manganese, i.e., the valence state of manganese form Mn^{3+} to Mn^{4+}.

Additionally, the local manganese structure of this compound remains unchanged throughout the whole tuneable window, as manganese remains coordinated in oxygen octahedrons for $Li_xMn_2O_4$ ($0 \leq x \leq 2$) as illustrated in figure 2.5. This control tactic to change the chemical composition and therefore the manganese valence state of this material by (de)lithiation, is well studied in the field of battery research.[53–57]

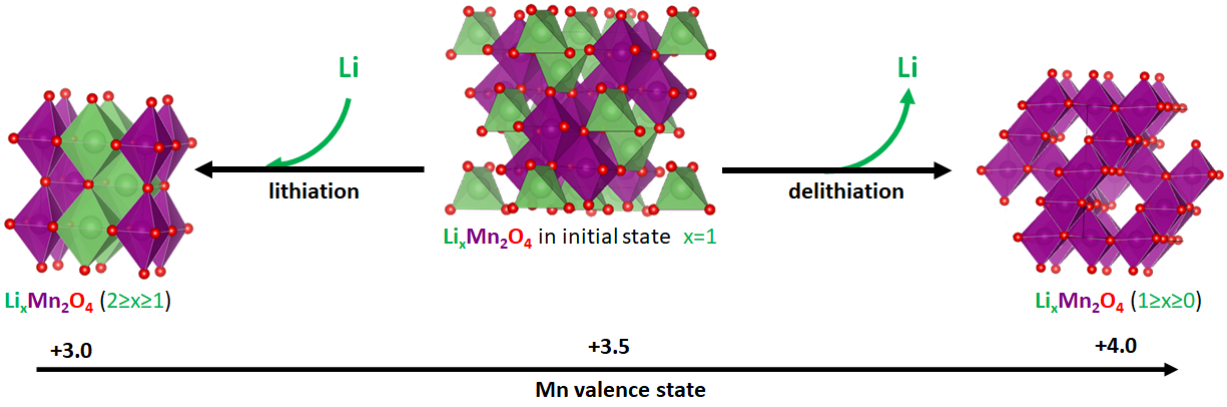

Figure 2.5.: Crystal structures of $Li_xMn_2O_4$: changing the chemical composition by (de)lithiation of the initial material (middle). The lithiation of the material changes the crystal structure from cubic spinel to the tetragonal spinel structure (left), however, the local neighborhood structure of manganese remains unchanged i.e. manganese remains coordinated in an oxygen octahedron (purple). By this change in the chemical composition, the manganese valence state can be tuned between Mn^{3+} and Mn^{4+} (structure visualized by Vesta [25]).

It is referred to (de)intercalation (lat. *intercalare* for insert), as it describes the electrochemically insertion and extraction of small ions — in this case lithium — in a host material or the extraction from it.

Lithium manganese oxide is a two phase system.[52] For the deintercalation reaction ($0 \leq x \leq 1$) of the initial material $Li_1Mn_2O_4$, the material remains in the cubic spinel structure. There is some evidence in the literature for a charge and lithium ordered intermediate phase at around x=0.5.[52, 58] The product of extracting all lithium is λ-MnO_2, in which manganese and oxygen occupy their initial sites in the spinel structure with empty tetrahedral sites.[59]

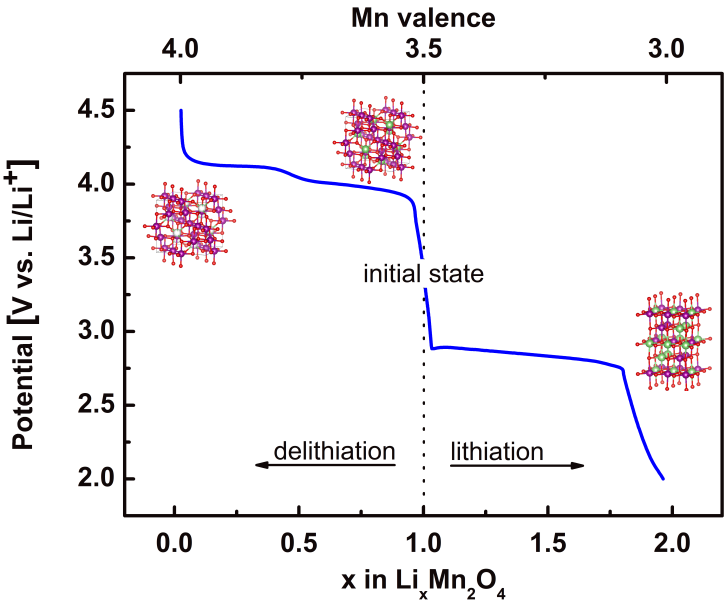

Figure 2.6.: (Dis)charging curve of a battery cell, which performs a C/5 rate using $LiMn_2O_4$ as active material (EC/DMC electrolyte). Charging by delithiation from initial state (left part), discharging by lithiation from initial state (right part). Lattice structures visualized by Vesta[25]

The delithiation reaction occurs by applying a positive current to the material, which results in a cell potential between 3.6 V and 4.3 V vs. Li/Li^+ (Fig. 2.6) and can be written as:

$$Li_1Mn_2O_4 \rightleftharpoons Li^+ + 2\lambda\text{-}MnO_2 + e^- \tag{2.7}$$

The material remains in the spinel phase[57] and a shrinkage of the lattice constant proportional to the lithium content from 8.245 Å (x=1) to 8.029 Å (x=0) is observed.[60] The behaviour of $0 \leq x \leq 1$ is consistent to a single phase. The small potential step in the charging profile at x= 0.5 is likely an indication of a charge ordered phase (Fig. 2.6).[52, 58]

The intercalation of lithium ($1 \leq x \leq 2$) into the initial material $Li_1Mn_2O_4$ occurs at lower potentials around 3 V vs. Li/Li^+ by applying a negative current. The reaction can be written as (Eq. 2.8).

$$Li_1Mn_2O_4 + Li^+ + e^- \rightleftharpoons Li_2Mn_2O_4 \tag{2.8}$$

This intercalation reaction of lithium into the structure causes a first-order phase transition from a cubic spinel to a tetragonal spinel of lithium manganese (III) dioxide.[52] In this process the manganese valence changes from $Mn^{3.5+}$ to Mn^{3+}. In this regime, the potential is almost constant for a large lithium content window (Fig. 2.6), consistent with the expected behavior for a two phase system.[61]
Besides, this phase transition causes a significant potential drop at x=1 in the charging curve (Fig. 2.6), as it entails structural and chemical changes, e.g. Jahn-Teller distortions, a lithium site shift and additional manganese antibonding electron.[52]
As indicated by the arrows, both reactions (Eq. 2.7 and 2.8) are reversible and represent the principle of a charging/discharging process of a secondary battery using $LiMn_2O_4$ as active material.

2.5. Electrochemical fundamentals and characteristics

To complement the scientific background of this thesis, the following section introduces the electrochemical fundamentals and characteristics to the reader. It explains the model of *double layer* of the electrode-electrolyte interface and the meaning of its capacity and the resulting electrochemical surface area (ECSA). Moreover, the concentration dependency on the potential, which is described by the *Nernst equation*, is presented. In the final part of this section, the electrochemical kinetics describe by the *Butler-Volmer equation*, as well as the *Tafel equation* as a simplification of the Butler-Volmer equation and the *reaction rate* are considered.

2.5.1. The electrode-electrolyte interface: the double layer

The model of the *double layer* describes the interface and the potential difference between the electrode and the electrolyte (solid phase and liquid phase) and consists of two layers: a positively charged electrode and a layer of negatively charged ion of the solution or vice versa.

The structure of this double layer and the potential distribution is describted in different models. The first and simplest model by *Hermann von Helmholtz* assumed[17, 62], that solvated ions are located along the electrode surface and that the solvating molecules keep the ions on a defined distance to the electrode: the *outer Helmholtz plane*. In this model the potential drop between the electrode and the outer Helmholtz layer is assumed as

linear and neglects any Brownian motion of the ions.

This motion was taken into account in an extended model by *Louis Georges Gouy* and *David Leonard Chapman* introduces the diffuse layer[17, 63, 64], in which the local concentration of the ions decreases with the distance to the electrode until it equals the electrolyte concentration of the volume. Neither the *Helmholtz* model nor the *Gouy-Chapman* model describes the real double layer behaviour as the Helmholtz layer is too focused on the stability of the compact layer and the model of *Gouy-Chapman* neglects it. The *Stern* model (Fig. 2.7) combines these two models.[17, 65]

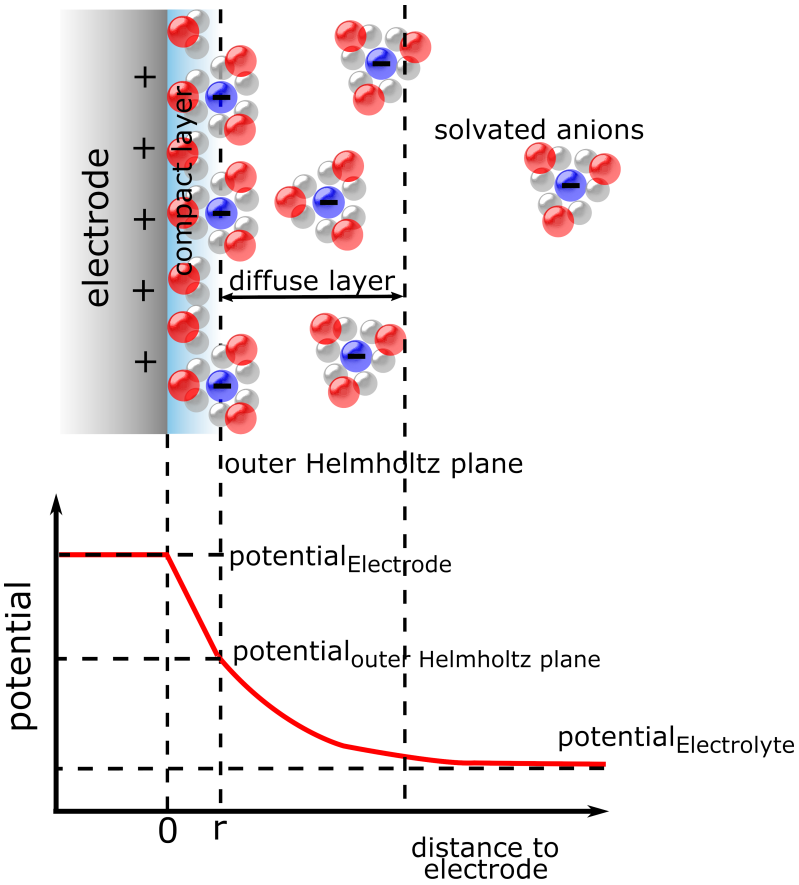

Figure 2.7.: Stern model of the double layer combines the compact layer at the electrode surface of the Helmholtz layer and the diffuse layer of the Gouy-Chapman model. Below: the potential distribution of the Stern model with respect to the electrode surface. Figure modified from [17].

The importance of this double layer is that it influences the overpotential of a reaction,

as a charge has to overcome this double layer at the electrode-electrolyte interface.

2.5.1.1. Double layer capacity

The double layer behaves in a simplified model like a plate capacitor, with the capacity C, charge Q and the voltage U as written in equation 2.9.[17]

$$C = \frac{Q}{U} \tag{2.9}$$

Transferring the behaviour of this electronic device to the electrical double layer Q corresponds to the total charge density σ^M and U to the total potential difference between electrode and electrolyte — the so called Galvani potential $\Delta\phi$ — as written in equation 2.10.

$$C = \frac{\sigma^M}{\Delta\phi} \tag{2.10}$$

Consequently, a constant capacity would imply that the compact layer remains unchanged if the external potential is changed. (Fig. 2.7). In reality there is no exact proportional behaviour between σ^M and $\Delta\phi$, as changes of the electrode potential influences e.g. the orientation of the solvated ions. Hence, the change of σ^M ($\mathrm{d}\sigma^M$) by changing the electrode potential by $\mathrm{d}\phi$ depends on the starting potential $\mathrm{d}\sigma^M(\phi)$. Therefore, the differential quotient (Eq. 2.11) is more suitable to describe the charging behaviour of the double layer.[17]

$$C_{DL} = \frac{d\sigma^M}{d\phi} \tag{2.11}$$

Thus, the double layer capacity can be deduced from the current by applying a linear potential increase ($\frac{d\phi}{dt}$) (scan rate) to the electrode.

$$i_C = C_{DL}\frac{d\phi}{dt} \tag{2.12}$$

The experimental determination of the double layer capacity is described in chapter 4.4.4.

2.5.1.2. The electrochemical surface area — ECSA

One important aspect to evaluate the catalytic activity is to normalize the electrode current to the electrode surface, which defines the electrode current density.[66] As illustrated in figure 2.8 there are different definitions of surface areas and techniques to determine

these areas.[66–69] The easiest way is to calculate the current density form the geometry of the electrode surface (Fig. 2.8a), however this method neglects the true surface morphology like roughness, porosity or particle size of the catalytic material (Fig. 2.8b).[70]

(a) (b)

Figure 2.8.: (a) An ideal surface of a catalyst on top of a supporting electrode e.g. a glassy carbon electrode, also called geometric surface as it is only taking into account to macroscopic surface area (b) the electrochemical surface area (ECSA) considering the electrode surface morphology e.g. different particles forming the electrode surface and thereby the interface to the electrolyte.

As mentioned in the previous section, this surface is well represented by the interface of the electrode and the electrolyte. Hence, the double layer capacity C_{DL} [F] (Eq. 2.12) could be used as representation of the real surface area corrected by the specific capacity $c_{sp.}$ [F/cm^2]as shown in equation 2.8.

$$A_{ECSA} = \frac{C_{DL}}{c_{sp.}} \tag{2.13}$$

Besides, there are other techniques to determine the catalytic surface area as well, e.g.by gas absorption (BET-theory) or by microscopy like scanning electron microscope (SEM) and atomic force microscopy.[70]

2.5.2. The redox potential: Nernst equation

In an electrochemical cell, the potential depends on the ionic concentration of the redox pairs and is given by the *Nernst equation* (Eq. 2.19).[17, 71]

Introducing an electrode into an electrolyte establishes an equilibrium potential, if the electrolyte contains of a redox pair as demonstrated in equation 2.14. For this redox couple A_{ox} represents the oxidized species, which can be reduced to A_{red} by accepting z electrons.

$$A_{ox} + z\ e^- \rightleftharpoons A_{red} \tag{2.14}$$

As a result of this potential a double layer (chapter 2.5.1) at the electrode interface is formed and forming an electrochemical equilibrium. Under assumption of the equilibrium conditions of exchanged electrons gives:

$$\mu_s - \mu_e = 0 \tag{2.15}$$

Therefore, the electrochemical potential in the electrolyte and the electrode/catalyst has to be equal for an exchange of electrons

$$\Delta\phi_0 = \phi_e - \phi_s = \frac{\mu_s - \mu_e}{F} - \frac{RT}{F}\ln(a_s) \tag{2.16}$$

With the Faraday constant (F), universal gas constant (R) and the absolute temperature (T). Using the law of mass action gives the activity of the electrons of the electrolyte.

$$K_\alpha = \frac{a_{ox} \cdot a_s^n}{a_{red}} \tag{2.17}$$

Converting equation 2.17 to a_s

$$a_s = \left(K_\alpha \frac{a_{red}}{a_{ox}}\right)^{\frac{1}{n}} \tag{2.18}$$

The Nernst equation 2.19 is a result of summarizing all terms, which depends on the concentration to E^0.

$$E = E^0 + \frac{RT}{zF}\ln\left(\frac{a_{ox}}{a_{red}}\right) \tag{2.19}$$

At room temperature (T=298 K) equation 2.19 can be simplified to equation 2.20.

$$E = E^0 + \frac{0.059\ V}{z}\log\left(\frac{c_{ox}}{c_{red}}\right) \tag{2.20}$$

2.5.2.1. Nernst equation for the oxygen evolution reaction

For the here investigate OER, the Nernst equation can be written as illustrated in Eq. 2.25. In the following, the derivation of the Nernst equation for the OER. As indicated in the reaction equation (Eq. 2.21) by the present of H_3O^+, this reaction dependent on the pH.

$$6H_2O \rightleftharpoons O_2 + 4H_3O^+ + 4e^- \qquad E^0 = 1.23\ \text{V} \tag{2.21}$$

At room temperature (289 K), this four electrons reaction can be applied to the Nernst equation 2.20 as shown in equation 2.22.

$$E_{OER} = 1.23\ \text{V} + \frac{0.059\ \text{V}}{4} \log\left(\frac{c^4(H_3O^+)c(O_2)}{c^6(H_2O)}\right) \tag{2.22}$$

As there is an excess of water in the electrolyte, which remains constant, it can be neglected. For oxygen at ambient pressure it can be assumed as c(O_2)=1. Thereby, the logarithm only depends on the concentration of H_3O^+.

$$E_{OER} = 1.23\ \text{V} + 0.059\ \text{V} \cdot \log\ c(H_3O^+) \tag{2.23}$$

As the pH is defined as the negative decimal logarithm of the concentration of H_3O^+ (Eq.2.24), equation 2.23 can be simplified.

$$pH = -\log\ c(H_3O^+) \tag{2.24}$$

This simplification leads to the Nernst equation for the OER, as shown in equation 2.25.

$$E_{OER} = 1.23\ \text{V} - 0.059\ \text{V} \cdot pH \tag{2.25}$$

2.5.2.2. Nernst equation for the delithation of $LiMn_2O_4$ in aqueous solution

Since $LiMn_2O_4$ can be delithiated in lithium hydroxide electrolytes, a theoretical model, based on the Nernst equation, to predict the stability of the catalyst in this electrolyte in dependence of the applied potential and electrolyte concentration was established. This model is illustrated by equation 2.45. In the following, this equation is derived.

The (de)lithiation of $LiMn_2O_4$ in aqueous solution — namely lithium hydroxide electrolyte— was already investigated by Li et al.[55], as they built a lithium-ion battery cell. In equilibrium, when no lithium is extracted from $LiMn_2O_4$ and solved in water can be written

as in equation 2.26.

$$Li_{1-x}Mn_2O_4 + H_2O \rightleftharpoons Li^+ + OH^- + \frac{1}{2}H_2 \tag{2.26}$$

During this reaction (Eq. 2.26) molecular hydrogen from water is evolved at the platinum counter electrode (under standard conditions e.g. 1 bar), while lithium hydroxide is formed by the removed lithium from $LiMn_2O_4$ in this aqueous environment. The half cell reaction can be expressed with respect to the RHE-scale, as standard potentials and the depends of the pH (Eq. 2.29 and 2.32) are considered.

The delithiation in aqueous solution as shown in reaction equation 2.26 can be written as potential, which leads to

$$\mu_{Li}^{intercal.} + \mu_{H_2O}^0 = \mu_{Li^+} + \mu_{OH^-} + \frac{1}{2}\mu_{H_2}^0 \tag{2.27}$$

The potentials of Li^+ and OH^- depend on the concentration and are accessible by the Nernst equation (Eq. 2.28 and 2.29).

$$\mu_{Li^+} = \mu_{Li^+}^0 + \frac{RT}{F}\ln(Li^+) \tag{2.28}$$

$$\mu_{OH^-} = \mu_{OH^-}^0 + \frac{RT}{F}\ln(OH^-) \tag{2.29}$$

By inserting these potentials for Li^+ (Eq. 2.28) and OH^- (Eq. 2.29) in the initial equation 2.27, leads to

$$\mu_{Li}^{intercal.} + \mu_{H_2O}^0 = \mu_{Li^+}^0 + \frac{RT}{F}\ln(Li^+) + \mu_{OH^-}^0 + \frac{RT}{F}\ln(OH^-) + \frac{1}{2}\mu_{H_2}^0 \tag{2.30}$$

Because of charge neutrality ($(Li^+)=(OH^-)$), equation 2.30 can be simplified.

$$\mu_{Li}^{intercal.} + \mu_{H_2O}^0 = \mu_{Li^+}^0 + 2\frac{RT}{F}\ln(OH^-) + \mu_{OH^-}^0 + \frac{1}{2}\mu_{H_2}^0 \tag{2.31}$$

As the pH can be expressed in depends of OH^-

$$\begin{gathered} pH+pOH = 14 \\ pH = -\log(H^+) = 14 - (-\log(OH^-)) = 14 + \log(OH^-) \\ \log(OH^-) = pH - 14 \end{gathered} \tag{2.32}$$

Write the term in equation 2.31, which depends on OH^- as an expression of the pH as shown in equation 2.32, leads to equation 2.33.

$$\mu_{Li}^{intercal.} + \mu_{H_2O}^0 = \mu_{Li^+}^0 + 2\frac{\ln(10)RT}{F}\ (pH - 14) + \mu_{OH^-}^0 + \frac{1}{2}\mu_{H_2}^0 \tag{2.33}$$

At room temperature:

$$\frac{\ln(10)RT}{F} = 0.059\ \text{V} \tag{2.34}$$

Using the simplification of equation 2.34 for equation 2.33, leads to

$$\mu_{Li}^{intercal.} + \mu_{H_2O}^0 = \mu_{Li^+}^0 + 2 \cdot 0.059\ \text{V} \cdot (pH - 14) + \mu_{OH^-}^0 + \frac{1}{2}\mu_{H_2}^0 \tag{2.35}$$

Multiplying all values with each other

$$\mu_{Li}^{intercal.} = 0.118\ \text{V} \cdot pH - 1.652\ \text{V} + \mu_{Li^+}^0 + \mu_{OH^-}^0 + \frac{1}{2}\mu_{H_2}^0 - \mu_{H_2O}^0 \tag{2.36}$$

$$0.118\ \text{V} \cdot pH = \mu_{Li}^{intercal.} + 1.652\ \text{V} - \mu_{Li^+}^0 - \mu_{OH^-}^0 - \frac{1}{2}\mu_{H_2}^0 + \mu_{H_2O}^0 \tag{2.37}$$

As shown by Li et al.[54], the cell potential $E(x)$ of an Li/Li$^+$ intercalation reaction can be calculated as

$$E(x) = -\frac{1}{e}(\mu_{Li}^{intercal.} - \mu_{Li}^0) \tag{2.38}$$

Convert equation 2.38:

$$\mu_{Li}^{intercal.} = -eE(x) + \mu_{Li}^0 \tag{2.39}$$

Using the equation 2.37 for 2.39

$$0.118\ \text{V} \cdot pH = -eE(x) + 1.652\ \text{V} + \mu_{Li}^0 + \mu_{H_2O}^0 - \mu_{Li^+}^0 - \mu_{OH^-}^0 - \frac{1}{2}\mu_{H_2}^0 \tag{2.40}$$

The remaining terms of equation 2.40 as illustrated in equation 2.41, is basically the expression of is minus the change of the Gibbs free energy of the reaction in 2.42

$$\mu_{Li}^0 + \mu_{H_2O}^0 - \mu_{Li^+}^0 - \mu_{OH^-}^0 - \frac{1}{2}\mu_{H_2}^0 \tag{2.41}$$

$$Li + H_2O \rightleftharpoons LiOH + \frac{1}{2}H_2 \tag{2.42}$$

The change in the Gibbs free energy of reaction 2.42 is DG=-2.228 eV.[55] Apply this change in the Gibbs free energy to equation 2.40, leads to equation 2.43

$$0.118\ \text{V} \cdot pH = 1.652\ \text{V} - eE(x) + 2.228\ \text{V} \tag{2.43}$$

Solve for E(x)

$$E(x) = -0.118\ \text{V} \cdot pH + 3.88\ \text{V} \tag{2.44}$$

The cathode potential can be calculated as in equation 2.45.

$$E(x)_{LMO} = -0.118\ \text{V} \cdot pH + 3.88\ \text{V} - E^0_{LMO} \tag{2.45}$$

For the here used material, the first equilibrium potential (E^0_{LMO}) i.e. the first potential plateau for the delithiation reaction ($Li_xMn_2O_4$ for 0.5≤ x ≤1), in an electrolyte of EC/DMS, is at 3.996 V vs. Li/Li^+. In the following, this equilibrium potential is used, as the delithiation during the OER in aqueous solution is only for a short time and therefore not in the regime of the second equilibrium potential for a much pronounced delithiation (0≤ x ≤0.5). E^0_{LMO}=3.996 V

$$E(x)_{LMO} = -0.118\ \text{V} \cdot pH + 3.88\ \text{V} - 3.996\ \text{V} \tag{2.46}$$

Sum up equation 2.46, leads to equation 2.47.

$$E(x)_{LMO} = -0.11\ \text{V} - 0.118\ \text{V} \cdot pH \tag{2.47}$$

As equation 2.47 describes the intercalation reaction (lithiation) at the cathode, the cell polarization for the delithiation process at the anode has the opposite sign, as written in equation 2.48.

$$E(x)_{LMO} = 0.11\ \text{V} + 0.118\ \text{V} \cdot pH \tag{2.48}$$

This equation is used in chapter 5 to predict the stability of $LiMn_2O_4$ in different concentrated LiOH electrolytes.

2.5.3. Nernst slope

The *Nerst slope* describes the potential change of an electrode, when changing the concentration of the reactant (electrolyte) by a factor of ten. For the OER (Eq. 2.2) in alkaline solution, the system contains mainly of water and hydroxide molecules, where the concentration of hydroxides in water corresponds to the pH. Thereby, the Nernst slope of this aqueous solution is accessible by derive the electromotive force of the Nernst equation for the OER (Eq. 2.25) with respect to the pH, as written in equation 2.49.[17]

$$\frac{dE}{dpH} = -0.059 \text{ V} \tag{2.49}$$

2.5.4. Kinetics in electrochemistry

The kinetics of a redox reaction is influenced by the potential of the electrode. These kinetics are described in the *Butler-Volmer equation* 2.56 — it describes the dependence of the current and the potential of this electrode.[17, 72]

The theory based on charged particles within the double layer. When changing the Galvani potential of the electrode the potential distribution of the double layer (Fig. 2.7) changes as well. For a simple redox reaction like water splitting, the kinetics J_k depend on the Gibbs energy ΔG.[17]

$$J_k(\phi) = -c_{ox} \cdot k_0 \cdot exp\left[-\frac{\Delta G(\phi)}{RT}\right] \tag{2.50}$$

In this model the reaction is only limited by the charge transfer, however the concentration of electrons and reactive species are assumed as constant. A change in the electrode potential ϕ_1 by $\Delta\phi$ is causing a change in the kinetics by

$$(1-\alpha) \cdot z \cdot F \cdot \Delta\phi \tag{2.51}$$

As a result, the exchange current density j_0 changes too.

$$j_D^-(\phi) = -zF \cdot c_{ox} \cdot k_0^- \cdot exp\left[-\frac{\Delta G(\phi_1) + (1-\alpha)zF \cdot \Delta\phi}{RT}\right] \tag{2.52}$$

And in anodic direction

$$j_D^+(\phi) = zF \cdot c_{red} \cdot k_0^+ \cdot exp\left[-\frac{\Delta G(\phi_1) + \alpha zF \cdot \Delta\phi}{RT}\right] \tag{2.53}$$

In an equilibrium, the exchange current density could be described by $\phi = \phi_0$

$$j_0 = j_k(\phi_0) \tag{2.54}$$

This causes a simplification, as all pre-factors and the first part of the exponential term can be summed up of equation 2.52 and 2.53. A change in the potential is described by the activation overpotential

$$\Delta\phi = \phi_0 + \eta_D \tag{2.55}$$

That leads to a current density in dependence of the activation overpotential.

$$j_D = j_D^+ + j_D^- = j_0 \left\{ exp\left[\frac{\alpha z F}{RT}\eta_D\right] - exp\left[-\frac{(1-\alpha)zF}{RT}\eta_D\right]\right\} \tag{2.56}$$

In case of high overpotential the Butler-Volmer equation can be simplified to the Tafel equation (chapter 2.5.5).

2.5.5. Tafel equation and Tafel slope

In case of high overpotentials (for anodic reaction $\eta \gg \frac{25.7}{z}$ mV, for cathodic reaction $\eta \ll \frac{-25.7}{z}$ mV at room temperature) the *Butler-Vollmer equation* can be simplified because one of the exponential terms gets neglectable.[17] For the anodic reaction

$$j_D = j_0 \; exp\left[-\frac{\alpha z F}{RT}\eta_D\right] \tag{2.57}$$

The logarithm of equation 2.57 leads to the *Tafel equation*.

$$\eta_D = A + B \; \log|j_D| \tag{2.58}$$

In which B is the so called *Tafel slope*:

$$B = \frac{\ln(10)RT}{\alpha z F} \tag{2.59}$$

The charge transfer coefficient (α), for a single electron transfer is assumed as 0.5 and 0 in case of non-transfer. For a multi-electron transfer reaction like the OER, equation 2.59

is adjusted to equation 2.60, with $\frac{\ln(10)RT}{F} = 0.059$ V at room temperature (298 K).[73]

$$B = \frac{0.059 \text{ V}}{z_{before} + 0.5 z_{during}} \tag{2.60}$$

Therefore, the Tafel slope (B) relies on the ratio of the transferred electrons before (z_{before}) and during (z_{during}) the rate limiting step. The connection between the Tafel slope and the rate limiting step (RLS) for the four-electron transfer OER is illustrated in table 2.1.[74]

Table 2.1.: Tafel slope and classification of corresponding rate limiting step[75] as well transferred electrons before and during the RLS and the resulting reaction rate (chapter 2.5.6)

Tafel slope [mV/dec]	**Rate limiting step**	**Numbers of electrons**		**Reaction rate**
		z_{before}	z_{during}	
14.75	chemical	4	0	4
16.86	electrochemical	3	1	4
19.67	chemical	3	0	3
23.6	electrochemical	2	1	3
29.5	chemical	2	0	2
39.33	electrochemical	1	1	2
59	chemical	1	0	1
118	electrochemical	0	1	1

Therefore, it is possible to identify, if the rate step is electrochemically or chemically limited, as latter does not involve an electron transfer ($z_{during} = 0$).[73] Although, there are further combinations of z_{before} and z_{during} for the OER, than shown in table 2.1, however this would include an unrealistic multi-electron transfer during the RLS.

2.5.6. Reaction rate

The OER can be divided in several partial reactions, in which more than the reactant of the total reaction is involved. Besides, the stoichiometric factors of one species in this partial reaction can differ from its factor of the total reaction. The stoichiometric factors of these involved equilibrium reactions are known as the reaction rate x_j of z transferred

electrons.[17]

$$Reactant_{ox} \rightleftharpoons \sum_{j=1}^{z} x_j^{ox} \cdot Reactant_j \tag{2.61}$$

By using the law of mass action to replace c_{ox} in equation 2.52 by

$$c_{ox} = K_{ox} \prod c_j^{x_j^{ox}} \tag{2.62}$$

the resulting equation is shown in 2.63

$$j_D^-(\phi) = -zF \cdot K_{ox} \prod c_j^{x_j^{ox}} \cdot k_0^- \cdot exp\left[-\frac{\Delta G(\phi_1) + (1-\alpha)zF \cdot \Delta\phi}{RT}\right] \tag{2.63}$$

By logarithmizing and partially deriving to the concentration results in the dependence of the current density and the reaction rate.[17]

$$\frac{\partial \ln j_D}{\partial \ln c_k} = x_k^{ox} \tag{2.64}$$

The possible reaction rates for the OER with the corresponding Tafel slope are illustrated in table 2.1.

3. Experimental techniques

In this chapter, the experimental techniques are introduced to the reader. This chapter is divided into two parts. The first part focuses on the electrochemical methods to characterize the electrocatalytic performance by rotating ring disk-electrode (RRDE) and the electrochemical modification. While the second part deals with the methods to characterize the initial and modified material by various techniques.
To characterize the active material in its initial and modified state is a crucial step to get a deeper inside in the fundamentals of activity versus manganese valence and surface morphology. The aim to control the manganese valence by changing the stoichiometric lithium content is challenging as a quantitatively determination of the lithium content is ambitious due to its low atomic mass. Therefore, we used XRD to determine the lattice constant and thereby indirectly stoichiometric lithium content. Besides that, XAS was used to determine the manganese oxidation as a complementary method to electron energy loss spectroscopy (EELS).

3.1. Catalytic characterization by rotating ring disk-electrode

For the characterization of the electrocatalytic activity and stability of $Li_xMn_2O_4$, a RRDE setup was used. The main idea of this setup goes back to 1958 and is based on the principal of a forced convection of the electrolyte — i.e. mass transport of the ions or molecules in the electrolyte.[76–78]

Since the measured current signal during the experiment is influenced by the local concentration of the ions or molecules of the electrolyte near the electrode's surface, convection has an important impact on an electrochemical experiment. A quiescent electrolyte in which no active transport of the electrolyte's ions occurs, is only a suitable approach for short-term experiments on a timescale less than 30 seconds. On such a timescale the

influences of convection are negligible.[72]

A simple experiment to demonstrated the impact of convection on an electrochemical experiment can be seen by using a redox couple e.g. potassium ferricyanide (III) ($K_3[Fe(CN)_6]$) in the electrolyte. As shown in figure 3.1a the electrode near Fe^{3+} ions of the electrolyte get reduced to Fe^{2+}, when sweeping to lower potentials. This is indicated by the increase of the cathodic current. This occurs until all electrode near ions are reduced and no more Fe^{3+} is locally available, which than causes a decrease in the cathodic current. In this case, the reaction is limited by the diffusion of un-consumed Fe^{3+} to the electrode. Sweeping back to higher potentials leads to an oxidation of the produced Fe^{2+} back to Fe^{3+} until all Fe^{2+} is consumed.[79]

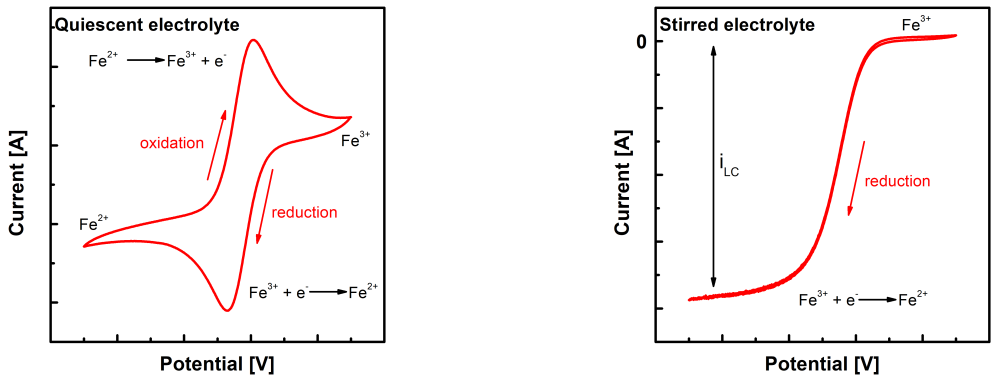

(a) (b)

Figure 3.1.: (a) Experiment in a quiescent $K_3[Fe(CN)_6]$ electrolyte: cathodic current increase until all electrode-near Fe^{3+} ions are reduced to Fe^{2+} and no further ions can be reduced — reaction is limited by diffusion (b) experiment in a stirred $K_3[Fe(CN)_6]$ electrolyte: reduction of Fe^{3+} to Fe^{2+} occurs in the reduction potential window as a continuous mass transport provides un-consumed Fe^{3+} to the electrode — reaction is limited by mass transport and reaches the cathodic limiting current i_{LC}.

For experiments on a longer timescale, diffusion limitation can be avoided by a forced convection, introduced to the electrolyte e.g. by stirring. As demonstrated in figure 3.1b, this forced convection causes a transport of un-consumed Fe^{3+} to the electrode, which can

continuously reduced and removed from the electrode. Consequently, this experiment is limited by the mass transport, which depends on the rotation speed.

In the case of the RRDE setup, this forced convection is introduced by the rotation of the electrode itself. This setup contains of two working electrodes. In the centre, there is a glassy carbon disk electrode on which the catalyst is applied (Fig. 3.2). Although, the current signal of the water splitting reactions are not influenced by the hydrodynamics, as illustrated in figure 3.1a, even for a quiescent electrolyte as the reaction is not limited by the mass transport of the reactant, one can benefit from the setup. As the rotation causes a laminar flow of the electrolyte and thereby a continuous mass transport, the reaction product, namely here oxygen, can be qualitatively detected at the second working electrode (Fig. 3.2).

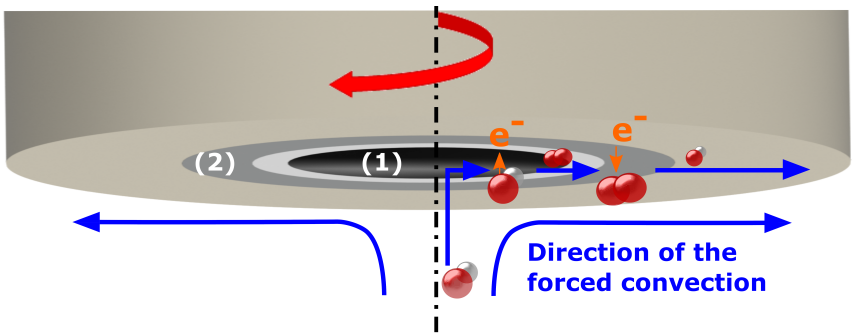

Figure 3.2.: Mass transport at a RRDE used in the investigation of the OER in alkaline solution: a hydroxyl ion from the bulk of the electrolyte arrives at the surface of the disk electrode (1) and gets oxidized to oxygen (loss of electrons as shown in Eq. 3.2, conveys by the flow to the ring electrode (2), where it is detected by the reduction back to a hydroxyl ion (gain of electrons as shown in Eq. 3.3).

However, only a fraction of the, at the disk electrode generated products arrive at the ring electrode, where it can be detected. This fraction is called *collection efficiency* ($N_{col.eff.}$) and is the ratio of the limiting current of the ring electrode ($i_{L,ring}$) and the limiting current of the disk electrode ($i_{L,disk}$) (Eq. 3.1) with n electrons transferred at these electrodes. For the here used system, a collection efficiency of approximately up to 40% for redox

couples is reported.[76, 78]

$$N_{col.eff.} = |\frac{i_{L,ring}}{i_{L,disk}} \cdot \frac{n_{disk}}{n_{ring}}| \tag{3.1}$$

To perform such an experiment to evaluate the electrocatalytic behaviour of a material, the potential at the disk electrode sweeps from an initial potential to a maximum potential and back by a constant scan rate — i.e. performing a cyclic voltammetry (CV) at the disk electrode (Fig. 3.3).

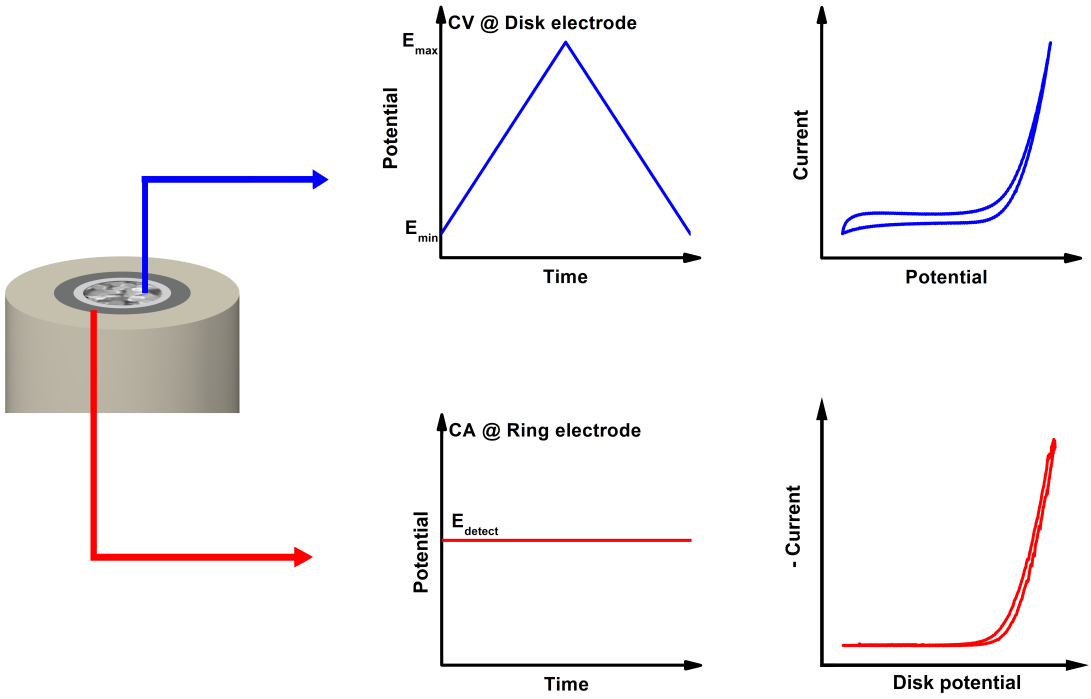

Figure 3.3.: Experimental setup for the RRDE: Active material is applied to the disk electrode, at which a CV is performed, i.e. the potential sweeps from the initial potential to a maximum and back over time. When the needed overpotential is reached to drive the water splitting reaction, an exponential current increase can be observed. Simultaneously, a CA at ring electrode (detection electrode) is performed i.e. the ring is set to a fixed potential and the current is measured — this current is plotted over the applied disk potential.

As the water oxidation reaction occurs at a certain overpotential (see also chapter 2.1),

which is indicated by an exponentially increase of the catalytic current at the disk electrode (Eq. 3.2):

$$4OH^- \longrightarrow O_2 + 2H_2O + 4e^- \tag{3.2}$$

Simultaneously, the ring electrode is set to a fixed detection potential, while the current is measured. As a result of the detection reaction, an increase in the ring current is observed. As the chemical reaction, which occurs at the ring electrode, is the backward reaction of the disk half reaction, this half reaction can be written as equation 3.3.

$$O_2 + 2H_2O + 4e^- \longrightarrow 4OH^- \tag{3.3}$$

However, additional information about the stability of the catalyst itself, during catalytic cycling can also be made by this setup, as it also enables to detect manganese leaching (MnO_4^-) as a side reaction (Eq. 3.4).

$$MnO_4^- + 2H_2O + 3e^- \longrightarrow MnO_2 + 4OH^- \tag{3.4}$$

This insoluble manganese(IV) oxide as a product of the detection deposits on the platinum ring electrode. In this project, we detect these two reaction products separately: oxygen and manganese. In table 3.1 the detection potentials can be found, to which the ring electrode was set.

Table 3.1.: Used detection potentials. Determining potentials see chapter 4.2.2

Species	**Detection potential [V vs. RHE]**
Oxygen	0.4
Manganese	1.2

In this project we are using a RRDE-setup from *ALS Japan Co, Ltd.* with ring electrode of 5 mm inner diameter and 7 mm outer diameter. The glassy carbon disk electrode is made by *HTW Hochtemperatur-Werkstoffe GmbH* with a diameter of 4 mm. A spacer made of polytetrafluoroehylene (PTFE) between these two working electrodes is sealing the electrode setup preventing the electrolyte to enter and also to electrically insulate the electrodes from each other. A loading of 50 μg of the active material was realized by drop casting.[1] The rotation speed is set to 1600 rpm.

[1]Ink casting and ink composition table A.1

3.2. Modification of $LiMn_2O_4$ by (de)lithiation in an ex-situ battery cell

To synthesize a sufficient amount of modified material, a custom made battery cell was used. The ex-situ cell is containing of a PEEK middle fitting, which can be tighten by a plunger made of stainless steel and a cap nut. As active material the initial $Li_1Mn_2O_4$ powder mixed with carbon black (same ratio as needed for electrocatalytic experiments) is filled in. A pad of cotton is used as a separator, which separates spatially both electrodes. A few millilitres of ethylene carbonate/ dimethyl carbonate (50:50) (EC/DMC) containing lithium hexafluorophosphate ($LiPF_6$) (from Sigma-Aldrich) are dropped on the separator until it is fully soaked.

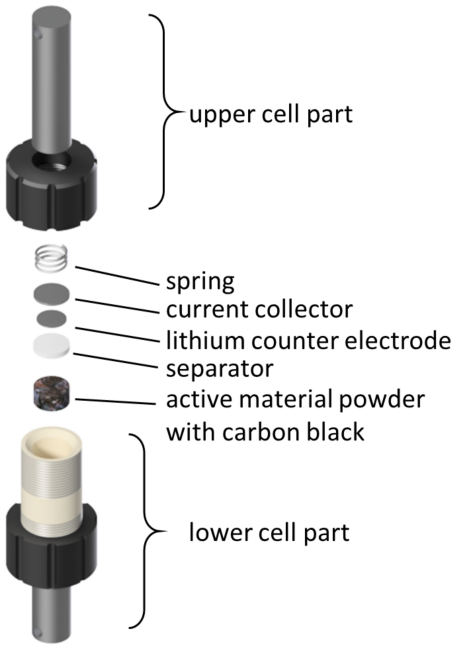

Figure 3.4.: CAD plot of used custom-made ex-situ cell for modification of pristine $LiMn_2O_4$ by (de)lithiation. By using this cell we synthesize approx. 100 mg of $Li_{1-x}Mn_2O_4$.

A piece of lithium, used as counter electrode, is laid on top of the separator. A stainless steel coin is added as a current collector. The whole assembly is sealed from the environment by tighten the upper plunger, which compresses the inner setup by a spring. Due to the used chemicals, the cell assembly has to be done in a glovebox under argon

atmosphere (<0.5 ppm O_2 and <0.5 ppm H_2O).

To modify the pristine $Li_1Mn_2O_4$, a constant current is applied to the cell (see (dis)charging curve Fig. 2.6). This current for a defined (de)lithiation can be calculated in consideration of the *1st Faraday's law*, that the amount of active material (n) is proportional to the total conducted charge (Q) during an electrochemical reaction.

$$Q = \frac{m \cdot F \cdot z}{M_{LiMn_2O_4}} \tag{3.5}$$

As the Faraday constant (F) can be expressed as 26.80 Ah, which is more common in the field of battery research and there is only one electron (z) transferred per $LiMn_2O_4$ molecule, equation 3.5 can be simplified.

$$Q_{theo.} = \frac{26.8 \text{ Ah}}{180.2 \text{ g/mol}} = 148.07 \text{ mAh/g} \tag{3.6}$$

To calculate the (de)lithiation current (I), $Q_{theo.}$ has to be transferred in a defined time (t) per mass of active material (m).

$$I = \frac{Q_{theo.} \cdot m}{t} \tag{3.7}$$

To express the needed time to transfer this theoretical total charge in a defined time by a constant current is known as C-rate, i.e. that in a e.g. C/5 the theoretical total charge is transferred in five hours. As Lim et al.[80] reported, the (de)lithiation process of a particle proceeds inhomogeneously. Consequently, there are different areas with different distribution of lithium in one particle during this reaction. Therefore, a moderate C-rate of C/12 was chosen, to generate a material with a most homogeneous distributed lithium content

In this work, for the modification of the initial material, the (de)lithation current was calculated by equation 3.7 — as each batch contained approximatly 100 mg of $Li_xMn_2O_4$ and a C/12 rate was chosen for the synthesis, the current to drive the (de)lithiation reaction is — depending on the individual loading of active material — a current of approximately 925 μA for a total delithation reaction was used. For small values of x, it is possible to set the cell to a hold potential at the exit potential (here: 4.5 V vs. Li/Li^+)to drive the reaction to an end.

3.3. Characterization methods to determine structural and electronic properties of $Li_xMn_2O_4$

As it is hard to identify lithium with the standard analytic techniques, we choose mostly indirect methods to determine the lithium content and the resulting manganese valence state. Due to the wavelength of X-rays, which is the order of atomic bonds and lattice structures, they are a suitable tool for these analysis. Therefore, different X-ray techniques, as XRD, XAS and X-ray photoelectron spectroscopy (XPS) were used to determine structural and electronic properties of the material for the correlation with the catalytic activity. Besides, scanning electron microscopy was used to determine the morphology i.e. particle shape and size distribution. In the following, the principles of these techniques are introduced to the reader.

3.3.1. X-ray diffraction (XRD)

By interacting with matter X-rays can provide different information of material and chemical properties. X-ray diffraction is a method to gain structural information of the material by elastic scattering — so called Thomson scattering.

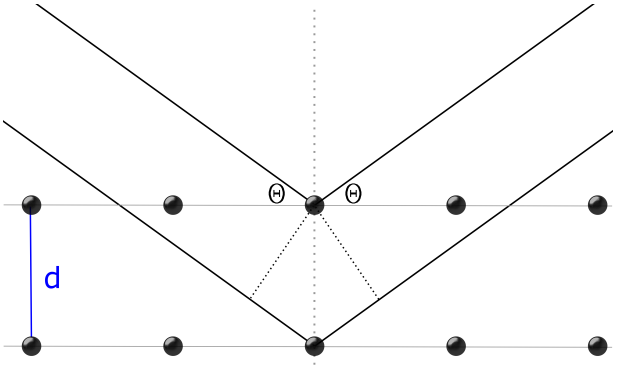

Figure 3.5.: Illustrating Bragg reflection in case of constructive interference of scattered X-rays

In case of constructive interference as shown in figure 3.5 the Bragg's law 3.8 is obeyed. Where d is the distance between equivalent atomic planes, the wavelength λ, the angle θ of the incident X-rays and a factor ($n \in \mathbb{N}$) for a phase shift.

$$2 \cdot d \cdot sin(\Theta) = n \cdot \lambda \tag{3.8}$$

As $Li_xMn_2O_4$ (for x≤1) has a cubic structure, the determination of the lattice constant (a) is given by equation 3.9, where h,k,l are the Miller indices of the reflections.

$$d_{hkl} = \frac{a}{\sqrt{h^2 + k^2 + l^2}} \tag{3.9}$$

Using an in-situ XRD battery cell provided by an external collaborator, we were able to establish a calibration curve, in which we can correlate the lattice constant and the lithium content.
This calibration experiment allows us, to use XRD as a fast and accurate method to control indirectly the lithium content of the modified catalyst by its lattice constant.[81] All XRD characterization experiments of the $Li_xMn_2O_4$ particles (initial as well as modified) were performed by a Bruker D8 Discovery with monochromatized CuK_α radiation in a two theta range of 15°-85° in 0.05° step size.

3.3.2. X-ray absorption spectroscopy (XAS)

When X-rays interact with matter, a part of it will be absorbed and the initial intensity (I_0) will be exponentially reduced referring to the *Lambert-Beer law* (Eq. 3.10).

$$I = I_0 \cdot e^{-\mu x} \tag{3.10}$$

This absorption depends on the sample thickness x and the element specific absorption coefficient μ. Latter roughly proportional (Eq. 3.11) to the density ρ, atomic number Z, atomic mass A and the X-ray energy E.[82]

$$\mu \approx \frac{\rho Z^4}{AE^3} \tag{3.11}$$

If the X-ray energy of the beamline (of the synchrotron) is tuned in the range, in which core electrons are exited, an electron is promoted by an absorbed X-ray out of the atom into the continuum (Fig. 3.6a). This process can be observed in a sharply rise in absorption (edge) in the X-ray absorption near-edge structure (XANES) spectra (Fig. 3.6b). As indicated by equation 3.11, the needed photon energy is element specific. Besides, it is influenced by the oxidation state as a gain or loss of electrons has an impact on the binding energy of the remaining electrons and thereby on the needed energy, i.e., a higher oxidation of a sample causes an edge shift to higher photon energies.[82]

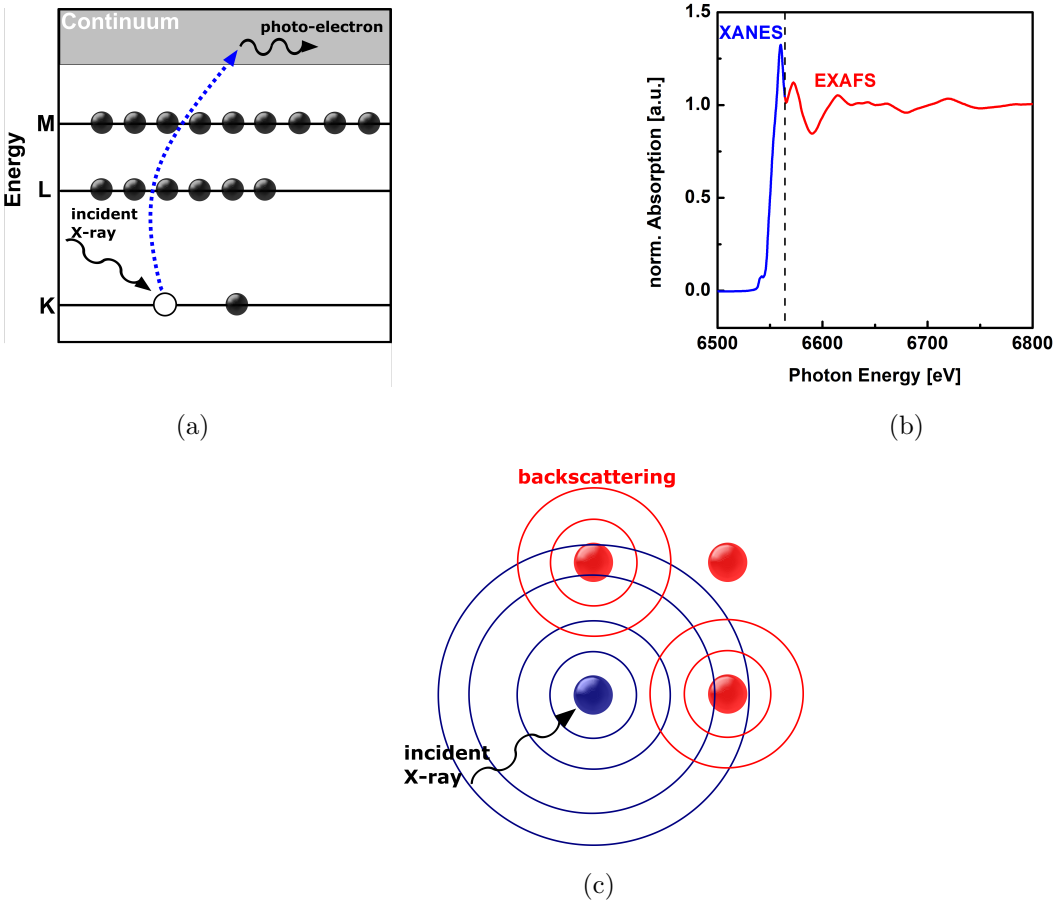

(a) (b)

(c)

Figure 3.6.: (a) Electron of K-shell is promoted by an absorbed X-ray out of the atom into the continuum and (b) the resulting X-ray absorption spectra: Blue XANES part due to promoting a core shell electron into continuum and red EXAFS part due to backscattering of neighbouring atoms (c) the reaction of neighbouring atoms (red) of this incident providing additional information about the extended fine structure

Therefore, it is a suitable method to estimate the oxidation state of a sample by determine the edge position of its XANES spectra. However, an additional calibration curve, which contains of different oxides with defined oxidation states is required.[83, 84] To determine the energy of the edge position of a sample — and therefore its oxidation state — three different methods are discussed in literature.[83]

- Photon energy of the edge at half-height absorption of a normalized spectra (0.5)
- Photon energy of the edge at the inflection point ($\frac{d^2\mu}{dE^2}$)
- Photon energy of the edge as the mean energy value of the edge step determine by an integral of the XANES region

In this thesis the integral method is used, as the edge energy can be determined with a high accuracy and it is less sensitive to shape variations of the edge which are not associated with an edge shift.[83]
Besides, the position of the edge and thereby the oxidation state, the XANES spectra also provides information of the coordination by the pre-edge. Additional information of the local structure of the sample — such as the number of neighbouring atoms, the distance to them, as well as the coordination of the atoms — are provided by the extended X-ray absorption fine structure (EXAFS) region of the XAS spectra in figure 3.6b (red part). These information are a result of backscattering events of neighbouring atoms next to the absorber atom (Fig. 3.6c).[82]

The here reported XAS experiments were performed at ALBA-synchrotron, Spain (Beamline BL22 CLÆSS) and at BESSY II synchrotron, Berlin (Beamline KMC-2 and KMC-3). In general a XAS scan was performed, starting 200 eV before the edge ($E_{0;Mn-K}$=6539 eV) up to 6800 eV. The energy step size before the edge is 5 eV and a smaller step size of 0.05 eV after E_0. For energy calibration a manganese foil was used.

3.3.3. X-ray photoelectron spectroscopy (XPS)

X-ray photoelectron spectroscopy (XPS) is a surface sensitive method to analyse the chemical composition of a few monolayers of a sample. This information is generated by the *photoemission process* caused by an ejected electron from the top 1-10 nnm of a sample due to a X-ray photon absorption (Fig3.7).[85]

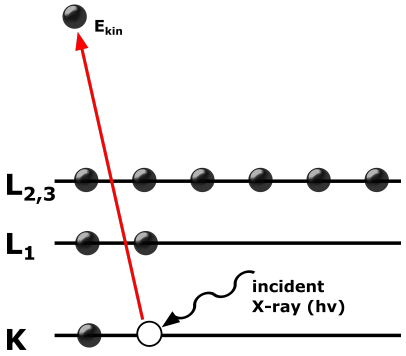

Figure 3.7.: Photoemission process: electron is ejected out of the atom by an absorbed X-ray photon

The kinetic energy (E_{kin}) of the ejected electron depends on the incident X-ray energy ($h\nu$) and the binding energy (E_{bind}) as illustrated in equation 3.12. The kinetic energy of the emitted electron is measured.[85, 86]

$$E_{kin} = h\nu - E_{bind} \tag{3.12}$$

As the needed X-ray photon energy is element specific (Eq. 3.11), an analysis of the chemical composition of the sample is possible. Additionally, the binding energy, which influenced the measured kinetic energy, depends on e.g. the oxidation state and the orbital, from which the electron was ejected.[86]
Therefore, XPS is an appropriate method for the characterization of catalyst as the information is generated at the part of the sample, which is in direct contact with the electrolyte and the atoms which are involved in the reaction.

A rough XPS analysis of pristine particles was performed at an external institute, using a *PHI 5000 VersaProbe II* with an aluminum source and an energy resolution of 2.96-187.85 eV. The energy calibration was performed on a carbon tape.

3.3.4. Scanning electron microscopy (SEM)

The scanning electron microscope (SEM) is a microscopy technique using a focused electron beam which interacts with the atoms of a sample. Electrons are emitted e.g. by a field emission gun and focused by a lens system. By scanning a defined area of the sample with this electron beam, elastic and inelastic scattered electrons are detected for each scanned spot of the sample. These information are joint up to generate an image of the scanned sample area. An advantage of the SEM is the high depth of field of rather thick samples which provides information of surface properties and textures.[85]

In this research SEM is mainly used for determining particle sizes distribution in a statistical amount to get an inside in the catalytic active surface area (see also chapter 4). These investigations were performed in a *FEI Nova Nano SEM 650* in high vaccum mode at 5.00 kV, detecting secondary electrons.

4. Total disk current as sum of current contribution: the origin of the disk current

This chapter is a reproduction of the following publication:

Influence of particle size on the apparent electrocatalytic activity of $LiMn_2O_4$ for oxygen evolution

Max Baumung, Florian Schönewald, Torben Erichsen, Cynthia A. Volkert and Marcel Risch
Sustainable Energy Fuels, 2019, 3, 2218-2226; DOI 10.1039/C8SE00551F

Please note, that labels, reference numbers and the format have been adjusted to suit the format of this thesis.

Abstract: We investigate $LiMn_2O_4$ as a model catalyst for the oxygen evolution reaction (OER), because it shares the cubane structure with the active site of photosystem II. Specifically, we study the influence of different particle sizes of $LiMn_2O_4$ on the OER in a sodium hydroxide electrolyte. The product currents of manganese corrosion and oxygen evolution were obtained by rotating ring disk electrodes (RRDE). Physical characterization by various methods supports identical surface chemistry and microstructure of the pristine powders. We obtained similar oxygen current densities of 42(13) $\mu A/cm^2_{ECSA}$ and 26(5) $\mu A/cm^2_{ECSA}$ for micro- and nano-sized particles. However, the total current densities differed drastically and while the micro-powder had a high disk current density of 205(2) $\mu A/cm^2_{ECSA}$, its Faradic efficiency was only 20%. In contrast, the Faradic efficiency of the nanopowder was at least 75%. We hypothesize that a Mn redox process may occur in the bulk in parallel and possibly in combination with oxygen evolution on

the surface based on the observed difference between the total and product current densities. Knowledge of the product currents is crucial for distinguishing the mechanisms of corrosion and catalysis and for designing better catalysts with high Faradic efficiency.

4.1. Introduction

An adequate and reliable supply of energy is a necessity in our modern society. Currently, the most common energy vector is burning fossil fuels to generate heat and electricity.[3, 87, 88] However, due to climate change, political crises in the middle east and rising oil prices, the transition to renewable energy from solar and wind is highly desirable.[20] Unfortunately, these sources are not available on demand. Therefore, it is crucial to store the energy from renewables, when it is produced until it is needed. An attractive avenue is the splitting of water for storage of the produced hydrogen. This hydrogen could then be used in a fuel cell to generate electricity. The water splitting reaction is kinetically limited by the oxygen evolution reaction (OER).[88–90] We focus on $LiMn_2O_4$ as a model system in our research as it shares the cubane structure with the active site of photosystem II. Previously, we demonstrated that nano-sized $LiMn_2O_4$ is catalytically active in sodium hydroxide electrolytes and interpreted the key mechanistic parameters in the context of natural photosynthesis.[48] Here, we investigate the influence of the particle size of $LiMn_2O_4$ on catalytic activity. A rotation-ring disk electrode (RRDE) setup was used to measure the conventional disk currents and to monitor the trends of either Mn dissolution or oxygen evolution at a ring electrode during 10 cycles. We used X-ray diffraction and electron microscopy to quantify the particle structure and size distribution. While the disk current densities per surface area differed, the detected product currents due to Mn loss and oxygen evolution were identical within error. We hypothesize that the disk current densities differ due to contributions from the bulk, which is discussed in the context of the mechanisms of charge storage and catalysis.

4.2. Results and discussion

4.2.1. Characterization of pristine $LiMn_2O_4$ particles

XPS-analysis showed no significant difference in the surface electronic structure of the pristine nano- and micro-sized powders (Fig. A.1) so we focused on structural and morphological characterization. XRD measurements identified both oxide powders as $LiMn_2O_4$

(Fig. 4.1), despite slight differences in the peak widths and peak positions. The observed peak shifts indicate differences in lattice constants which may be due to impurities and defects introduced by the different production methods of the $LiMn_2O_4$-powders. Using the Scherrer equation (Eq. 4.1), we obtained a particle size of 47(4) nm for the nano-sized powder. (The Scherrer equation is only valid for particles smaller than 100 nm and was thus not applied to the XRD data of the micron-sized powder.[91]) We determined the experimental lattice parameter from the best fit of Bragg's law (Eq. 4.2) to the six reflections in Fig. 4.1. The nano-sized powder has a lattice constant of a_{nano}=8.21(1) Å and the micro-sized power a lattice constant of a_{micro}=8.28(1) Å, which were similar to the expected $a_{crystal}$=8.25 Å for $LiMn_2O_4$ (single crystals).[92] We note that the lattice constant of the previously measured nanopowder was found to be 8.15 Å using Rietveld refinement[48] and 8.12(1) Å using Bragg's law. Due to the difference between this work and our previous study,[48] the XRD measurements were repeated two additional times, giving a_{nano}=8.22(1) Å and a_{nano}=8.24(1) Å, which are both close to the expected value and deviate by less than 0.4 . The previously measured lower lattice parameter could be due to the specimen not being exactly in the X-ray focus or due to slight lithium[93] or oxygen[94] deficiency in the investigated powders, which emphasizes the importance of careful storage and measurement of the powders.

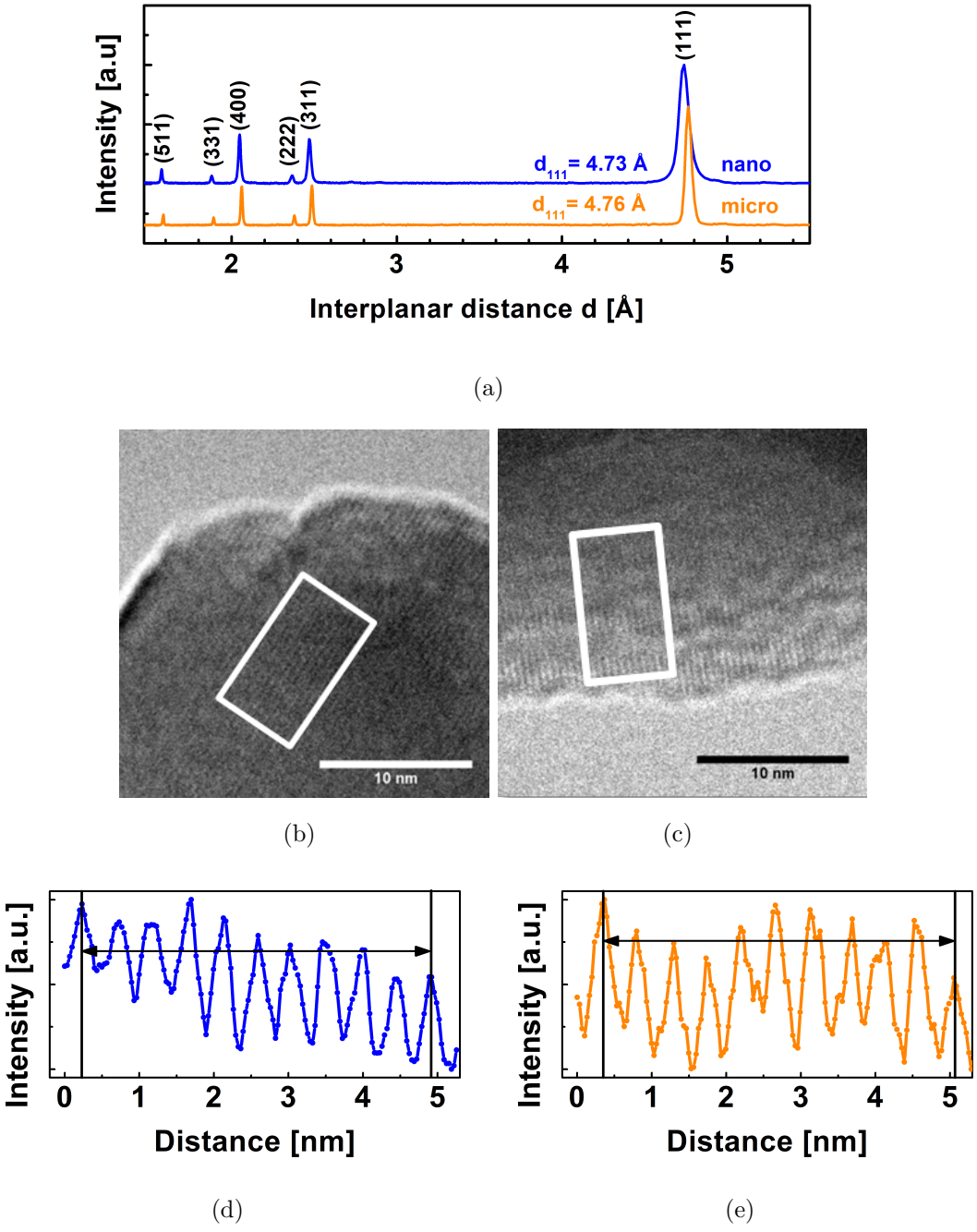

Figure 4.1.: (a) XRD diffractogram of nano- and micro-sized $LiMn_2O_4$. The background-corrected intensities were normalized to the (111) peak and offset for clarity. HRTEM picture of (b) nano-sized and (c) micro-sized powder as well as interplanar distance for the (111) orientation of (d) nano-sized powder with d_{111}=4.68 Å and (e) micro-sized powder with d_{111}=4.72 Å. The intensity profiles were obtained in the white boxes and arrows indicate the lattice fringes used in the analysis.

Knowing the lattice parameter and space group allows the density of the particles to be calculated as ρ_{nano}=4.339(3) g/cm^3 and ρ_{micro}=4.230(1) g/cm^3. The density of $LiMn_2O_4$ was previously reported to have a somewhat higher value of 4.436(1) g/cm^3 due to the smaller value of the measured lattice constant.[48] The lattice spacing of the (111) reflection was also obtained using TEM. The micrographs clearly show lattice fringes up to the surface of nano-sized (Fig. 4.1b) and micro-sized (Fig. 4.1c) $LiMn_2O_4$ particles. The analysis of ten oscillations in the intensity profiles revealed d_{111}=4.68 Å for the nanopowder and d_{111}=4.72 Å for the micropowder (Fig. 4.1d,e). These are smaller than the corresponding (111) diffraction reflections obtained by XRD for the nano-sized (d_{111}=4.73 Å) and micro-sized powders (d_{111}=4.76 Å). The TEM values have higher uncertainty ($\leq$1%) than the XRD measurements due to a less exact calibration. It also has to be noted, that only a few HRTEM measurements were performed (additional images in Fig. A.2-A.3, so that no statistics could be carried out over a large ensemble of particles, in contrast to XRD. Still, the TEM measured values are comparable to each other and larger trends and changes could have been resolved but were not observed. In summary, the TEM and XRD analyses agree within the accuracy of the methods and support an identical crystal structure of both powders. We characterized the particle shape and size distributions by SEM (Fig. 4.2a,b). The micro- and nano-sized particles were mainly truncated octahedrons and some truncated rhombic dodecahedrons (Fig. A.4). Therefore, both pristine powders consist predominantly of 111 facets, with some 100 and 110 facets, in agreement with the calculated equilibrium particle shapes.[95] The nano-sized particles tended to agglomerate (Fig. 4.2a) in contrast to the micro-sized particles which did not agglomerate (Fig. 4.2b). Additional SEM images may be found in the electronic supporting information (Fig. A.5). A TEM investigation of nanopowder sizes showed a comparable particle distribution with the same frequent diameter (Fig. A.6).

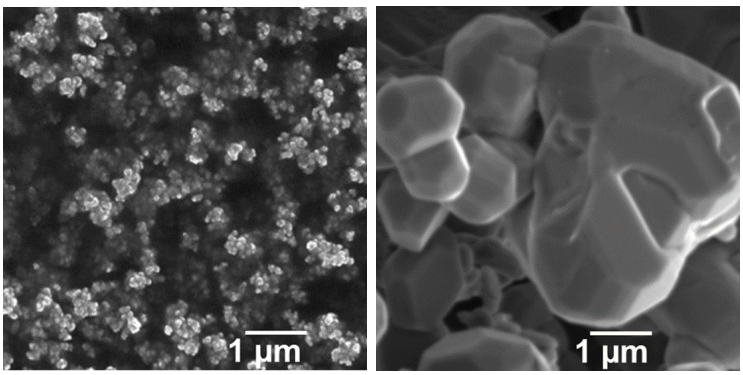

(a) (b)

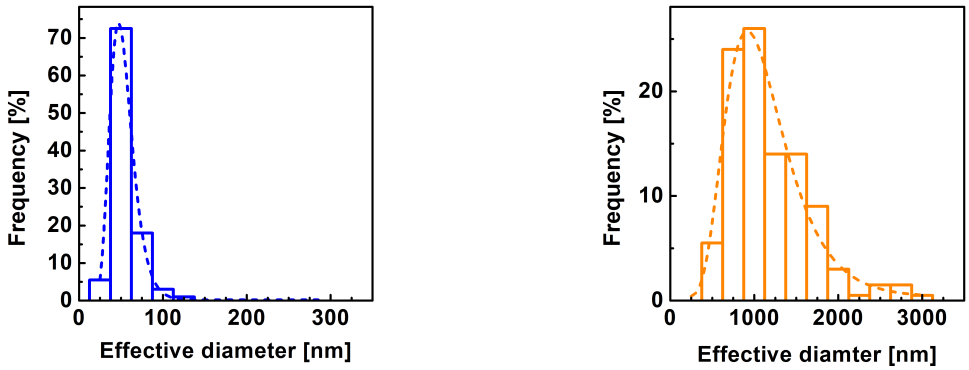

(c) (d)

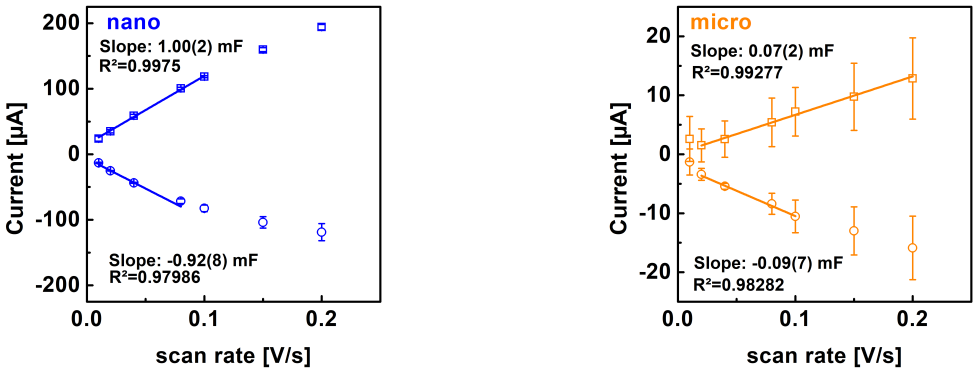

(e) (f)

Figure 4.2.: SEM-characterization of (a) nano-sized and (b) micro-sized $LiMn_2O_4$ and corresponding histograms of (c) nano-sized and (d) micro-sized $LiMn_2O_4$. Dotted lines show the fit to a lognormal distribution. Anodic (squares) and cathodic (circles) currents from cyclic voltammetry of (e) nano-sized and (f) micro-sized $LiMn_2O_4$ ink-casted disks for evaluation of the double layer capacitance. Error bars were obtained using at least three independent measurements and may be too small to be visible.

The mean and most common nano-particle diameters were calculated from a lognormal fit to the experimental distribution as 44(14) nm and 42 nm, respectively, which are similar to the crystallite size of 47(4) nm determined by the Scherrer equation. For the micro-sized particles, the mean and most common diameters were calculated as 1.2(6) μm and 1.0 μm, respectively. We approximated the truncated octahedra as spheres for the estimation of the specific surface area (Eq. 4.3), to obtain 14.376(7) m^2/g for nano-sized $LiMn_2O_4$. In the work of Köhler et al. the specific surface was calculated as 12.264(2) m^2/g,[48] mainly due to the smaller lattice parameter (and thus larger density). For the micro-sized powder, we calculated a specific surface of 0.490(4) m^2/g. The latter agrees well with the specific surface of perovskite oxides with similar diameter.[10] As an alternative measure of the oxide surface area, we also performed cyclic voltammetry to probe the double-layer capacitance (Fig. A.7). The (differential) capacitance (C_d) of the electrode was obtained by linear regression of the currents at 1.174 V vs. RHE against the sweep speed (Fig. 4.2e,f). The fit range was chosen to minimize the Pearson correlation coefficient (Table A.2). The capacitance of the micropowder was less reproducible as compared to the nanopowder for reasons that are not entirely clear but possibly the target loading was less accurate for the micropowders, which sedimented quickly during ink-casting. The anodic currents (squares) showed better linearity and were thus selected for evaluation. We obtained capacitances of 1.00(2) mF and 0.07(2) mF for the nano- and micro-sized powders. These capacitances are proportional to the ECSA but the exact conversion factor (specific capacitance) is not known for $LiMn_2O_4$. Nonetheless, using the specific capacitance of α-Mn_2O_3 of 0.19(8) mF/cm^2_{ox},[96] gave quite reasonable agreement with the SEM based estimates of the electrode surface areas (Table 4.1). However, the ratio of the ECSAs of the nanopowder to the micropowder is a factor of two smaller than the ratio of SEM determined areas (Table 4.1). The discrepancy likely arises due to agglomeration, of the nanoparticles, making much of their surface area inaccessible for the electrochemical measurement. Nonetheless, both methods demonstrate that the surface area of the nanopowder was clearly larger than that of the micropowder as expected.

Table 4.1.: Physical properties of nano- and micron-sized $LiMn_2O_4$ and their ratios.[96]

Property	**Micro (M)**	**Nano (N)**	**Ratio N/M**
Disk current (μA)[1]	75(7)	186(4)	2.5
Ring current (μA)[1]	0.178(2)	7.55(4)	42.4
Specific surface area (m^2/g)[2]	0.49(4)	14.38(1)	29.4
SEM surface (cm^2_{SEM}))[2]	0.25(1)	7.19(3)	29.4
Capacity (mF)[3]	0.07(2)	1.00(2)	14.3
ECSA (cm^2_{ECSA})[3]	0.37(2)	5.26(3)	14.3

4.2.2. Electrochemical calibration experiments

For the RRDE investigations of stability and activity, the detection potential for manganese and oxygen at the ring has to be selected. The general goal is to find a potential where the reduction of only one species occurs. In order to identify these potentials, we added either oxygen gas or permanganate ions to the sodium hydroxide electrolyte. The platinum ring-electrode was scanned from 0 V vs. RHE to 1.55 V vs. RHE to detect the reduction of these species (Fig. 4.3). We identified detection potentials of 0.4 V vs. RHE for oxygen and 1.2 V vs. RHE for manganese. We also performed the RRDE experiment at both detection potentials without any rotation (Fig. A.8), which suggested that there was no significant electronic crosstalk between the ring current and the disk current that would affect the product detection.[97]

[1] at 1.68 V vs. RHE applied to disk during 5^{th} cycle. Disk area 0.126 cm^2; catalyst loading 0.4 mg/cm^2

[2] determined by SEM; Fig. 4.2 c,d

[3] the electrochemical surface area (ECSA) was determined by cyclic voltammetry; Fig. 4.2e,f. Specific capacitance was assumed to be 0.19(8) mF/cm^2_{ox}.[96] The disk area was 0.126 cm^2

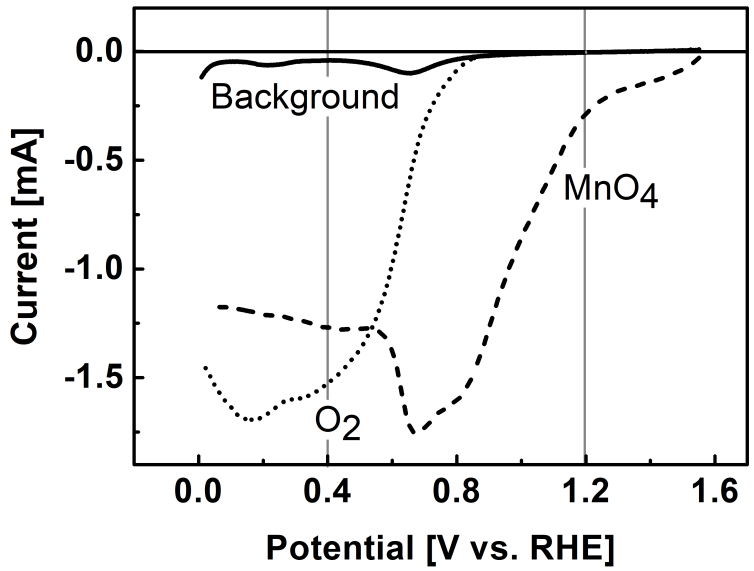

Figure 4.3.: Identification of the ring potential for oxygen (dotted; in oxygen-saturated electrolyte) and permanganate (dashed; in argon-saturated electrolyte) by CV. The detection potential was set to 0.4 V vs. RHE for oxygen and 1.2 V vs. RHE for manganese detection as indicated by vertical lines.

The detection potential for manganese could not be set to a potential, for which the detection is limited by Mn transport (i.e. current independent of potential) while avoiding overlap with the detection of oxygen. Thus, only qualitative detection is possible for Mn and we did not correct the measured ring currents for the collection efficiency. The identified detection potential of 1.2 V vs. RHE is identical to that previously used in the literature.[98, 99] The detection potential for oxygen was set on the current plateau at 0.4 V vs. RHE, where oxygen detection is limited by diffusion of oxygen. This detection potential is also identical to that previously used in the literature.[98, 99] It is challenging to quantify the amount of the released oxygen, due to bubble formation at the disk electrode and the PTFE (polytetrafluoroethylene) spacer, which prevent a continuous transport to the ring electrode.[42, 48] Therefore, the oxygen detection is also only qualitative and we did not correct the measured ring currents for the collection efficiency. Since detection of manganese is also possible at 0.4 V vs. RHE, it is imperative to exclude the presence of manganese in the electrolyte. This motivated us to study the activation process of $LiMn_2O_4$ described in the next section.

4.2.3. Catalyst activation and performance

The stability of the two types of $LiMn_2O_4$ particles was investigated at the detection potential for Mn during cyclic voltammetry (Fig. 4.4). The ring currents increased above 1.4 V vs. RHE, indicating dissolution of Mn in the electrolyte during the first cycle for both the nano- and micro-sized $LiMn_2O_4$ based electrodes. The ring currents for both powders decreased with increasing cycle number and little change was observed between the fifth and tenth cycles. The currents for the nano-$LiMn_2O_4$ are similar to our previous study[48] and are much larger than for the micro-sized $LiMn_2O_4$, presumably due to the much larger surface area. We performed post-mortem TEM on electrodes cycled ten times between 1.25 and 1.75 V vs. RHE (Fig. 4.4c,d), to investigate the stability of both types of particles. Lattice fringes up to the surface could still be resolved after electrochemical cycling. This can be seen most clearly in an additional picture recorded with a higher resolution TEM (Fig. A.9) similar to ref.[48]. Neither particle showed evidence of surface amorphization as reported, e.g., for perovskites.[99–101] The inter–planar distances obtained after catalysis (Fig. 4.4e,f), are d_{111}=4.74 Å for the nanopowder and d_{111}=4.68 Å for the micropowder, which are very close to the values of the pristine samples (d_{111}=4.68 Å and 4.72 Å, respectively). The lattice fringes were somewhat more difficult to resolve for the thicker microparticles, but are nonetheless clearly detectable, meaning that the crystal structure of $LiMn_2O_4$ was preserved for both nano- and micro-sized particles despite loss of Mn from the materials during the initial cycles.

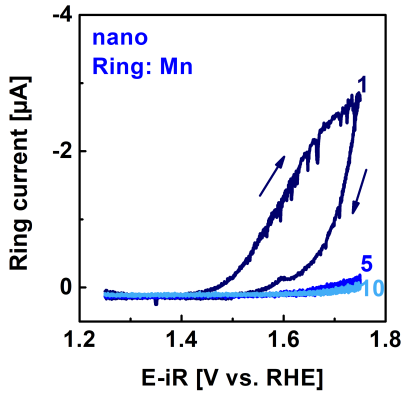

(a)

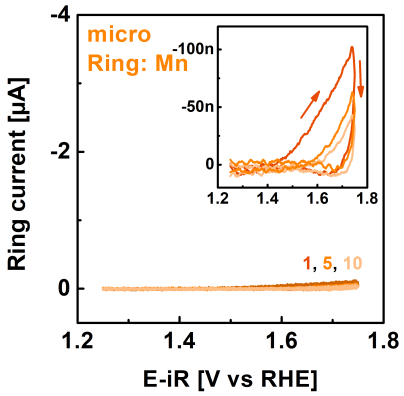

(b)

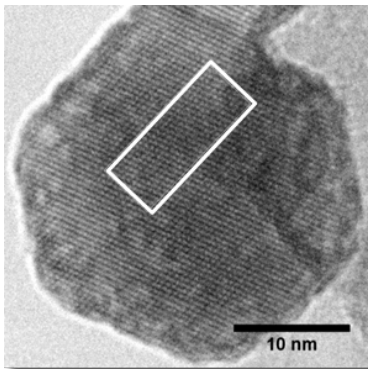

(c)

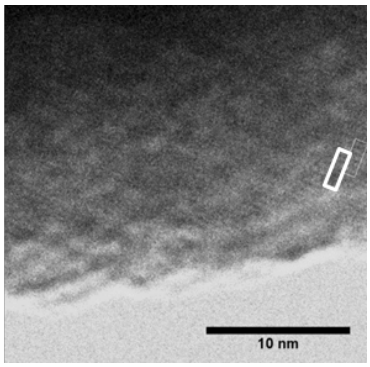

(d)

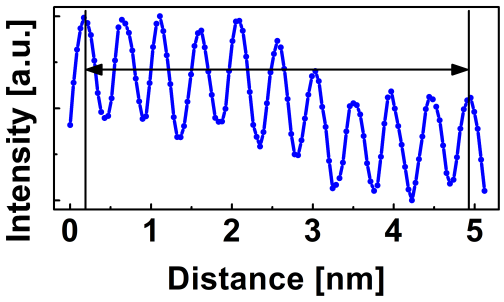

(e)

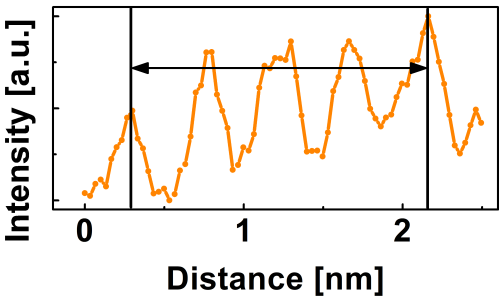

(f)

Figure 4.4.: Detection of Mn loss at 1.2 V vs. RHE for (a) nano-sized and (b) micro-sized powder (inset smoothed by Savitzky-Golay method). Post-mortem TEM investigation of (c) nano-sized and (d) micro-sized $LiMn_2O_4$ and interplanar distance for the (111) orientation of (e) nano-sized powder with d_{111}=4.74 Å and (f) micro-sized powder with d_{111}=4.68 Å. The intensity profiles were obtained in the white boxes and arrows indicate the lattice fringes used in the analysis.

Having confirmed the absence of structural changes due to catalysis, we now discuss the CV traces and corresponding catalytic currents during the fifth cycle, during which the loss of Mn had reached steady state. The CV traces at the disk only show an exponential rise above 1.6 V vs. RHE (Fig. 4.5a). The shape of the CV trace of the micropowder was slightly asymmetric, which may indicate the hidden shoulder of a redox peak. The disk current of the nano-sized powder was higher than that of the micron-sized powder (Fig. 4.5a) as expected due to the larger surface area (Table 4.1). Due to the ambiguity of the total disk current, qualitative detection of oxygen generated at the disk was performed by setting the ring potential to 0.4 V vs. RHE as discussed above (Fig. 4.5b). The positive-going traces of the ring current follow the same trends as the disk currents, while the negative-going scans show strong hysteresis likely due to trapping of oxygen at the spacer. This effect is particularly pronounced for the micropowder.

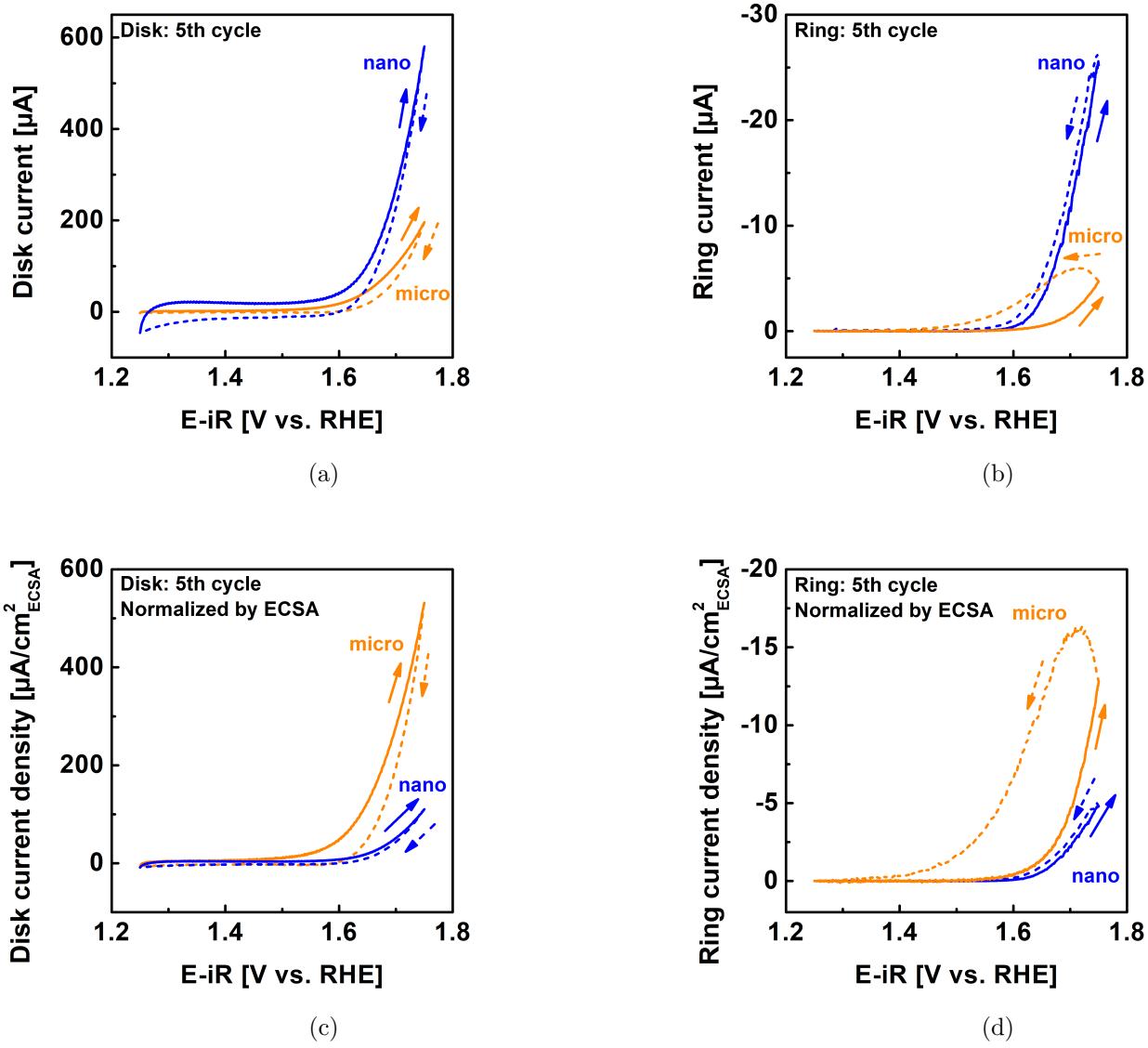

Figure 4.5.: (a) Representative cyclic voltammograms (fifth cycle) of nano- and micro-sized $LiMn_2O_4$ ink-casted disks and (b) and ring current of the corresponding oxygen detection at the ring electrode at 0.4 V vs. RHE (c) Cyclic voltammetry (fifth cycle) of nano- and micro-sized $LiMn_2O_4$ ink-casted disks normalized by the ECSA and (d) and the corresponding oxygen detection at the ring electrode at 0.4 V vs. RHE also normalized by ECSA. The positive-going half cycles are shown as solid lines, while the negative-going half-cycles are shown as dashed lines.

To investigate whether there are intrinsic differences between the two powders, we focused on the currents normalized by the ECSA as a proxy for the active surface area of the oxide. The area from SEM was not considered for the detailed analysis due to particle agglomeration. Surprisingly, the disk (Fig. 4.5c) and ring (Fig. 4.5d) current densities of the micropowder exceeded that of the nanopowder, although the ring current densities of the positive-going cycles were similar (Fig. 4.5d). Due to the observed hysteresis in the negative-going half-cycle (dashed lines), we only evaluated the positive-going half-cycle (solid lines) in detail. The disk, O_2 and Mn ring current densities were recorded at a disk potential of 1.68 V vs. RHE for both particle sizes as a function of cycle number (Fig. 4.6). The disk current densities of the micro-sized particles are higher than those of the nano-sized particles for all cycles (Fig. 4.6a). The current densities of both particle sizes decreased with cycle number to a nearly constant value. In contrast, the ring current densities due to oxygen evolution were nearly constant and their averages were the same within error (solid symbols in Fig. 4.6b). The measured currents are not necessarily directly proportional to the available surface area, e.g., when the electrode loading is varied.[102] Yet, the constant and similar ring current densities of the two powders suggests that the activity is proportional to the available surface area. The ring currents due to Mn loss (Fig. 4.6c) show a similar trend with cycle number to the disk current densities and are the same for both particle sizes within the noise. During later cycles, the experimental error of some points included zero current density, yet the averages (solid symbols) did not vanish. A continuous small loss of Mn was also reported for sputtered manganese oxide by a different method.[103] Identical ring currents due to catalysis (O_2) and corrosion (Mn) are expected and have been confirmed because the pristine powders were chemically identical as demonstrated by XPS (Fig. A.1) and have the same crystal facets (Fig. A.4). Moreover, the similarity of the ring current densities due to Mn loss indicates that the surfaces of the micro- and nano-sized $LiMn_2O_4$ particles change in the same way with cycle number and thus retain an identical activity per (electrochemical) surface area within experimental error. However, both ring measurements were qualitative and additional analysis is required to quantify the activity for oxygen evolution.

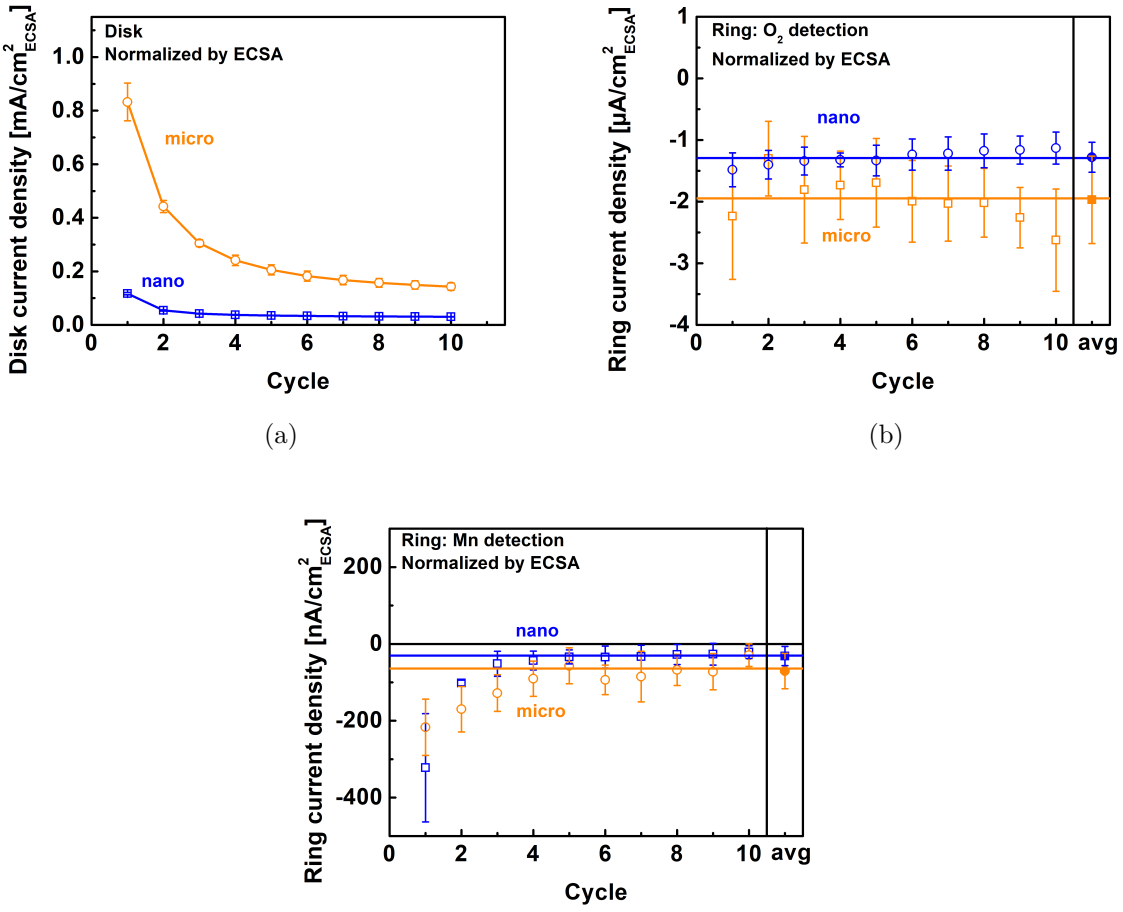

Figure 4.6.: Trends of (a) disk current density, (b) the corresponding current density of the ring set to detect oxygen and (c) the corresponding current density of the ring set to detect manganese. The data points were evaluated at a disk potential of 1.68 V vs. RHE during all ten cycles. Only the positive-going half-cycle was considered and normalized by the ECSA. Error bars indicate the standard deviation of three (nano) and eight (micro) independent measurements. Connecting lines were added to guide the eye.

4.2.4. Origin of disk currents

The disk currents of conventional electrochemical experiments are ambiguous as they do not discriminate between redox currents, catalytic currents and corrosion currents. Using product detection at ring electrodes, we aim to deconvolute the contributions to the disk

current. While the ring currents in our setup only qualitatively probed the currents due to catalysis (i.e. O_2 detection) and corrosion (i.e. Mn detection), the trends with the number of cycles permit a linear combination analysis of the disk current density according to $j_{disk}=c_{O2} \cdot j_{R,O2} + c_{Mn} \cdot j_{R,Mn} + c_x \cdot j_x$, where c_{O2}, c_{Mn}, c_x are the coefficients of oxygen evolution, Mn loss and additional processes (i.e. side reactions) with current density j_x, respectively, and j_{O2}, j_{Mn} the measured uncalibrated current densities at 1.68 V vs. RHE (Fig. 4.6). The best fit values for the coefficients may be found in Table A.4, where we have assumed that the coefficients are not changed by the particle size or by the cycle number. This is equivalent to assuming that the intrinsic nature of the reactions is not affected by particle size or cycle number and is justified by the chemical and structural characterization of both powders as supported by the previous discussions (Fig. A.1, Fig. A.4). The calibrated ring current densities are named after the detected product henceforth, i.e. oxygen and manganese current density.

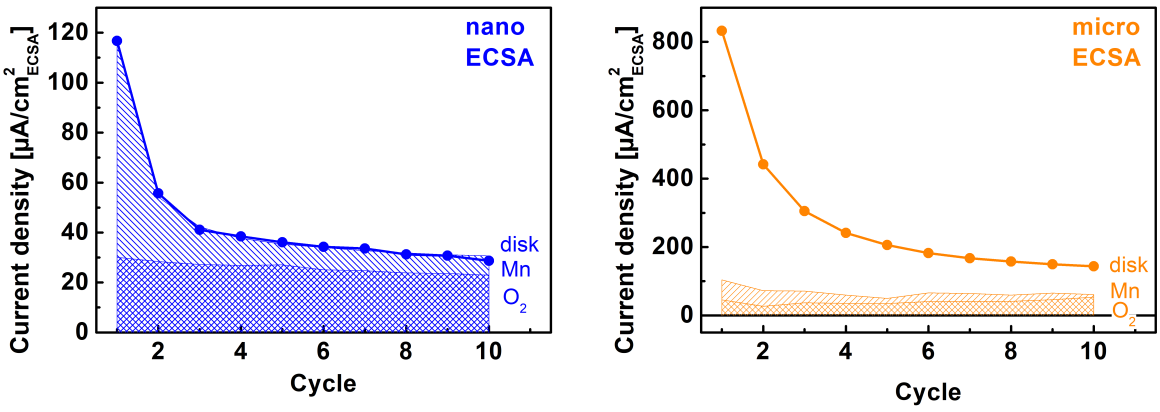

(a) (b)

Figure 4.7.: Calculated assignment of the currents due to Mn corrosion (line shade) and catalysis (cross shade) to the measured disk current (black line and circles) for (a) nano-sized and (b) micro-sized $LiMn_2O_4$. Calculation details may be found in the text. Connecting lines were added to guide the eye.

The disk current of the nanopowder was well described by only the first two terms in Eq. (4.1), namely $c_{O2}j_{R,O2} + c_{Mn}j_{R,Mn}$ (Fig. 4.7a). The oxygen current density was 26(5) $\mu A/cm^2_{ECSA}$ at 1.68 V vs. RHE independently of the cycle number. In contrast, the analysis of the manganese current density suggested that the decay of the disk current density as entirely due to Mn loss, which reached a nearly steady value of 8(7) $\mu A/cm^2_{ECSA}$

at the third cycle. As discussed above, the possibility that the Mn loss contribution has reduced to zero cannot be ruled out within the experimental error. The Faradaic efficiency for oxygen evolution can be calculated as $c_{O2}j_{R,O2}/j_{disk}$. It increased with cycle number from 26% to 75% with 75(2)% after the third cycle, which are lower boundaries as the manganese current density could have vanished. Any change in Faradaic efficiency after the third cycle was minor and the electrode can be considered activated thereafter. The analysis of the micropowder could be fit with the same values of the oxygen evolution and Mn loss coefficients as obtained from the nanopowder, but revealed an additional j_x contribution to the measured current density (Fig. 4.7b). It is worth pointing out that a similar quality fit to the two sets of data in Fig. 4.7 can be obtained by allowing some contribution from additional j_x processes during reaction of the nanopowder. However, the magnitude of the micropowder disk current makes it clear that these additional processes are much stronger for the micropowder than the nanopowder. Consequently, the Faradic efficiency is only 25(8) % and our model suggests that the majority of the measured disk current density of the micropowder comes from a different process. Product currents are unfortunately rarely reported in the literature. The ECSA-normalized current densities of micro-sized manganese oxides were benchmarked by Jung et al.[104] who reported disk currents at 0.35 V overpotential ranging for various ink-casted manganese oxides (Table A.5). Unfortunately, the Faradic efficiencies were not reported. Our micro-sized $LiMn_2O_4$ showed a disk current density of 34(3) $\mu A/cm^2_{ECSA}$, which is similar to the value of 31(25) reported for MnO.[104] However, our detailed analysis of the product currents showed that only a small fraction of this current contributes to oxygen evolution. The disk current generally depends on catalytic currents, corrosion currents and redox currents. Having measured and assigned the first two sources, we hypothesize that the remaining contribution is related to manganese redox throughout the particles, including in the bulk. Micro-sized particles have relatively more bulk atoms as compared to the smaller nano-sized particles. Unlike metals, oxides exhibit charged regions near the surface, the space charge layer. Furthermore, $LiMn_2O_4$ has also been previously discussed as a material for electrochemical supercapacitors in aqueous solutions[105] as well as for non-aqueous[56] and aqueous batteries.[106] These applications entail redox of manganese ions in the bulk, in most cases associated with Li addition or removal. Mn oxidation of the subsurface has also previously been reported during the activation procedure of another manganese oxide.[96] The shape of the CV trace of the micropowder in Fig. 4.5c further supports that a Mn redox process may occur. However, a definite proof requires additional measurements that are beyond the scope of this report. Mechanistic consid-

erations and our comparative study suggest that the particle size must be considered in the design of catalysts even in the case of identical surface chemistry and microstructure, since the bulk may contribute to the measured total currents. The mechanisms of manganese oxidation for charge storage in electrochemical capacitors[105] and batteries[56] are virtually identical to that of the common proposals for electrocatalysts before catalytic turnover.[21, 23, 101] In particular, we previously concluded that the electrocatalytic mechanism of our nanopowder includes an electrochemical pre-equilibrium step involving manganese oxidation coupled to a proton-transfer.[48] This step can also occur in electrochemical energy storage mechanisms that rely on the bulk such as batteries and capacitors, where the charge can also be compensated by species other than protons, e.g., Li. In contrast, catalysis requires the adsorption of the reactant, which can only occur on the surface. While the conditions of the electrochemical pre-equilibrium step may thus be satisfied in the bulk and on the surface, only the pre-equilibrium at the surface is relevant for product formation, i.e. oxygen evolution. Therefore, these spatial considerations can explain the observed commonalities and differences between nano- and micro-sized $LiMn_2O_4$, namely identical oxygen current density due to an identical surface chemistry and differing total current due to different bulk volumes.

4.3. Experimental

4.3.1. Materials

Micro-sized (electrochemical grade) and nano-sized (>99%) $LiMn_2O_4$ were purchased from Sigma-Aldrich. Tetrahydrofuran (THF) was purchased from VWR (≥99.9% stabilized). The electrolyte was 1 M sodium hydroxide Titripur (Merck) solution which was diluted to c_{NaOH}=0.1 M by ultrapure water (Milli-Q R ≥ 18.2 MΩ). The gases used to purge the electrolytes were purchased from AirLiquide Alphagaz (argon 5.0 and oxygen 4.8). Acetylene carbon black was purchased from Alfa Aesar (≥99.9%) and was acid-treated.[107] All other chemicals were used as received.

4.4. Physical characterization of $LiMn_2O_4$ particles

$LiMn_2O_4$ particles were characterized by X-ray diffraction (XRD) using a Bruker D8 Discovery with a monochromatized CuK_α radiation in the 2Θ range from 15° to 85°in 0.05° steps. Specimens for XRD measurements were prepared by gluing the oxide powder

to a glass slide. The particle size of the nanopowder was calculated using the Scherrer-equation

$$L = \frac{K \cdot \lambda}{\beta \cdot cos(\Theta)} \tag{4.1}$$

where is the line broadening at half maximum intensity and the shape factor K=0.8. We determined the experimental lattice parameter according to

$$a = d \cdot \sqrt{(h^2 + k^2 + l^2)} \tag{4.2}$$

where d is the lattice spacing in Bragg's law (λ_{Cu} = 1.5406 Å) and hkl are the Miller indices. The lattice constant of the powders was obtained by linear regression of d of six reflections on the inverse of the square root in Eq. (4.2). Scanning electron microscopy (SEM) was performed in a FEI Nova Nano SEM 650 in a high vacuum mode at 5 kV (micro-sized particles) and 15 kV (nano-sized particles). Specimens for SEM were prepared by mixing 10 mg oxide with 2 mL of THF and applied on a SEM carbon tape. For the evaluation of the average particle size, 200 randomly picked particles were measured. The elliptic shape of the particles was simplified as a circle and the equivalent diameter was calculated from the measured area as (Fig 4.2). Subsequently, we used the Cauchy expression to determine the specific area [108]

$$A_s = \frac{6}{\rho} \cdot \frac{\Sigma d_e^2}{\Sigma d_e^3} \tag{4.3}$$

where ρ is the density of $LiMn_2O_4$ calculated from the unit cell (i.e. assuming dense singly crystalline particles). The oxide particles were investigated in high-resolution transmission electron microscopy (TEM) before and after the experiments. For this investigation, we used a FEI Tecnai G^2 Spirit at 120 kV. For this, we drop-casted a copper-carbon TEM grid with the catalytic ink. For post mortem analysis, the same procedure was used after washing the particles off the electrode.

4.4.1. Electrochemical setup

For all catalysis experiments, an OrigaFlex system was used, composed of three OGF500 potentiostats (Origalys SAS) and for the determination of the double-layer capacitance, we used a Gamry Interface 1000E. Our measurement station consisted of a RRDE-3A rotator (ALS Japan Co Ltd.) and custom-made electrochemical cells made of polytetrafluoroethylene (PTFE) cylinders that were used in a three-electrode configuration with a saturated

calomel electrode (SCE) (ALS Japan Co Ltd., RE-2B) and a platinum counter electrode. The radial distance between the working and counter electrode or reference electrode was 17 mm. The RRDE-electrode setup consisted of a glassy carbon disk that is 4 mm in diameter (area=0.126 cm^2) and a concentric platinum ring with 5 mm inner diameter and 7 mm outer diameter. These working electrodes (disk and Pt-ring) were separately polished to a mirror finish with Al_2O_3-micro-polish and cleaned with isopropanol. The used SCE reference electrode was calibrated to the RHE scale (HydroFlex Gaskatel) by determining the offset of characteristic peaks during cyclic voltammetry (CV) on a clean polycrystalline Pt surface in the hydrogen underdeposition region.

4.4.2. Electrochemical calibration experiments

The electrolyte was first saturated with oxygen and a CV at the ring electrode was executed between 0-1.75 V vs. RHE at 100 mV/s for five cycles at 1600 RPM. The same procedure was carried out for an electrolyte saturated with argon. Afterwards, 10.3 mg of $KMnO_4$ was added to this argon-saturated electrolyte for a final molarity of 1 mM and another CV was carried out. $LiMn_2O_4$ catalytic ink was made by mixing 10 mg $LiMn_2O_4$ powder, 2 mg carbon black into a slurry of 2 mL THF. After sonication for 30 minutes, 10 μL of this suspension was applied on a polished glassy carbon disk, which was assembled in a RRDE setup. The ink covered the disk completely and homogeneously. The electrolyte was also saturated with argon 30 minutes before any of the electrochemical measurements.

4.4.3. Catalytic experiments

Six electrodes of the nanopowder were made so that three measurements each could be recorded with the ring set to oxygen and manganese. Due to the higher experimental errors, fifteen electrodes of the micropowder were prepared, of which three were recorded with the ring set to manganese and twelve with the ring set to oxygen. Of the latter, four measurements were discarded as the values differed by more than 50% from the median of all measurements. All catalytic experiments were performed using the same protocol. The disk electrode was conditioned at 1.25 V vs. RHE for three minutes and afterwards a CV between 1.25 V and 1.75 V vs. RHE was carried out at 10 mV/s for ten cycles at 1600 RPM. The ring electrode was set to the identified detection potential for manganese (1.2 V vs. RHE) or oxygen (0.4 V vs. RHE). All characterization and electrochemical experiments were carried out at room temperature. Subsequently, we

performed electrochemical impedance spectroscopy in the range from 100 kHz to 1 Hz to determine the uncompensated resistance and correct the applied voltage for the Ohmic drop. Typical uncompensated resistances were 50.72(1) Ω for electrodes coated with nano-sized and 47.64(4) Ω for micro-sized $LiMn_2O_4$.

4.4.4. Electrochemial determination of double-layer capacity

For the determination of the double layer capacitance all experiments were performed without rotation and a disconnected ring electrode. Data acquisition was performed in the 'surface mode' to capture the capacitive currents. The lower scan potential of 1.1 V vs. RHE was held for 60 seconds to equilibrate the powders, followed by cyclic voltammetry between 1.1 and 1.25 V vs. RHE with various scan rates (10, 20, 40, 80, 100, 150, 200 mV/s) was executed (Fig. A.7).

4.5. Conclusion

We observed an influence of the particle size on the electrocatalytic activity. Two commercial powders $LiMn_2O_4$ with mean particle sizes of 44(14) nm (nano) and 1.1(5) μm (micro) were selected for this study. They had nominally identical chemical composition and valence as probed by XPS. We determined similar lattice parameters of a_{nano}=8.21(1) Å and a_{micro}=8.28(1) Å that were also directly visible as lattice fringes in TEM. Based on the differential capacitance, we obtained ECSA of 5.26(3) cm^2_{ECSA} for the nanopowder and 0.37(2) cm^2_{ECSA} for the micropowder, which was used to calculate the current density per particle surface. The ring potentials for Mn (1.2 V vs. RHE) and O_2 (0.4 V vs. RHE) detection were identified firstly for the qualitative detection of the product currents and secondly for quantitative evaluation based on linear combination analysis. The total disk current densities decayed, which matched the trend of the current density due to manganese loss. The main reduction occurred in the first three cycles and we considered the catalyst fully activated after five cycles due to minor changes thereafter. The current density due to oxygen evolution was constant independently of cycling and the oxygen current densities (per ECSA) were identical for both powders as expected for identical surface chemistry and microstructure. The oxygen current densities were identical within error, namely 40(14) $\mu A/cm^2_{ECSA}$ and 26(5) $\mu A/cm^2_{ECSA}$ for micro- and nano-sized $LiMn_2O_4$, but only the latter had a Faradaic efficiency of at least 75%. We hypothesized that Mn redox in the bulk of micro-sized $LiMn_2O_4$ was the source of the large disk current

density (per ECSA), while the oxygen current densities of the micro- and nano-powders were identical due to identical surfaces. Bulk redox processes drive electrochemical energy storage in capacitor and battery materials, which provides a mechanistic link between these different subfields of electrochemistry. Furthermore, corrosion processes are often, if not always, in competition with catalysis. Therefore, the detailed knowledge of product currents is crucial, on the one hand for the rational design of better electrocatalysts as it is the relevant metric that should be optimized by materials design and on the other hand for a mechanistic understanding when more than one product is formed.

Acknowledgements

The authors are grateful for the financial support by the collaborative research center (CRC) 1073 (SFB 1073, project C05) sponsored by the Deutsche Forschungsgemeinschaft (DFG). We also like to thank Mr. R. Köhler and Prof. Dr W. Viöl (HAWK) for the XPS measurement. The XPS instrument was funded by the DFG.

5. Bulk oxidation of $LiMn_2O_4$ increases overpotential

This chapter is a reproduction of the following publication:

Undesired bulk oxidation of $LiMn_2O_4$ increases overpotential of electrocatalytic water oxidation in lithium hydroxide electrolyte

Max Baumung, Leon Kollenbach, Lifei Xi and Marcel Risch
ChemPhysChem 2019, 20, 2981. ; DOI 10.1002/cphc.201900601

Please note, that labels, reference numbers and the format have been adjusted to suit the format of this thesis.

Abstract: Chemical and structural changes preceding electrocatalysis obfuscate the nature of the active state of electrocatalysts for the oxygen evolution reaction (OER), which calls for model systems to gain systematic insight. We investigated the effect of bulk oxidation on the overpotential of ink-casted $LiMn_2O_4$ electrodes by a rotating ring-disk electrode (RRDE) setup and X-ray absorption spectroscopy (XAS) at the K shell core level of manganese ions (i.e. the Mn-K edge). The cyclic voltammogram of the RRDE disk shows pronounced redox peaks in lithium hydroxide electrolytes with pH between 12 and 13.5, which we assigned to bulk manganese redox based on XAS. The onset of the OER is pH-dependent on the reversible hydrogen electrode (RHE) scale with a Nernst slope of -40(4) mV/pH at -5 μA monitored at the RRDE ring. To connect this trend to catalyst changes, we develop a simple model for delithiation of $LiMn_2O_4$ in LiOH electrolytes, which gives the same Nernst slope of delithiation as our experimental data, i.e., 116(25) mV/pH. From this data, we construct an E^{RHE}-pH diagram that illustrates robustness of $LiMn_2O_4$ against oxidation above pH 13.5 as also verified by XAS. We conclude that manganese oxidation is the origin of the increase of the OER overpotential at

pH lower than 14 and also of the pH dependence on the RHE scale. Our work highlights that vulnerability to transition metal redox may lead to increased overpotentials, which is important for the design of stable electrocatalysts.

5.1. Introduction

Efficient storage of energy is one of the challenges in turning away from fossil energy vectors towards renewable energies and decelerate global warming.[3, 87] A promising pathway is water splitting for the production of hydrogen as a sustainable energy carrier. Unfortunately, this reaction is kinetically limited by the oxygen evolution reaction (OER),[11, 23] which mandates the use of an efficient catalyst. However, chemical and structural changes before or during electrocatalysis obfuscate the nature of the active state of electrocatalysts for the OER, which calls for model systems to gain systematic insight.

Previously, we studied $LiMn_2O_4$ as a model catalyst for the OER because it shares the structural motif with the active site of natural photosynthesis. We discussed the electrocatalytic mechanism of $LiMn_2O_4$ for the OER in the context of photosynthesis[48] and determined the product current due to the OER in NaOH,[15] which hinted at a significant involvement of the bulk to the measured currents as is the case, e.g., in batteries.

Here, the battery aspects of the material are discussed further from the viewpoint of electrocatalysis. $LiMn_2O_4$ was first reported as a positive electrode material for non-aqueous batteries by Thackeray et al.[51] and has since been optimized systematically.[56] Most relevant for electrocatalysis of $LiMn_2O_4$ is its previous use as an active material for aqueous batteries,[109] mainly in neutral[106, 109–114] electrolytes but also in alkaline electrolytes.[54, 55, 94] LiOH has not been used in aqueous Li-ion batteries, probably because the reversible potential of $LiMn_2O_4$ delithiation under standard conditions is above the thermodynamic potential in alkaline electrolytes, which can be illustrated by aligning the potential scale relative to the Li/Li^+ redox ("battery scale") to the scale of the standard hydrogen electrode (SHE).[109, 115] While OER before delithiation prevents operation as an aqueous battery, it is highly desirable for stable operation as a catalyst for oxygen evolution. Moreover, LiOH electrolytes are interesting for in-depth fundamental studies as the chemical complexity is reduced to the Li-Mn-O-H system, in contrast to all previous electrocatalytic investigations of $LiMn_2O_4$ in KOH[24] and NaOH[15, 45, 48]

electrolytes.

In this report, we investigate the oxygen evolution reaction on $LiMn_2O_4$ in LiOH electrolytes with pH between 12 and 14 using rotating ring disk electrodes (RRDE) and X-ray absorption spectroscopy (XAS). Disks of $LiMn_2O_4$ show pronounced redox peaks below pH 14 in LiOH, which was not previously reported in other hydroxide electrolytes.[15, 24, 45, 48] The redox peaks are assigned to Mn redox due to (de/-)lithiation of $LiMn_2O_4$. A simple model for the reversible potential of delithiation is derived, which matches the data well. Furthermore, the onset of oxygen evolution is determined using the ring of the RRDE. Finally, we construct an E^{RHE}-pH diagram based on the model and our experimental data. Predictions regarding the oxidation stability are verified using additional ex situ XAS measurements.

5.2. Results and Discussion

We used the same batch of commercially available $LiMn_2O_4$ nanopowder for our investigations in LiOH as was also used in our previous studies [11, 48] in NaOH where the pristine powder was extensively characterized by scanning electron microscopy (SEM) and transmission electron microscopy (TEM), X-ray diffraction (XRD) and soft XAS. In short, it has the expected crystal structure of semiconducting $LiMn_2O_4$ (space group Fd3m)[48] with lattice parameter a=8.21(1) Å[11] that is typical for the composition of $Li_1Mn_2O_4$.[93] The size distribution, space group and lattice parameter were confirmed again before the electrocatalytic experiments presented herein and showed similar values as those reported previously, namely a mean diameter 41(15) nm and a median of 40.45 nm (Fig. 5.1). An average manganese valence of +3.5(3) in the bulk was previously determined by soft XAS at the Mn-L edge using calibration to selected experimental references.[48] The oxide could thus be written $Li(Mn^{3+}Mn^{4+})O_4$ but we will not make this distinction because XAS can only measure averages. Overall, these analyses demonstrate that the pristine powder has the expected size, bulk crystal structure, bulk composition and bulk valence.

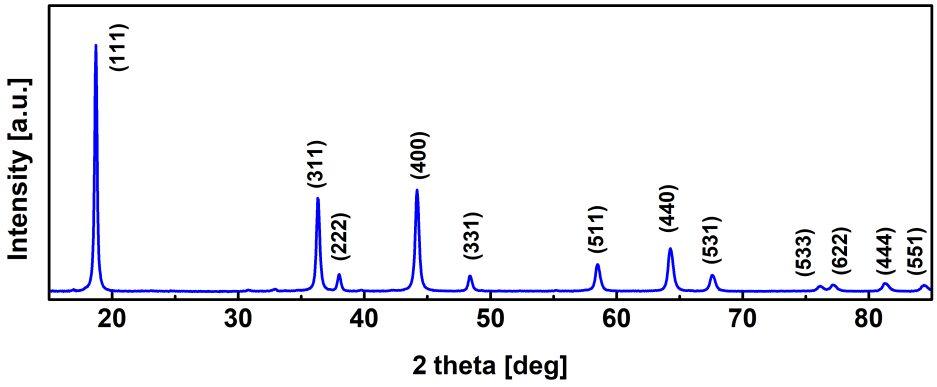

(a)

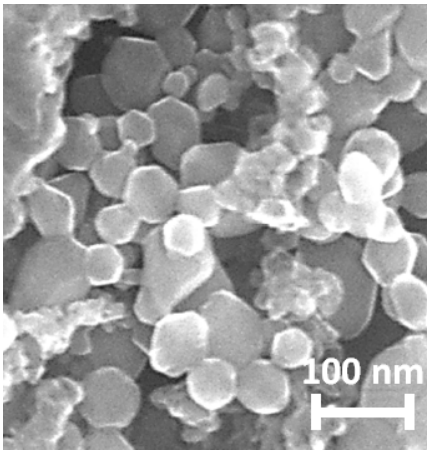

(b)

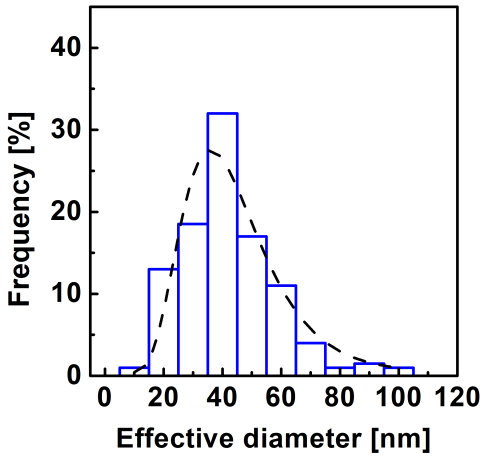

(c)

Figure 5.1.: (a) Indexed X-ray diffractogram of pristine $LiMn_2O_4$ particles (b) SEM image of the nanoparticles and (c) particle distribution (bars) and fitted lognormal distribution (dashed line)

The traces of the voltammogram in LiOH evidently differed from our previous studies in NaOH.[11, 48] We performed cyclic voltammetry and simultaneous chronoamperometry at the ring of the used RRDE setup in Ar-saturated hydroxide electrolytes. Exemplary disk current densities in 100 mM NaOH (gray line) and 100 mM LiOH (red line) are compared in Fig. 5.2a,b during the 5^{th} cycle, which was selected because initial Mn loss had ceased before the 5^{th} cycle in NaOH.[48] In LiOH, the currents due to Mn loss were higher as

compared to NaOH but also changed little after the 5^{th} cycle (Fig. A.10). Our previous studies showed no evidence of morphological changes of the $LiMn_2O_4$ nanoparticles in NaOH).[15, 48] As the detected Mn loss during the first 5 cycles is similar for all LiOH electrolytes (Fig. A.10) and also similar to the Mn loss reported in NaOH,[48] we expect that no changes in morphology occurred in the used LiOH electrolytes. In Fig. 5.2a, the anodic and cathodic traces of the CV in NaOH were featureless except for the exponential rise due to oxygen evolution,[11, 48] while there was a clear anodic shoulder and cathodic peak in the CV in LiOH. The rise in current density due to oxygen evolution occurs at lower voltages in 100 mM NaOH as compared to 100 mM LiOH (Fig. 5.2b), i.e. at a different pH, which is rationalizeddiscussed below as a chemical change of $LiMn_2O_4$ preceding OER in 100 mM LiOH below.

We investigated the CV of 10 mM LiOH further as it showed a clear exponential rise in current density and emphasized the aforementioned differences to previous studies in NaOH[15, 48] and KOH[24, 45] (Fig. 5.2c). The rising disk current density at high voltage was assigned based on the ring current (blue dashed line), which was set to reduce oxygen at 0.4 V vs. RHE and thus qualitatively detected the oxygen produced at the disk. We only show the anodic trace of the ring currents as the cathodic trace showed hysteresis due to trapped oxygen. As the anodic shoulder and cathodic peak do not show up in the ring current (as expected), it was likely related to manganese redox. Therefore, an additional redox reaction occurred at voltages below the onset of the OER on $LiMn_2O_4$ in 10 mM LiOH as compared to our previous studies in 100 mM NaOH.[15, 48]

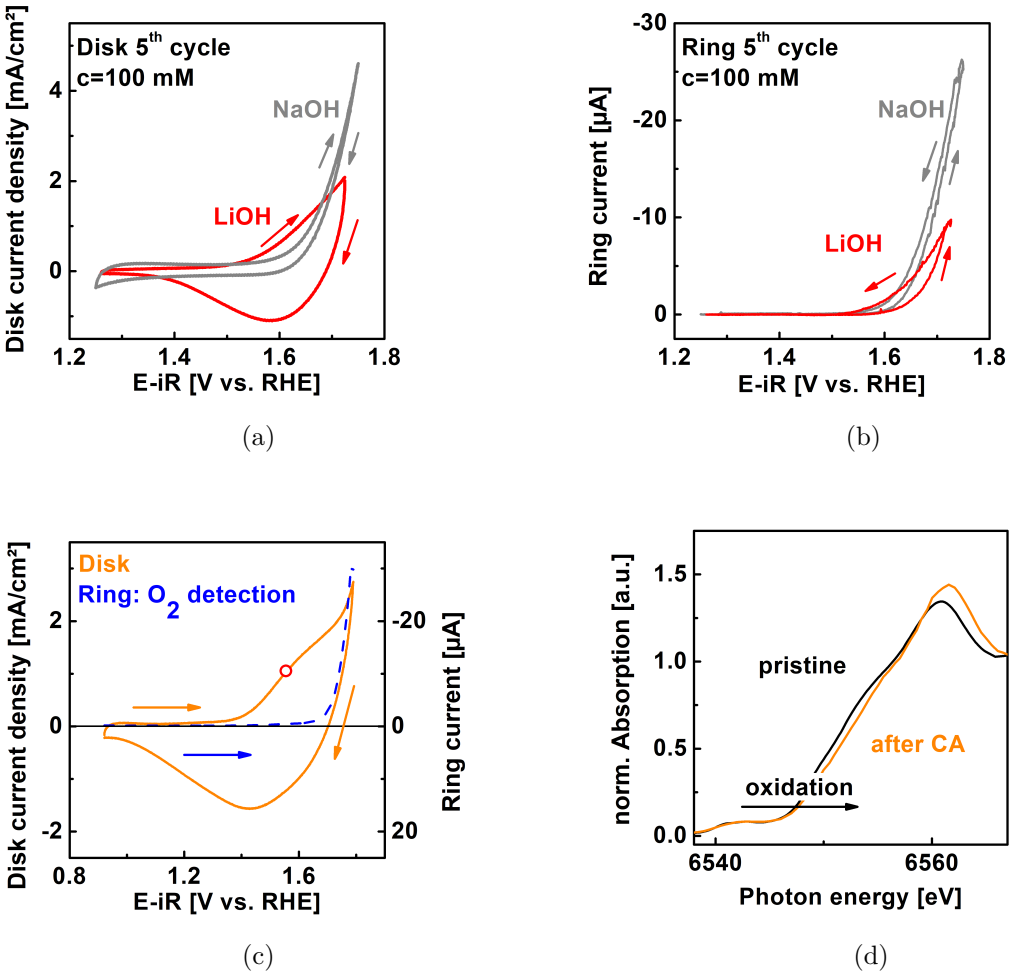

Figure 5.2.: (a) CV of $LiMn_2O_4$ in 100 mM NaOH and LiOH (pH 13) and b) corresponding oxygen detection at ring electrode (detection potential 0.4 V vs. RHE) The NaOH data was taken from ref. [15]. (c) CV of 5^{th} cycle in 10 mM LiOH (solid orange line; pH 12) as well as the corresponding qualitative oxygen detection in LiOH at ring electrode at detection potential 0.4 V vs. RHE (circles) at 1600 rpm rotation. The red bullet indicates 1.55 V vs. RHE. Arrows indicate the scan direction. (d) XANES at the Mn-K edge of a pristine sample and one held at 1.55 V vs. RHE (indicated potential) for 1 h showing an edge shift to higher energies, i.e., oxidation.

We gained insight into the manganese redox using hard XAS at the Mn-K edge (Fig. 5.2d). In this spectroscopy, core holes are ejected from the Mn-K shell, which requires a certain threshold energy and produces discontinuities, so-called "edges", in the absorption.[82,

116, 117] The penetration depth depends on the atomic number and density of the sample.[82] A single attenuation length is 5 μm for $LiMn_2O_4$ (crystal density 4.3 g/cm^3)[15, 48] mounted at 45°,[118] which is clearly a factor 100 larger than the mean particle size. Therefore, the bulk of the particles was probed. The X-ray absorption near edge structure (XANES) was recorded for the pristine powder (black line) and a sample, which was held at 1.55 V vs. RHE in 10 mM LiOH for one hour (orange line). The spectrum of the latter sample was shifted by 1 eV toward higher energies at a normalized absorption value of 0.5, which is commonly assigned to manganese oxidation. This interpretation is justified because the nuclei of oxidized atoms are less shielded and thus photons of higher energy are needed for excitation of the core hole. A shift of the order of 1 eV corresponds typically to an increase in the average valence of about 0.4 units (i.e. $Mn^{3.5+}$ to $Mn^{3.9+}$).[83, 119–121] This is a change in the average bulk valence and can thus only be explained by a bulk process for charge compensation. We propose that the process associated with Mn oxidation is delithiation of the bulk. This proposal is supported by the use of $Li_{1-x}Mn_2O_4$ as a battery material in similar aqueous electrolytes.[54, 55, 106, 109–111, 113–115, 122, 123] The manganese valence can be converted to the lithiation value x using the stoichiometries of the formula $Li_{1-x}Mn_2O_4$, i.e., x is twice the absolute valence change. However, the lithiation of $x \approx 0.8$ estimated from XAS after 1 h at 1.55 V (Fig. 5.2d) likely differed from those at 1.55 V during the CV experiment (Fig. 5.2c) due to the time required for Li diffusion through the bulk of $Li_{1-x}Mn_2O_4$. Nonetheless, the XAS experiment clearly demonstrated that the bulk of $LiMn_2O_4$ can oxidize at voltages where the anodic shoulder was found in the CV. Therefore, we assigned the anodic shoulder in 10 mM LiOH to manganese oxidation and the corresponding cathodic peak to manganese reduction. Charge neutrality was ensured in both cases by lithium extraction or insertion at long time scales. We were not sensitive to changes of the surface. Yet, protonation and deprotonation of the surface likely occurred simultaneously as water is weakly buffering at pH 12 (10 mM LiOH)[124] and it can thus accept as well as provide protons. For that reason, we expect that the redox properties and the shape of the CV depend on both the lithium concentration and pH (i.e. proton concentration). In our experiments, both the molarity of Li and the pH changed. Both are intimately coupled in stagnant aqueous solutions as releasing a Li^+ cation into the electrolyte must be compensated by creation of an OH^- anion (assuming water as the only anion source). In our hydrodynamic experiments, they are coupled because the bulk solution contains equal molarities of Li^+ and OH^-. The thermodynamic activity is 0.96 in 1.0 M OH and approaches 1 below pH 13.[125] Therefore, the calculation of the pH from the concentrations is a reasonable approximation. To

simplify the discussion, we use the pH defined as

$$pH = 14 + \log([OH^-]) \tag{5.1}$$

The pH in this report is calculated from the molarity of the prepared LiOH solutions and not measured using conventional glass electrodes as they are inaccurate in LiOH.[125] We decided to discuss the observed changes in terms of pH changes, which are a staple of systematic electrocatalytic experiments. We performed additional RRDE experiments in LiOH electrolytes prepared with pH values between pH 12 (10 mM) and pH 14 (1000 mM) that are shown in Fig. 5.3. The disk scan range was adjusted to clearly evolve oxygen in the anodic range and to completely reduce the particles back to their pristine state (i.e. vanishing current at the end of the cathodic scan). While the same voltage range of 1.25 to 1.75 V vs. RHE was suitable in the range of pH 13 to pH 14, it had to be extended to 0.90 and 1.79 V vs. RHE at the lowest pH 12 (Fig. 5.3a). Moreover, the magnitude and width of the redox peaks clearly depended on the pH where the features were broadest at the lowest pH and vanished at the highest pH. At pH 13, the anodic shoulder appeared to have merged with the onset of currents due to oxygen evolution.

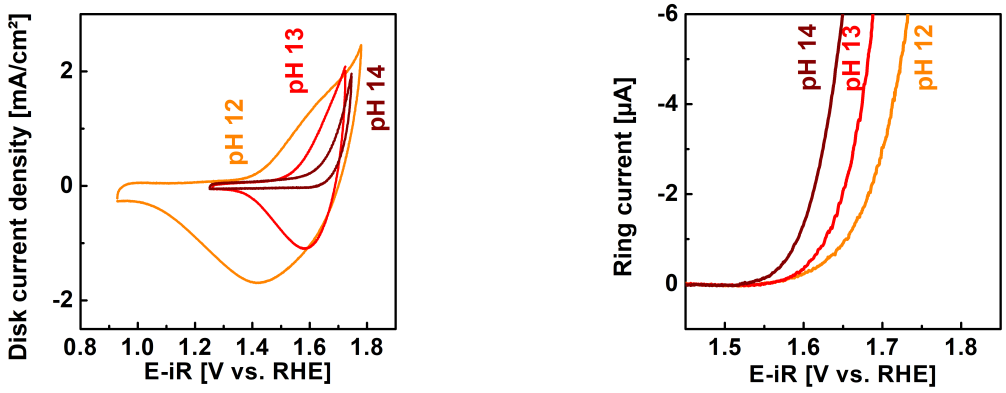

(a) (b)

Figure 5.3.: (a) Representative CV during the 5^{th} cycle at pH 12, pH 13 and pH 14 and (b) corresponding qualitative oxygen detection at ring electrode for these concentrations. For all ring electrode measurements, the detection potential was set to 0.4 V vs. RHE at 1600 rpm rotation (complete dataset in Fig. A.11).

The simultaneously measured ring currents revealed that the onset and kinetics of oxygen evolution likewise depended on the pH (Fig. 5.3b). The ring currents rose exponentially

as expected where the lowest onset was found for pH 14 and the highest for pH 12. We defined the onset potential herein as the ring current at -5 μA. The voltage at this reference changes by -40 mV on average when the pH is increased by one unit (Table A.6), i.e. a change in the OH^- concentration of a factor 10. This shift is the Nernst slope $(\partial \mathrm{E}^{RHE}/\partial \mathrm{pH})_{i=const.}$ on the RHE scale. The solubility of O_2 in hydroxides changes little with concentration in hydroxides,[126] so that we attribute the observed shifts to modifications of $LiMn_2O_4$, which is also supported by differences in the redox peaks. The most likely chemical modification is a change of the lithiation x in the bulk of $Li_{1-x}Mn_2O_4$ as also supported by XAS. Based on the hypothesis of changes in bulk lithiation, we can derive the expected reversible potentials as function of the pH. The derivation is based on earlier work by Li et al.[54]] It is necessary as the plots in literature are derived for a fixed Li molarity[109, 115](often the standard condition of 1 M Li) which was not the case in our experiments and is often not the case in other recent electrocatalytic studies of pH dependence.[48, 127–130] The following reaction holds in equilibrium at the pH when Li^+ will no longer be extracted from $LiMn_2O_4$

$$Li_{1-x}Mn_2O_4 + xH_2O \rightleftharpoons xLi^+_{aq} + xOH^- + x/2H_2 \tag{5.2}$$

We assume that H_2 forms at the (Pt) counter electrode in its standard state (denoted by superscript 0), i.e. 1 bar. Furthermore, water can be considered in its standard state for the used hydroxide concentrations.[125] The chemical potentials are thus

$$\mu_{Li}^{LiMn2O4}(x) + \mu^0_{H2O} = \mu_{Li+} + \mu_{OH-} + 1/2\mu^0_{H2} \tag{5.3}$$

The positive and negative charges in the electrolyte must be balanced, i.e.

$$([Li^+] + [H^+]) = [OH^-] \tag{5.4}$$

Since we study basic solutions (i.e. $[Li^+] \gg [H^+]$), the proton concentration in Eq. (5.4) can be neglected. Assuming full dissociation and no interactions, the chemical potentials of the Li and OH in solution can now be obtained from the Nernst equations using the concentrations rather than activities

$$\mu_{Li} = \mu^0_{Li} + RT/F \cdot \ln([Li^+]) \tag{5.5}$$

$$\mu_{OH} = \mu^0_{OH} + RT/F \cdot \ln([OH^-]) \tag{5.6}$$

Eq. (5.6) can also be rewritten using the definition of the pH in Eq. (5.1) as

$$\mu_{OH} = \mu^0_{OH} + \ln(10)RT/F(pH - 14) \tag{5.7}$$

Combining Eq. (5.3) with Eq. (5.7) and using that [Li^+]=[OH^-], gives

$$\mu^{LiMn2O4}_{Li}(x) = \frac{(2\ln(10)RT)}{F}(pH - 14) + \mu^0_{(Li+)} + \mu^0_{(OH-)} + 1/2\mu_{H2^0} - \mu^0_{H2O} \tag{5.8}$$

The voltage in an intercalation battery is given by the difference between the cathode ($LiMn_2O_4$) and anode (Li)

$$E_{cell} = -1/e(\mu^{LiMn2O4}_{Li}(x) - \mu^0_{Li}) \tag{5.9}$$

where μ^0_{Li} is the chemical potential of lithium metal. The standard chemical potentials correspond to that of the reaction Li + $H_2O \rightleftharpoons$ LiOH + 0.5 H_2, for which the free energy is -2.228 eV/e.[54] At room temperature (T=25°C), ln(10) RT/F equals 59 mV. Using these values, the voltage of the cell (with a Li/Li^+ anode) becomes

$$E_{cell} = 3.88 \text{ V} - 0.118 \text{ V}pH \tag{5.10}$$

The experimental standard potential of $LiMn_2O_4$, $E^0_{LiMn2O4}$, varies to some extend and depends on the synthesis.[111] Therefore, we obtained it experimentally for our powder in a typical battery electrolyte (Fig. A.12). The curve shows a first plateau at $E^{(0,low)}_{LiMn2O4}$=3.996 V vs. Li/Li^+ (i.e. the anode) for lithiation above x≈ 0.5 in $Li_{1-x}Mn_2O_4$ and a second plateau $E^{(0,high)}_{LiMn2O4}$=4.138 V vs. Li/Li^+, which correspond to a one-phase reaction (that of pristine $Li_1Mn_2O_4$) and a two-phase reaction.[131] The half-cell potential of the $LiMn_2O_4$ cathode is thus

$$E_{LiMn2O4} = 3.885 \text{ V} - E^0_{LiMn2O4} - 0.118 \text{ V}pH \tag{5.11}$$

The values of the pH-independent term are -0.111 V and -0.253 V for $E^{(0,low)}_{LiMn2O4}$ and $E^{(0,high)}_{LiMn2O4}$. As the duration of delithiation is rather short during a CV at 10 mV/s, we expect that $E^{(0,low)}_{LiMn2O4}$ is the relevant potential.

This half-cell voltage is expressed relative to the reversible hydrogen electrode (RHE), as we considered both the standard potential and the pH dependence of the solution in Eq. (5.7), which is the very definition of the RHE scale. Moreover, Li et al.[54] have

shown experimentally that the cell potential in a conventional non-aqueous 1 M $LiPF_6$ PC/EC electrolyte and 1 M LiOH electrolyte are nearly identical. The half-cell potential can thus be expressed against the RHE without considering further reactions. Finally, $LiMn_2O_4$ delithiation occurs on the anode in our application and the hydrogen redox on the cathode and so the polarity of the cell must thus be opposite as derived above

$$E^{RHE}_{LiMn2O4} = -0.111\ \mathrm{V} + 0.118\ \mathrm{V}pH \tag{5.12}$$

This equation can now be used to predict whether $LiMn_2O_4$ will delithiate in electrolytes with equal molarities of Li^+ and OH^-; delithiation occurs for all applied voltages $E_{appl} > E^{RHE}_{LiMn2O4}$.

We used Eq. (5.12) and the reversible potential of the OER (1.23 V vs. RHE) to construct an E^{RHE}-pH diagram (Fig. 5.4a). It is related to the more commonly used E^{SHE}-pH (Pourbaix) diagram, that is also used in previous work of aqueous battery work[109, 115], but the thermodynamic potential of the OER, i.e. the O_2/OH^- equilibrium, on the working electrode (black line) is a horizontal line in the E^{RHE}-pH diagram and the experimental overpotential is also a horizonal line if the Nernst slope vanishes, i.e. $(\partial E^{RHE}/\partial \mathrm{pH})_{i=const.}$, which is the expected pH dependence based on common mechanisms with proton-coupled electron transfers.[48, 127] Moreover, the representation in an E^{RHE}-pH diagram is often preferable in electrocatalysis as it allows to read overpotentials with respect to the OER more directly from the plot. Even minor changes of the overpotential are clearly visible in this diagram, whereas they are difficult to read from the classical E^{SHE}-pH diagram.

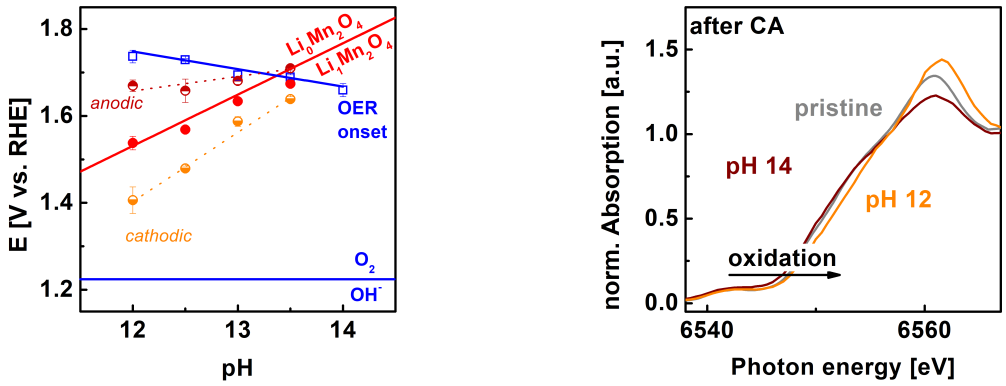

(a) (b)

Figure 5.4.: (a)E^{RHE}-pH diagram of $Li_{1-x}Mn_2O_4$ in LiOH showing the expected (solid red line, Eq. 5.12) and measured (filled circles) reversible potential of delithiation. The half-filled circles and dotted lines were used in the determination of the experimental value (Table A.6). The equilibrium potential of O_2/OH^- (solid blue line) and experimental OER onset determined as the overpotential at -5 μA qualitative ring current (open squares). The dashed line was added as a guide to the eye. Error bars may be too small to be visible. (b) XANES spectra of Mn K-edge of a $LiMn_2O_4$ electrode holding at 1.55 V vs. RHE at pH 12 and pH 14 compared to pristine $LiMn_2O_4$ powder. Edge shifts to higher energies indicate oxidation of Mn.

The kinetic data from the CVs in Figs. 5.3 and A.11 was overlaid onto the E^{RHE}-pH diagram to compare to the predicted thermodynamic lines (Fig. 5.4a). The overpotentials of the OER at -5 μA ring current (blue squares) were taken as an approximation of the onset of oxygen evolution. The kinetic data must have slightly higher potentials as compared to the thermodynamic O_2/OH^- equilibrium due to the kinetic barrier. However, the majority of the offset ($\sim$0.4 V) is often attributed to the so-called scaling relations[21, 54, 132]] between dependent intermediates. Therefore, the experimental data (blue symbols) are found at higher potentials as the thermodynamic potential (blue line). Furthermore, the experimental data clearly depended on pH on an RHE scale with a Nernst slope of -40(4) mV/pH, which clearly differed from our previous study in NaOH where the Nernst slope was -2(1) mV/pH the onset of the OER.[48] The reversible potential of delithiation of $LiMn_2O_4$ was also determined experimentally. For this, we determined the peak potentials as the zero-crossings of the second derivative of the measured data (Fig. A.13).

The analysis was performed separately for the anodic and cathodic shoulder/peaks and their average potentials are shown in Fig. 5.3a between pH 12 and 13.5. for higher pH values, no shoulders or peaks were detected. We had assigned the anodic shoulder to Mn oxidation above +3.5 and the cathodic peak to Mn reduction back to about +3.5. The difference between the anodic and cathodic potentials decreases from 260 mV at pH 12 to 71 mV at pH 13.5 in the resistance-corrected data. Thus, we attribute the diminishing difference in shoulder/peak potentials to better reversibility[133] of lithium extraction and re-insertion at higher LiOH concentrations, i.e. closer to standard conditions. The reversible potential was determined as the midpoint potentials of the anodic and cathodic shoulders/peaks (red symbols), i.e. their average. The determined midpoint potentials fall onto the line predicted by Eq. (5.12) within error, except for pH 13.5 because it was too close to the intersection of the OER onset (see below). Thus, we confirmed that the assumptions and simplifications made in the derivation are valid and reasonable for our application. Our E^{RHE}-pH diagram can be used to predict whether $LiMn_2O_4$ will retain its bulk valence of +3.5 during electrolysis in LiOH electrolytes, which is important for the stability and activity of the electrocatalyst. The fit line to the experimental oxygen evolution data of the ring electrode intersects that of the (de/-)lithiation reaction (Eq. 5.12) slightly below pH 13.5. Had we read the voltages at a lower ring current, then the intersection would occur at a slightly lower pH value. This intersection is highly significant because oxygen evolution (blue symbols and line) should be performed at potentials where Li cannot be extracted from $LiMn_2O_4$ (red symbols and lines). Otherwise, the Mn on the surface and in the bulk of $LiMn_2O_4$ oxidize. The E^{RHE}-pH diagram suggests that measurements at pH 12 in LiOH lead to significant Mn oxidation (as discussed above), while those at pH 14 should retain their valence. The expected bulk valences were again investigated by hard XAS at the Mn-K edge (Fig. 5.4b). A dense pellet of optimized loading was prepared and measured in transmission mode (grey line). It showed a pre-edge at 6540 eV, a shoulder at 6550 eV and maximum (white line) at 6560 eV. The shape of a XANES spectrum depends on the local geometric and electronic structures of the absorbing atom.[134] It is not straightforward to interpret and requires extensive theoretical calculations that are beyond the scope of this manuscript. Here, we only compare spectral differences among the samples. The measurements of the $LiMn_2O_4$ electrodes had to be made in fluorescence yield (FY) mode due to the comparably low loading required by the electrocatalytic measurements. The FY mode only approximates an X-ray absorption spectrum[82, 135] and depends on the measurement geometry. Nonetheless, the spectrum of a sample held at 1.55 V vs. RHE for 1 h at pH 14 is congruent with

the pristine sample and only deviates at the maximum near 6560 eV, where lower amplitudes are a common artefact of FY measurements.[136, 137] Thus, we conclude that the bulk material was not changed at 1.55 V in LiOH at pH 14 and in particular retained an average valence of +3.5. In contrast, the sample held at the same potential at pH 12 differed clearly, namely, the shoulder was less pronounced, the edge shifted to higher energies and the maximum clearly increased. Overall, the XAS measurements confirmed our predictions from the E^{RHE}-pH diagram. In particular, the $LiMn_2O_4$ sample measured at pH 14 retained its bulk valence. The Mn valence has been correlated with the activity for the OER previously.[120, 138–141] In a more detailed picture, the (bulk) e_g occupancy has been proposed to correlate with activity[107] where an occupancy near unity results in the lowest overpotential. The rationale is that the electron density of the e_g orbital points towards the absorbing oxygen, which is a key step in the mechanism.[21, 127] For spinels, including $LiMn_2O_4$ and several closely related spinels, the (bulk) e_g occupancy of the octahedral site has been proposed to correlate with the overpotential.[24] In the simple crystal field splitting model of manganese oxides with valences between +2 and +4, they contain 3 (spin up) electrons in the t_{2g} orbitals and the e_g orbital fills up (with spin up) electrons from 0 (Mn^{4+}) to 1 (Mn^{3+}) to 2 (Mn^{2+}).[142] Based on the previous studies of the e_g occupancy, Mn^{3+} (e_g occupancy of 1) is desirable in an electrocatalyst for the OER. However, a single parameter does not fully describe the catalytic properties of a material as complex as an oxide.[21, 32, 40, 41, 143] Mixed manganese valences between Mn^{3+} and Mn^{4+} result in the highest activity, i.e. lowest overpotential, in many reports.[9, 40, 96, 138, 143–148] Therefore, retaining the $Mn^{3.5+}$ valence of the pristine $LiMn_2O_4$ is crucial for sustained electrolysis with unchanged activity. The observed increase of the OER overpotential from pH 14 to pH 12 in LiOH can now be explained in the context of changed manganese valence. The available literature data suggests that oxides with Mn valences slightly above Mn^{3+} have higher activity than those with lower or higher manganese valence.[24, 107] We have calculated the conditions, for which Mn reduction is expected (Fig. 5.4a) and verified it experimentally for selected points (Fig. 5.4b). Therefore, we conclude that the overpotential increased in electrolytes below pH 14 due to bulk delithiation, which oxidizes the Mn in the bulk of $LiMn_2O_4$ above average valences of +3.5. It is often assumed, especially in theoretical work,[149] that the overpotential does not depend on pH, which is sometimes not the case in experimental studies.[127, 150] The origin of this effect is not well understood. While there are probably also other triggers of the effect, our work clearly demonstrates that changes in the bulk valence can induce pH dependency on the RHE scale, i.e. non-Nernstian behavior, as witnessed by a non-zero

Nernst slope ($\partial E^{RHE}/\partial$pH). The same pH dependence was reported for materials that (de/-)intercalate oxygen.[128] While few currently studied electrocatalysts will intercalate or deintercalated ions in the voltage range and electrolyte composition where the OER is studied, the classical E^{SHE}-pH (Pourbaix) diagram predicts valence changes for many used oxides, e.g. simple manganese oxides[151, 152] and they were also observed experimentally by in situ XAS.[84, 153–158] It is thus likely that many oxides, particularly manganese oxides, show non-zero Nernst potentials when they are oxidized or reduced in the investigated electrolytes.

5.3. Conclusion

We investigated the effect of bulk oxidation on the overpotential of $LiMn_2O_4$ as an electrocatalyst for the OER in LiOH electrolytes with pH between 12 and 14. We found pronounced redox peaks in LiOH electrolytes with pH $\leq$ 13.5 that were not observed at pH 14 and in all previous reports where NaOH and KOH electrolytes were used.[15, 24, 45, 48] Using XAS at the Mn-K edge, we showed that Mn in the bulk of $LiMn_2O_4$ oxidized at pH 12, which we used to assigned the observed peaks and shoulders to the $Mn^{3.5+}$-$Mn^{3.5+\delta}$ redox. As the XAS measurement was bulk sensitive, we argued that the most likely process of charge compensation was delithiation of the bulk. The current due to oxygen evolution could not be determined from the total disk currents due to interference of these Mn redox peaks. Yet, the ring of the used RRDE setup qualitatively measured the onset of oxygen evolution, which occurred at voltages higher than that of the Mn redox. The onset of the OER was pH-dependent on the RHE scale with a Nernst slope of -40 mV/pH at -5 μA (uncalibrated) ring current. We derived a simple model for the expected reversible potentials of delithiation for the used electrolytes with equal molarities of Li^+ and OH^-. The calculation of the expected delithiation potentials needs the standard potential of $LiMn_2O_4$ delithiation, which we determined experimentally in a common battery electrolyte as 3.996 V vs. Li/Li$^+$ below x=0.4 in $Li_{1-x}Mn_2O_4$. The predicted Nernst slope of delithiation of 118 mV/pH was identical to the experimental Nernst slope of 116(25) mV/pH within error. The model and experimental data of both delithiation and oxygen evolution were used to construct an E^{RHE}-pH diagram. The lines given by the Nernst slopes of the onset of the OER and that of delithiation intersect near pH 13.5. The E^{RHE}-pH diagram illustrates that delitihation occurs at voltages below that of the onset of OER at pH below about 13.5 while the onset of OER has a lower onset at higher pH. This is significant because the average bulk valance of $Mn^{3.5+}$ will only be retained

at pH above about pH 13.5, which we verified experimentally using XAS on a $LiMn_2O_4$ electrode operated at pH 14. Overall, the model and experimental data strongly support bulk delithiation of $LiMn_2O_4$ below a pH of about 13.5. We discussed Mn oxidation due to delithiation in the context of the e_g orbital descriptor, where oxidation above $Mn^{3.5+}$ should increase the overpotential for the OER. Therefore, we concluded that bulk delithiation and the concomitant oxidation of $Mn^{3.5+}$ to $Mn^{3.5+\delta}$ increased the overpotential of the OER and were the origin of the pH dependence on the RHE scale. The E^{RHE}-pH diagram in our work provides an intuitive graphical tool to gauge the stability of electrocatalyst against redox changes when they are not measured under standard conditions, i.e. 1 M LiOH. While it is most straightforwardly extended to predict the pH dependence of other electrocatalysts that are also common battery materials, e.g., $LiCo_{1-x}MxO_2$ and $LiCoPO_4$,[159–163] oxidation due to structural changes should also show pH dependence on the RHE scale, e.g., Risch et al.[31] showed that the Nernst slope of the $Co^{2/3+}$ redox couple differs from that of the $Co^{3/4+}$ redox couple. Therefore, pH dependence on the RHE scale (i.e. non-Nernstian behavior) should be expected when the electrocatalyst is not stable against redox changes in the investigated electrolyte.

5.4. Experimental Section

5.4.1. Materials

$LiMn_2O_4$ (>99%) catalyst powder was purchased from Sigma-Aldrich. Tetrahydrofuran (THF) was purchased from VWR (≥99.9% stabilized). For the electrolyte Lithium hydroxide powder (99%) purchased from Merck was dissolved in ultrapure water (Milli-Q R ≥18.2 MΩ). Argon (5.0) to purge the electrolyte was purchased from AirLiquide Alphagaz. Acetylene carbon black was purchased from Alfa Aesar and was acid-treated.[107] All other chemicals were used as received.

5.4.2. Characterization

The pristine powder was also characterized by a XRD Bruker D8 Discovery with monochromatized Cu-Kα radiation in a two theta range of 15°-85° in 0.05° steps. For this, the $LiMn_2O_4$ powder was glued using rubber cement (Fixo Gum, Marabu GmbH) on a microscope slide made of glass. The particle distribution was determined by Nova Nano SEM 650 in high vacuum mode at 15 kV. Both results were in good agreement with our

previous publications[11, 48] and are shown in the supporting information.

5.4.3. Electrochemical setup

For our electrochemical experiments we were using an OrigaFlex (OrigaLys SAS) system of three OGF500 potentiostats in bipotentiostat configuration. The RRDE-setup was composed of an RRDE-3A rotator (ALS Japan Co Ltd.) and a custom-made cylindrical PTFE cell that was used in a three-electrode configuration, consisting of a saturated calomel electrode (RE-2B, ALS Japan Co Ltd.) and a platinum counter electrode, which were arrange radially around the working electrodes. The distance between the RRDE-electrode and counter and reference electrode was 17 mm. We used a RRDE-electrode made by ALS Japan Co Ltd containing of a removable glassy carbon electrode 4 mm in diameter (area 0.126 cm^2) and a concentric platinum ring electrode with 5 mm inner and 7 mm outer diameter separated by a Teflon spacer. Both working electrodes were separately polished to a mirror finish with Al_2O_3-polish on separate polishing pads and cleaned afterwards with isopropanol. After this cleaning procedure the RRDE was assembled from both parts. This procedure reduces a possible contamination of the electrodes. A RHE (Hydroflex, Gaskatel GmbH) was used to calibrate the SCE to RHE scale.[15] For XAS measurements we used graphite foil (Alfa Aesar 99.8%) as the electrode instead of a glassy carbon in the RRDE-setup.

5.4.4. Electrochemcial experiments

For catalytic experiments we realized a loading of 50 μg active material on a glassy carbon electrode by drop coating. For this, we applied 10 μL of an ink containing of $LiMn_2O_4$ (83% of solid part) and carbon black (17% of solid part) in THF. The Teflon spacer of the RRDE assembly prevents the ink from contacting the ring electrode. If it happed by accident, the electrode was discarded. The electrolyte was saturated with argon gas. For RRDE-measurements, we used a rotation speed of 1600 rpm. The detection potential for the detection of oxygen was determined in our previous work.[15] Our protocol includes an impedance measurement from 100 KHz to 1 Hz at the open circuit potential. The ohmic resistance for the iR correction was obtained from this measurement at high frequency where the phase angle approached zero. Additional detail on the used protocol may be found in the supporting information.

5.4.5. Sample preparation for post-mortem chatacterization by XAS

For XAS measurements the catalytic ink was applied on a graphite foil and a CA at 1.55 V vs. RHE was performed for one hour in a LiOH electrolyte with pH 12 or pH 14. Afterwards the electrode was washed off with Milli-Q water, dried and transferred to the beamline. To characterize the pristine powder by XAS, we diluted the powder to 1-wt% of Mn in $LiMn_2O_4$ using BN. After these powders have been homogenized by a mortar and pestle, a pellet of 10 mm in diameter was pressed at 20 bar. This pellet was transferred to the beamline.

5.4.6. XAS measurements

XAS measurements of post mortem samples were performed in fluorescence mode (detector: Bruker X-Flash 6|60) at the KMC-2 beamline of the BESSY II synchrotron in Berlin. The beamline energy resolution is 1/4000. The acquisition time for one EXAFS scan takes around 90 min. The used beam size was around 2 mm x 4 mm (hor. x vert.). The first inflection point in the XANES of a manganese foil was used for the energy calibration by setting it to 6539 eV. XAS measurements of the pristine powder were performed in transmission mode at CLÆSS beamline of ALBA synchrotron in Barcelona. The used beam size was around 1 mm x 1 mm. We also used a manganese foil for energy calibration. All XANES spectra were normalized by subtraction of a straight line before the edge and division of a polynomial after the edge.

Acknowledgements

The authors are thankful for funding by the collaborative research center (CRC) 1073 (SFB 1073, project C05) sponsored by the Deutsche Forschungsgemeinschaft (DFG). We thank HZB for the allocation of synchrotron radiation beamtime. Other synchrotron experiments were performed at the CLÆSS beamline at ALBA Synchrotron with the collaboration of ALBA staff.

6. Correlation of Manganese valence on OER activity

Oxidation by delithiation of a $Li_xMn_2O_4$ model catalyst for the OER causes an increase in the Faradaic efficiency concurrenting a decrease in catalytic activity

Abstract: We investigated a $Li_xMn_2O_4$ (x=1, 0.51 and 0.25) model catalyst for the water oxidation reaction in sodium hydroxide in different Mn oxidation states by a RRDE setup. These oxidation states were realized by a controlled electrochemical delithiation process and were determined by complementary XAS and XRD. These findings of electronic and structural properties of the bulk and the catalyst's surface were correlated with the OER activity. Although, the overall catalytic activity decreases, we could unravel a different catalytic behaviour of the modified material ($x \leq 1$) in comparison to the initial catalyst (x=1), as the initial disk current decay for the modified particles depends on the crumbling catalytic activity over the cycles and not anymore on the Mn loss during the first cycles as for the initial (x=1) particles. Thereby, we found that the Faradaic efficiency increases from 75(2)% to 96(5)% in dependence with a decrease in the lithium content (i.e. oxidizing manganese), as the manganese corrosion's impact on the total disk current gets negligible. These findings could be a pathway to a deeper mechanistic understanding of catalysing the OER, as it identifies catalysts, which may be catalytically less active but have a negligible side reaction contribution, i.e. only produces the preferred product (here oxygen) with no interferences from side reactions.

6.1. Introduction

The usage of manganese oxides as catalysts for the OER (oxygen evolution reaction) is a wide field in current research, due to their rich redox chemistry.[138] The influence of the electronic and structural properties are extensively discussed in order to create models, which predicts catalytic activity.[7–9, 13, 38, 39] Suntivich et al. correlated the catalytic activity of perovskites with the e_g occupancy and predicted the highest activity at around e_g^1.[10] Wei et al. expanded this model to spinel oxides by identifying the octahedral side as the catalytically active and its e_g occupancy.[24] Sun et al. described the catalytic activity of oxide spinels as a covalency competition of the lattice motif $M_{octahedral}$-O-$M_{tetrahedral}$ as the bottleneck, as a bond breakage is needed to start a catalytic cycle.[12] A promising material to investigate the catalytic activity in dependence of the valence state is $Li_xMn_2O_4$. The benefit of this material is the possibility to modify its valence in a regime from +3 to +4 by (de)lithiation through battery techniques, without changing its nominal manganese bonding environment. Its catalytic performance in alkaline solution is already discussed.[14–16, 46–49]

Previously, we reported about the influence of nano and micron-sized $LiMn_2O_4$ particles on the OER activity and thereby the origin of the total disk current. This enabled us to deconvolute the disk current to all (side) reactions — i.e. the current contribution due to oxygen evolution, corrosion and Mn redox.[15] Besides, we published a study about the stability of $LiMn_2O_4$ in different concentrated lithium hydroxide electrolytes and that this electrolyte could cause a bulk oxidation by delithiation for low concentrated electrolytes. This delithiation process has a disastrous impact on the needed overpotential of the OER.[16] The undesired bulk oxidation of $LiMn_2O_4$ in this specific electrolyte is in a good agreement with the descriptor models for the OER. However, to describe the behaviour of the catalysts in all its side reaction is often ignored. Although, this could provide beneficial insights in the mechanisms of the OER. Here, we catalyse the OER in sodium hydroxide electrolytes and use $Li_xMn_2O_4$ with different contents of lithium (x), which causes different average Mn-oxidation states (+3.5, +3.74, +3.87). Additionally, we could also determine a slightly reduced Mn-oxidation state of the surface by surface sensitive total electron yield (TEY) experiments, which was confirmed by STEM-EELS. This modification of the valence state was achieved by a controlled electrochemical extraction of lithium by applying a constant current for a defined time. The so synthesized material was characterized by XAS, XRD, TEM and the catalytic behaviour by RRDE, in which the ring electrode was used to detected oxygen and manganese. By using a

linear regression to determine the current contribution of the oxygen detection and the manganese loss reaction as the sum of the total disk current as establish in one of our previous studies[15], we were enabled to describe the behaviour of delithiated $Li_xMn_2O_4$ catalyst to gain further insights in the mechanism catalysing the OER.

6.2. Results and discussion

In this study we use a nano-sized commercial $Li_xMn_2O_4$ powder in its initial state (x=1) as catalyst for the OER and as starting material for the electrochemical delithiation $Li_xMn_2O_4$ (x≤1) (Fig. 6.1).

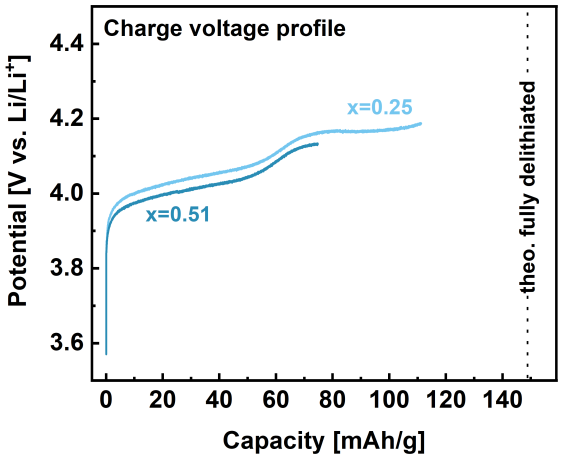

Figure 6.1.: Charge voltage profiles using a C/12 rate - here this technique is used for the synthesis of the modified catalyst $Li_xMn_2O_4$. The capacity is indicating the transferred charge. As the theoretical total possible transferable charge to remove all lithium of $Li_1Mn_2O_4$ is 148.07 mAh/g.

By removing lithium from this compound, we have a direct access to the electronic structure of manganese without changing its nominal bonding environment. As reported in our previous publication[15] we determined the particle distribution by SEM with a mean diameter of 44(14) nm. In a first step the initial material was characterized by XRD, XAS and EELS to gain insights into electronic and structural properties. To determine the manganese valence state of the catalyst material, we performed XAS experiments on different manganese oxides (Fig. 6.2a) with a defined oxidation state, which was correlated

with the photon energy of the edge position. The edge energy was determined by the step integral method.[83] Thereby, we were able to establish a calibration curve (Fig. 6.2b) by fitting the edge energy over the oxidation state for these manganese oxides.

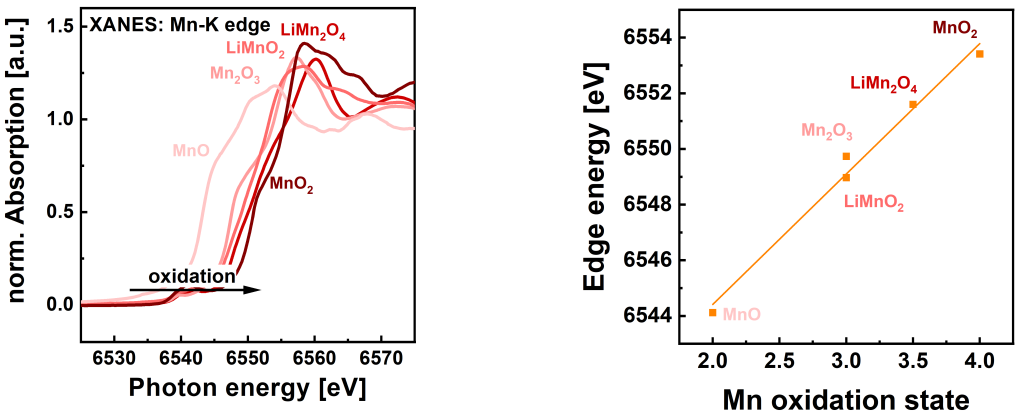

(a) (b)

Figure 6.2.: (a) XANES spectra of Mn-K edge for different manganese oxides: MnO(Mn^{2+}), Mn_2O_3(Mn^{3+}), $LiMnO_2$(Mn^{3+}), $LiMn_2O_4$($Mn^{+3.5}$) and MnO_2(Mn^{+4}) with a 1-wt% loading of manganese. Edge shifts to higher photon energies with respect to higher oxidation state (b) linear fit to determine a calibration curve of these spectra (Eq. 6.1) R^2=0.98

This calibration curve (Eq. 6.1) enables us to determine in a next step the oxidation state of the synthesised $Li_xMn_2O_4$ particles using XANES.

$$E_{edge} = 2.82 \cdot oxidation\ state + 6541.62\ \text{eV} \tag{6.1}$$

Besides, as recently published[60] the lattice constant (a) of the $Li_xMn_2O_4$ spinels shrinks linearly from 8.234 Å(x=1) to 8.0434 Å(x=0). Thus, the following connection between the lattice constant and the lithium content is given by equation 6.2.

$$a = 0.1906 \cdot x + 8.0434\ \text{Å} \tag{6.2}$$

Hence, we used the lattice constant to calculate the lithium content and thereby the manganese valence is a complementary approach, besides XAS. In figure 6.3a the X-ray diffractograms of the initial material as well as of two electrochemically delithiated powders are shown.

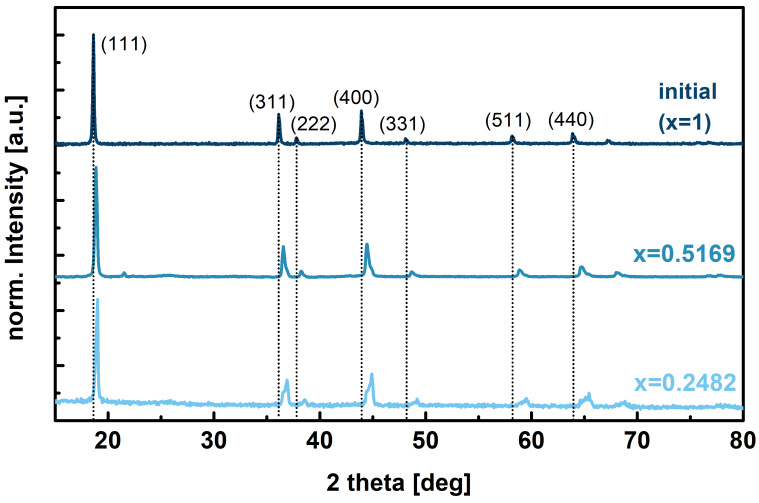

(a)

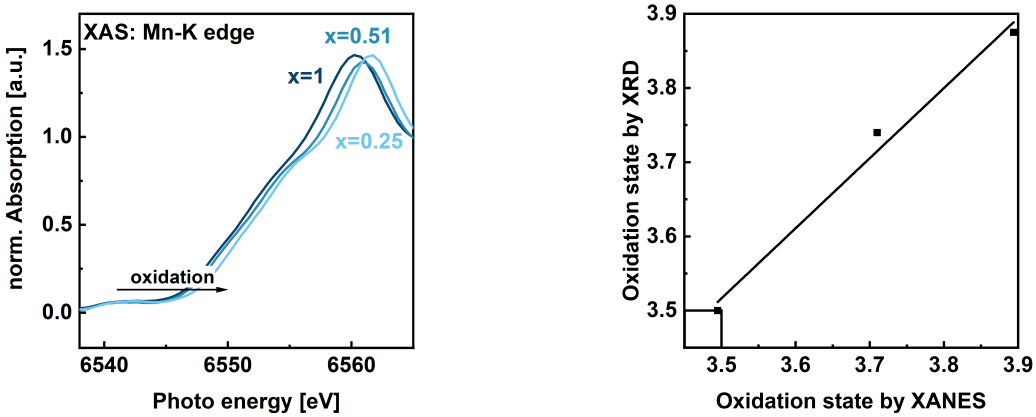

(b) (c)

Figure 6.3.: (a) Indexed X-ray diffractogram of pristine and modified $LiMn_2O_4$ particles, peak shift indicates a decrease in the lattice constant and thereby a delithiation (vertical lines to guide the eye of the peak position) (b) XANES of the Mn-K edge of these particles confirms oxidation by edge shift to higher energies (c) Oxidation state determine indirectly by the lattice constant by XRD over the oxidation state determine by position of the Mn-K edge by XANES, the linear fit has the slope = 0.94 (same ratio of x and y axis as indicated by inserted square)

The reflection peaks of the modified samples are clearly shifted to higher angles with

respect to the pristine material, which indicates a shrinkage of the lattice constant as a result of lithium extraction. Additional XANES of the Mn-K edge (Fig. 6.3b) of the same samples shows an edge shift to higher energies and thereby an oxidation of the manganese. We could confirm, that the average oxidation state of the samples, determine by XRD and XAS are in a good agreement (Fig. 6.3c). The resulting oxidation states of these two methods are shown in table 6.1.
However, as shown by Schönewald et al.[14] the here used $LiMn_2O_4$ particles in its initial state (x=1) have a core-shell behaviour with a reduced surface with respect to the volume. Therefore, additional soft XAS experiments of the Mn-L edge on calibration samples were performed (Fig. 6.4a), as TEY and the L-edges are more surface sensitive.[164] To resolve the peak energy, the L_3-peak was fitted with a Gaussian and correlated with the defined manganese valence state of the reference samples. The resulting calibration curve of the Mn-L_3 edge (Fig. 6.4b and Eq. 6.3) to determine the oxidation state was established. For the recorded soft-XAS spectra of the here used initial and modified material (Fig. 6.4c), the resulting peak position of the L_3-edge as well the resulting oxidation state are documented in table 6.1.

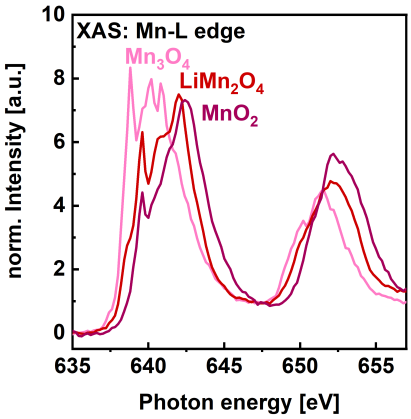

(a)

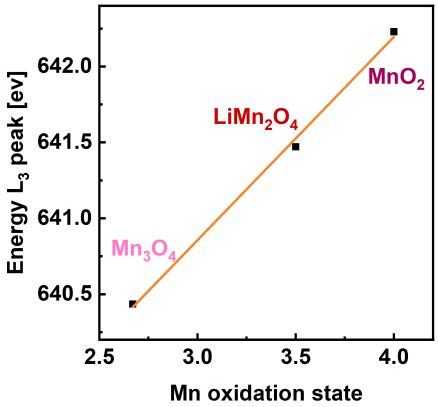

(b)

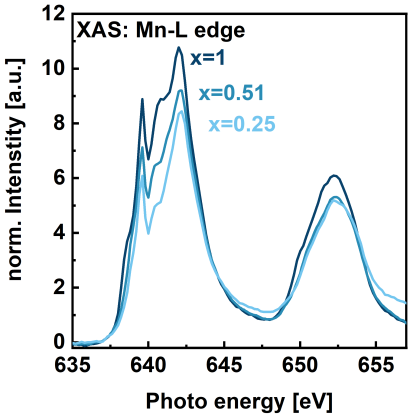

(c)

Figure 6.4.: (a) Soft-XAS of spectra of the Mn-L edge of calibration samples Mn_3O_4 ($Mn^{+2.67}$), $LiMn_2O_4$ ($Mn^{+3.5}$) and MnO_2 (Mn^{+4}) (b) calibration curve (R^2=0.99) to determine the manganese valence state by soft-XAS using the fitted peak position of the L_3 peak from these spectra (c) XAS of the Mn-L edge the here used samples

$$E_{peak} = 1.3388 \cdot oxidation\ state + 636.84\ \text{eV} \tag{6.3}$$

Thereby, we could confirm a lower valence state for the surface with respect to the bulk (Tab. 6.1). In table 6.1 we provide an overview about the manganese valence state de-

termine by different techniques. We could also confirm the core-shell behaviour which was recently observed by Schönewald et al.[14] for the pristine particles (x=1) for the electrochemically modified particles.

Table 6.1.: Determination of manganese valence of the $Li_xMn_2O_4$ samples by XRD, hard XAS and soft XAS

Sample	Lattice constant [Å]	Valence by Li content via lattice constant	Edge Energy (Mn-K) [eV]	Avg. valence by transmission	Peak Energy of Mn-L_3 [eV]	Avg. valence by TEY
pristine (x=1)	8.2340	+3.5	6551.475	+3.495	641.4709	+3.45
x=0.5169	8.1419	+3.74	6552.082	+3.71	641.7675	+3.68
x=0.2482	8.0907	+3.875	6552.553	+3.877	641.7947	+3.70

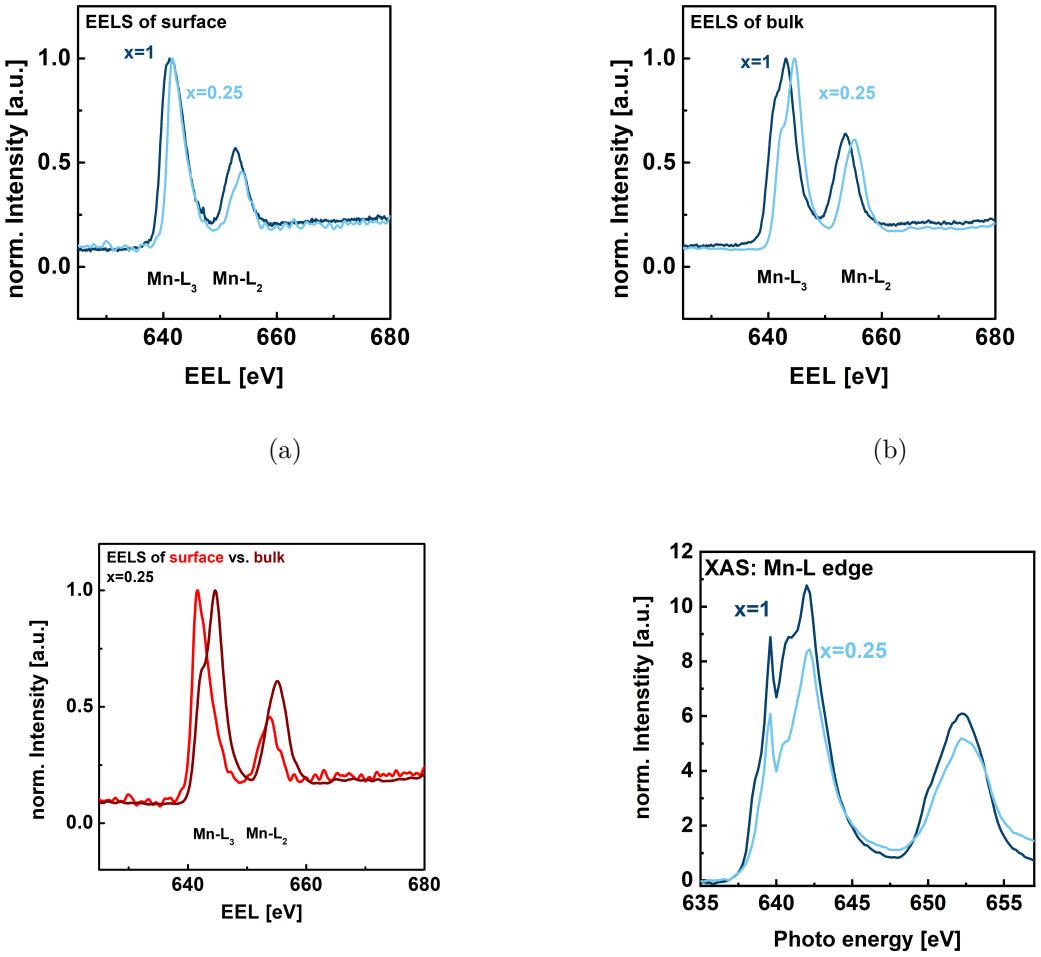

Figure 6.5.: STEM-EELS investigation (by F. Schönewald) of (a) as prepared $Li_{0.25}Mn_2O_4$ sample of the surface and (b) of the bulk (c) ELLS of the surface and the bulk of a $Li_{0.25}Mn_2O_4$ particle, the difference in the Mn-L_3/L_2 position indicates and reduced surface with respect to the bulk (d) XAS of the Mn-L edge of the $Li_{0.25}Mn_2O_4$ sample in comparison to the initial material as an additional technique to EELS (of subfigure (a))

As shown in figure 6.5a and b the surface and the bulk of the delithiated material is oxidized, as indicated by the shift of the Mn-L_3 and L_2 edge to higher energies and confirms the initial XAS and XRD analysis. However, this overall trend is even more pronounced for the bulk of the material (Fig. 6.5b). A closer look at the differences in the oxidation state of the surface in comparison to the bulk of the particles (Fig. 6.5c) reveals a core-shell

behaviour. This behaviour was already reported for the initial particles by Schönewald et al..[14] The soft-XAS of the Mn-L edge (Fig. 6.5d).[164] also indicates an oxidation with respect to the initial material by the shift to higher energies. Besides, the shoulder of the L_3-edge at around 642 eV of the initial material confirms the mixed manganese valence of +3/+4. These findings may indicate, that the reported core-shell structure of the initial material sustains the electrochemical delithiation process and that the reported Mn_T^{2+} is likely not removed by the delithiation reaction. However, it cannot be excluded.

In a next step we evaluated the catalytic performance of the material by RRDE in a 0.1 M sodium hydroxide electrolyte to correlate the activity with the electronic and structural properties and compare these with the modified catalyst.

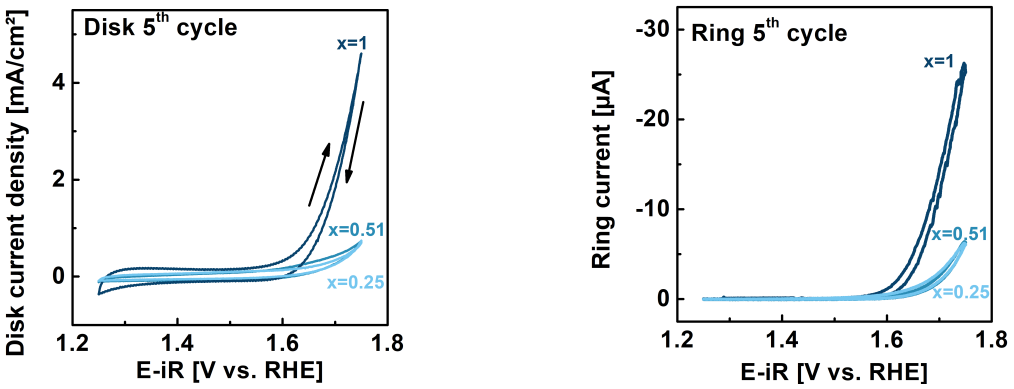

(a) (b)

Figure 6.6.: (a) 5^{th} cycle of the disk of all used catalyst materials in NaOH (0.1 M) and (b) corresponding ring data of the oxygen detection

The catalytic performance of the here used $Li_xMn_2O_4$ samples (x=1, 0.51 and 0.25) (Fig. 6.6) were determine by RRDE in sodium hydroxide (0.1 M). Therefore, a CV was performed at the disk electrode in a range from 1.25 to 1.75 V vs. RHE, while the ring electrode was set either to detect oxygen to evaluate the activity or to detect manganese to evaluate the stability.[15] As an overall trend, the disk current density decreases and the onset of exponentially increasing catalytic current is shifted to higher overpotential. These findings are in agreement with different descriptor models, to predict catalytic activity.[10, 24] However, the differences between $Li_{0.51}Mn_2O_4$ and $Li_{0.25}Mn_2O_4$ seems to be small, while the differences between the initial material and the modified particles is

drastic.

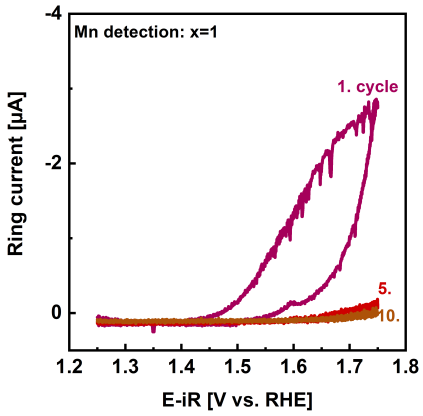

(a)

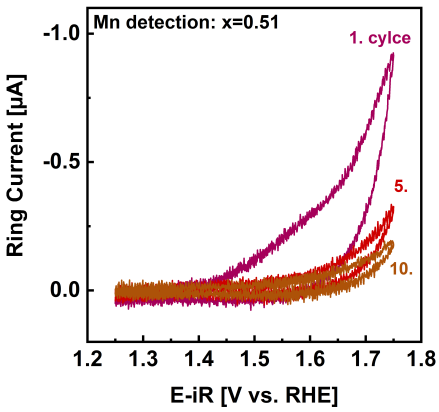

(b)

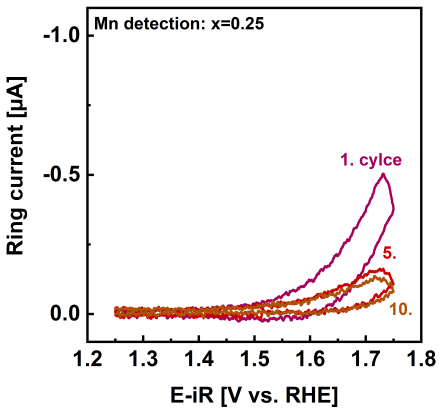

(c)

Figure 6.7.: Manganese detection at the ring electrode for the 1^{st}, 5^{th} and 10^{th} cycle of (a) $Li_1Mn_2O_4$ sample (b) $Li_{0.51}Mn_2O_4$ sample and (c) $Li_{0.25}Mn_2O_4$ sample

The ring current due to manganese loss (Fig. 6.7) decreases over all ten cycles for all samples in different lithiation state. While for the delithiated material the current is almost negligible and in the range of nano ampere, which indicates that the manganese loss for this material is much smaller in comparison to the initial material (x=1). Although, the shape of the manganese detection current in figure 6.7b may suggest an influence of crosstalk between both working electrodes (disk and ring). We performed an experiment in a quiescent electrolyte with the detection potential set to manganese.[15] Thereby, we

can exclude any electronic crosstalk between these two electrodes (Fig. A.8b). As we cannot exclude, that the by EELS discovered Mn_T^{2+} layer at the surface of the initial material (x=1) is affected by the electrochemical synthesis, a removal of this layer during the synthesis may explain the decrease in the manganese detection current at the ring electrode for these samples.

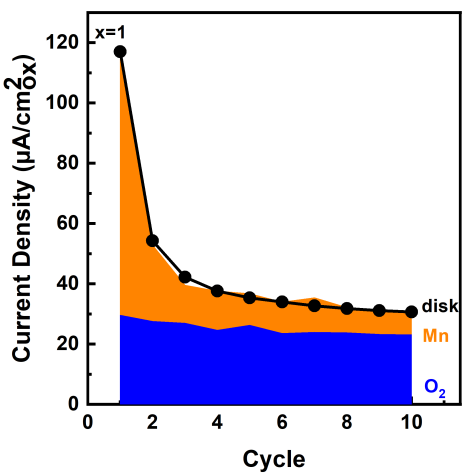

(a)

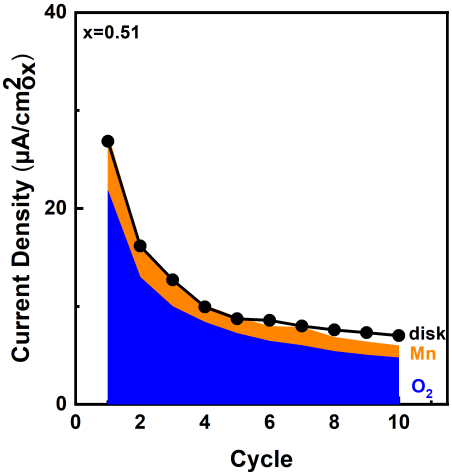

(b)

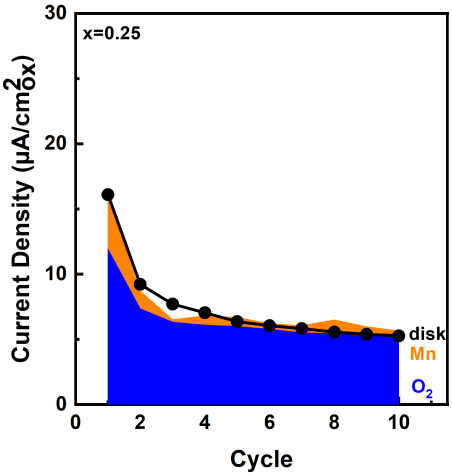

(c)

Figure 6.8.: Origin of the total disk current: calculated current contributions due to oxygen evolution (blue) and corrosion of manganese (orange) to the total disk current (black) at a reference potential of 1.68 V vs. RHE: (a) initial material (x=1) (data set reproduced from [15]) and for delithiated samples (b) x=0.51 and (c) x=0.25 — current normalized to ECSA by 5.26 cm^2_{ox}[15]

As demonstrated in our previous publication [15] we were able to determine the origin of the total disk current under the assumption, that it is the sum of at least two different

processes which products could be detected at the ring electrode — i.e. oxygen and manganese. Although, the measured ring currents are only qualitatively, the high number of reproduction (Fig. A.14-A.16) and cycles enables us to use a linear combination analysis of the disk current density, under the assumption of equation 6.4.

$$j_{disk} = c_{O2} \cdot j_{R,O2} + c_{Mn} \cdot j_{R,Mn} + c_x \cdot j_x \tag{6.4}$$

Here, c_{O2}, c_{Mn} are the coefficients (Tab. A.8) for the measured reactions (oxygen evolution and manganese corrosion) and c_x as a possible third unknown side reaction. For the analysis, the measured ring currents $j_{R,O2}$ and $j_{R,Mn}$ were used at a corresponding disk potential of 1.68 V vs. RHE. For these ring currents, we can also exclude, that the observed detection current at the ring electrode is influenced by saturiating effect of the electrolyte with these reaction products, as the current is continuously increasing for higher potentials than the reference potential, up to the maximum scanning potential.
Thereby, we could confirm that the total disk current decay of the initial $Li_1Mn_2O_4$ catalyst is caused by the manganese loss during the first cycles while the oxygen detection is at an almost constant level (Fig 6.8a). This manganese loss was assigned to catalytically inactive Mn_T^{2+} [14]. A contrary trend is observed for the modified material, here the disk current decay was assigned to the decrease of the oxygen detection current. As shown in the ring data for the manganese detection for these materials the current decreases with the number of cycles. This different behaviour of the modified material also influences the Faradaic efficiency (Eq. 6.5) as the manganese loss current in the order of nano ampere gets negligible.

$$r_f = \frac{c_{O2} \cdot j_{O2}}{j_{disk}} \tag{6.5}$$

Therefore, the Faradaic efficiency (r_f) increases from 75(2)% for the initial catalyst (x=1) to 96(5)% for the delithated catalyst (x=0.25) as an average over the cycles 4-10, after the initial disk current decay.

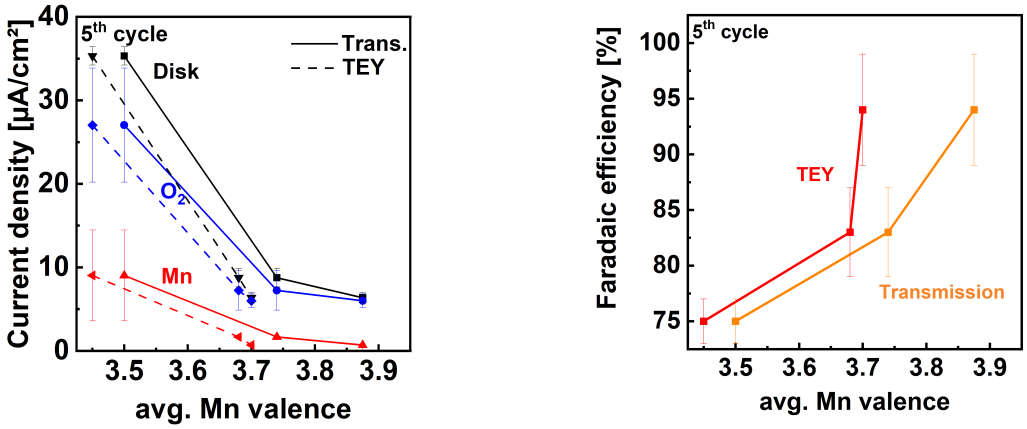

(a) (b)

Figure 6.9.: (a) Disk and Ring current at a reference potential of 1.68 V vs. RHE correlated with the manganese valence determine by transmission XAS of the Mn-K edge (solid line) and by TEY experiments of the Mn-L edge (more surface sensitive) dashed line (b) Faradaic efficiency for the three samples correlated with the Mn valence determine by these two techniques

Further, we used the resulting information of the origin of the total disk current of the fifth cycle to correlate the activity with the manganese valance state to describe the behaviour of the initial and modified catalyst in detail (Fig. 6.9a). As expected from literature [7–9, 13, 16] the disk current decreases in dependence with the lithium content of $LiMn_2O_4$. The model of Sun et al.[12], which focuses on the covalency of the $Mn_{Oct.}$-O-$Li_{Tet.}$ lattice motif of this material, is also in good agreement with our finding, as the delithiation reaction causes a smaller band distance of the manganese d-band to the oxygen p-band, i.e. the stronger bond is unlike to break and create an active site to start a catalytic cycle. In contrast to these extensively discussed publications [10, 24], this plot contains in addition to the disk current also the oxygen detection current and the detection current due to manganese loss. However, the detection of oxygen for $Li_{0.51}Mn_2O_4$ ($Mn^{3.74+}$) and $Li_{0.25}Mn_2O_4$ ($Mn^{3.88+}$) are only slightly different. Besides, the more surface sensitive TEY valence data provide a linear activity correlation, which makes it more suitable as a descriptor. This is a new approach to correlate surface properties with the activity. Although, catalysis is a process at the surface, the established descriptor models by Suntivich et al.[10] and Wei et al.[24] are bulk descriptors. As a result of these insights, we were also enabled to correlate the Faradaic efficiency of the here used

samples (Fig. 6.9b). The Faradaic efficiency increases with the increase in the manganese oxidation state, due to the more and more negligible manganese corrosion of the modified material. A new insight is provided by the additional plotting of the Faradaic efficiency, as this is concurrenting increasing. Thereby, it is possible to identify model catalysts, which only produces the preferred reaction product (here oxygen) and side reactions can be neglected. This provides a new insight in the mechanistic of the OER.

6.3. Conclusion

We investigated $Li_xMn_2O_4$ nano-sized particles with three different lithium contents, which catalyse the OER and the influence of their electronic structure on the catalytic activity. The lithium content and thereby the corresponding manganese oxidation state was independently determined and confirmed by XRD and XAS. These two complementary techniques to determine the average valence state were in a good agreement. However, we could also observe a core-shell behaviour of these particles, as reported for the initial particles (x=1). The oxidation by delithiation of this model catalyst causes a decrease in catalytic activity as expected from literature. However, it is remarkable that the catalytic behaviour of the modified material differs in comparison to the initial material, as the initial disk current decay could not anymore assigned to the manganese loss, but to a decay in the oxygen detection current. This for the initial material unknown behaviour causes an increase in the Faradaic efficiency as the manganese loss reaction is negligible. These results emphasise that it is insufficient to characterize catalytic activity only by the disk electrode current. Surprisingly, the trend for the catalytic activity over the manganese valence state is even more linear, when the activity is correlated with the valence state determine by surface sensitive TEY. This is remarkable, as the widely discussed descriptor models (e.g. valence state and e_g occupancy) rely on bulk descriptors, although, the water splitting reaction occurs at the surface of the catalyst.[10, 45, 147, 165, 166] For further mechanistic insights it is crucial to include the data of the detection electrode, as it provides important information about activity, corrosion and the resulting efficiency. Thereby, it enables new pathways in the mechanistic insights, as the Faradaic efficiency may help to select model catalysts which have no significant side reaction current contributions. Besides, the Faradaic efficiency contains the material property of this material — namely the manganese oxidation state of the catalyst, i.e., a mechanistic insight in the active site of the catalyst.

6.4. Experimental

6.4.1. Materials

As initial catalytic active material $LiMn_2O_4$ (99%) was purchased from Sigma-Aldrich, Acetylene carbon black was purchased from Alsa Aesar and was acid treated.[107] THF ($\geq$99.9% and stabilized) was bought from VWR. For the electrolyte 1 M sodium hydroxide Titripur (Merck) was purchased and diluted to needed concentration by ultrapure water (Milli-Q R$\geq$ 18.5 MΩ). The electrolyte was saturated with argon (5.0) from Air Liquide Alphagaz. For the synthesis ethylene carbonate/dimethyl carbonate (50:50) (EC/DMC) with 1 M $LiPF_6$ from Sigma-Aldrich was used as electrolyte. Lithium metal for Alfa Aeasar was used as counter electrode for the synthesis.[15, 16]

6.4.2. Electrochemical synthesis

The synthesis of the modified particles was performed in a battery cell (custom made Swagelok cell - Fig 3.4). Therefore, the pristine $LiMn_2O_4$ particles were mixed with carbon black in the same ratio as needed for the catalytic ink in the RRDE experiments and filled in a custom made Swagelok cell. A cotton separator is put on the powder before dropping a few drops of EC/DMC on it. The lithium metal counter electrode and a stainless steel current collector is put on top of the separator. A metal spring is the final inner part of the cell, which should press the components together and ensure an electrical contact. The cell is seal to the environment by a plunger. The assembly and disassembly of this cell was done in an argon filled glovebox (H_2O $\leq$0.5 ppm and O_2 $\leq$0.5 ppm).
For the (de)lithiation reaction a OFG500 module by OrigaFlex (OrigaLys SAS) is used. After an OCP, we realized a C/12 rate by applying a current (table A.7).

6.4.3. Sample Characterization

XRD characterization was performed by a Brucker D8 Discovery with monochromatized Cu-K_α radiation in a two theta range of 115°-85° (0.05° step size). The initial powder was glued on a microscope slide of glass, modified particles were drop casted on the microscope slide. XAS characterization was performed at KMC-2 and KMC-3 beamline in transmission mode and TEY at BESSY II synchrotron Berlin. For transmission mode, the material was homogenized by a mortar and applied on Kapton foil to realize a covered area of 1 cm^2. The used beam size was around 2 mm x 4 mm (hor. x vert.). To measure

in TEY mode, particles were applied on a carbon pad.

6.4.4. Catalytic performance

For evaluating the catalytic performance of the initial as well as the modified material a RRDE-setup was used. Therefore, a OrigaFlex (OrigaLys SAS) system containing of three OFG500 modules are connected and set to bipotentiostat configuration, realizing a three electrode setup. The experimental RRDE-setup contains of a RRDE-3 A rotator (ALS Japan Co Ltd.), a custom-made PTFE cylindrical cell, a Pt-counter electrode and a saturated calomel electrode (RE-2B, ALS Japan Co Ltd.), both radially arranged around the RRDE. the RRDE-electrode (ALS Japan Co Ltd.) is composed of a removable 4 mm in diameter glassy carbon electrode (area=0.126 cm^2) and a concentric platinum ring with 5 mm inner and 7 mm outer diameter - separated by a PTFE spacer. Both working electrodes were separately polished (Al_2O_3 polish) and cleaned afterwards in isopropanol to avoid cross contamination. After cleaning the working electrodes were assembled and 10 μL of catalytic ink containing of 12 mg powder (83% $Li_xMn_2O_4$ and 17% carbon black) and 2 mL THF were applied on the glassy carbon electrode.
For the experiment the electrolyte was saturated with argon gas. We used a rotation speed of 1600 rpm. The detection potential for the ring electrode was set to the previously determined potential of 0.4 V vs. RHE for oxygen detection and 1.2 V vs. RHE for manganese detection.[15] For iR correction we performed an EIS from 100 kHz to 1 Hz at OCP, after the CV.

7. Summary and Outlook

In this doctoral thesis, I gain mechanistic insights in catalysing the OER in alkaline solution, by using $Li_xMn_2O_4$ ($0 \leq x \leq 1$), a tuneable transition metal oxide spinel as a model catalyst for this multi-electron transfer reaction. Thereby, I aimed to unravel the influence of changes of its structural and electronic properties on the performance of catalytic water oxidation.

The initially first hypothesis, that the total disk current consists of the sum of at least two specific current contributions — namely OER activity and manganese loss, i.e., catalysis and corrosion — was addressed in chapter 4. Due to the RRDE-setup these reactions could be separately detected and identified.

- The first reaction was identified by setting the detection potential of the ring electrode to reduce the produced oxygen, i.e., the caused current is a qualitative indicator for the catalytic activity. This confirms the result of previous studies[46–49], that $LiMn_2O_4$ is capable to catalyse the OER. Additionally, it was possible to determine that the catalytic activity, i.e., the ring current is almost constant during all ten cycles, although the disk current is decreasing with the number of cycles. This usage of a detection electrode to characterize the catalytic activity is also possible in an acid environment, which was investigated for metal-organic ruthenium compound[167–169] and for iridium-based double perovskites as OER catalyst.[170]

- Besides, a second reaction due to the detection of manganese was identified. This current due to manganese detection decreases during the first three cycles and is negligible after five cycles. Meaning, the major loss happens in the first cycles and the catalyst reaches a steady state modus afterwards. The loss of manganese from a manganese oxide catalyst under OER conditions is expected as it was already reported by different techniques.[41, 103] The eminent advantage of the here used RRDE setup is that one is able temporal resolve when the manganese loss reaction occurs during the catalytic cycling. In contrast to Frydendal et al.[103], as they

only could determine a manganese loss of post mortem samples by ICP-MS. Later, an in-situ detection of dissolved manganese was achieved by Rabe et al.[171] using online Raman and in-situ ICP-MS.

The first hypothesis enables the calculation of the collection efficiency by a linear regression and therefore to summate these two detection currents corrected by this pre-factor, due to the high number of reproducible measurements. By this quantification procedure, it could be confirmed, that for the nano-sized particles, the total electrode current consists of only these two current contributions, i.e., there occurs no further reaction. The initial disk current decay during the first cycles is assigned to manganese loss, while the oxygen detection is unaffected by that.
In contrast to that, the micro-sized particles show that these two current contributions are not sufficient to describe the total electrode current. Which indicates that there is at least a third contribution to the total electrode current.

This preeminent third reaction could not be detected by the ring electrode. However, as the ratio of surface to volume is drastically decreasing with an increase in particle size, this side reaction is likely a manganese redox behaviour of the bulk.

To conclude on these findings, it is possible to describe the catalyst's behaviour and the origin of the total electrode current and thereby the selectivity of a catalyst. These results demonstrate the importance not only to characterize the catalytic activity by the current density of the catalyst's electrode as mostly done in literature [10, 96, 161, 165, 172], but also use an additional detection electrode to investigate the selectivity, i.e. the favoured product and side products to gain further understanding in the catalyst's behaviour. Additionally, these findings enable the study of Schönewald et al.[14] to critically questioning the usage of the e_g occupancy as a universal descriptor for OER activity.
Besides, this method to evaluate the behaviour of a catalyst by the different reaction current contributions could be used to clarify the open question, if a mixed manganese valence ($Mn^{3+/4+}$),[173] which corresponds to an e_g occupancy of 0.5 leads to the lowest overpotential in an alkaline electrolyte or a manganese valence of 3+ as predicted by previous studies.[10, 12, 24]

As $LiMn_2O_4$ is primarily know as an active cathode material in secondary batteries[56, 174, 175], manganese is not the only element which can be extracted of this compound. As discussed in the previous paragraph, the removal of tetrahedral coordinated manganese

has no impact on the OER. In contrast, a delithiation reaction, i.e., an extraction of lithium influences the catalytic activity, which is the subject of the second hypothesis and the following paragraph.

The second hypothesis, that an oxidation by delithiation of the volume of $Li_xMn_2O_4$ particles directly affects the catalytic activity, as indicated by a decrease in the oxygen current at a defined overpotential, was proven under two different experimental conditions.

In the first experiment nano-sized $LiMn_2O_4$ particles were in-situ delithiated by using different concentrated lithium hydroxide (aqueous) electrolytes, when being used as OER catalyst, as presented in chapter 5. In this electrolyte with a concentration below pH 14 defined redox peaks indicate a manganese oxidation during catalytic cycling. These peaks become more pronounced towards lower electrolyte concentration, i.e., the stability of the catalyst decreases in these lower concentrated electrolytes. This pH-dependent oxidation of the active material was confirmed by XAS of post-mortem electrodes and shifts the onset of the oxygen detection at the ring electrode to higher overpotential, which indicates a less active catalyst in low concentrated LiOH electrolytes and causes an unexpected non-zero Nernst slope (dE/dpH) of -40(4) mV/pH of the oxygen detection current.

Although, it was demonstrated by Li et al.[54, 55], that it is possible to delithiate $LiMn_2O_4$ in an aqueous (LiOH) battery cell, a controlled in-situ delithiation during being used as OER catalyst was not reported — as far as I know — which may enable further in-situ TEM and XAS studies.
In other studies, Köhler et al.[48] used $LiMn_2O_4$ in different concentrated sodium hydroxide electrolytes (pH 13.0, 13.2, 13.4 and 14), which is closely related to the lithium hydroxide, which was used in the work presented in chapter 5. However, Köhler et al.[48] did not observe redox peaks, which indicates a delithiation reaction nor a correlation between the used sodium hydroxide electrolyte concentration and the needed overpotential to drive the OER. This is remarkable, as the electrolytes are chemically related, thus the cations — lithium and sodium — are both alkali metals, and sodium is the next homologically larger one with respect to lithium.
This result highlights the importance of the environment, as this could directly affect the activity of the used catalyst even if the environmental differences are not evidently large. As demonstrated by Gao et al.[98], who investigated the influence of the alkali-metal ions of the electrolyte and correlated the OER activity of a MnO_x catalysts to the

containing cation of the use hydroxide electrolyte. They also observed this ambiguous character of side reactions, as they reported that the formation of passivation oxide of a MnO_x electrode (in LiOH, KOH and CsOH) did not affect the OER activity. However, the manganese corrosion in a NaOH electrolyte inactivated the catalyst.

Conclude on the points of the first and second hypothesis, side reactions are a critical aspect as they may change the catalyst itself and thereby its capability to catalyse the OER, e.g., by a delithiation process. On the other hand, as discussed in the previous section not every side reaction has an influence on the catalytic performance (e.g. manganese loss). This understanding of the stability of a catalyst is crucial for the development of new up-scaled OER catalysts.

In the second experiment, the material was ex-situ delithiated, i.e., particles were controlled synthesised in a purpose-built battery cell, by applying a defined positive current in a water- and oxygen-free organic battery electrolyte. Subsequently, the modified material was characterized, and the catalytic activity was evaluated by a RRDE setup in a sodium hydroxide electrolyte. In this context, the third hypothesis was addressed, that the oxidation by delithiation of $Li_{1-x}Mn_2O_4$ increases the Faradaic efficiency due to a negligible current contribution of the manganese detection. The results were presented in chapter 6.

As expected from literature[7–10, 13, 16, 165] the disk current is correlated with the electronic structure of manganese (oxidation state) and decreases in dependence with the lithium content of $Li_xMn_2O_4$. These findings agree with the second hypothesis. Surprisingly, the OER correlation with surface sensitive manganese valence provides a linear trend, in contrast to the bulk valence. Therefore, the manganese oxidation state of the surface has a more suitable descriptor behaviour. This approach to use the surface valence state is new. Although, catalysis is a process which occurs at the surface, in literature[10, 45, 147, 165, 166] often bulk descriptors are used.

Besides, the additional ring electrode to detect oxygen and manganese loss simultaneously, enables to determine the origin of the total disk current as demonstrated in chapter 4, which unravel a different catalytic behaviour for the delithiated samples. Here, the initial disk current decay during the first cycles could be assigned to the decay of the

oxygen detection current, while the manganese loss has only a small contribution. This is contradicting the behaviour of the initial material (x=1), as there the disk current decay is due to the loss of manganese during the first cycles, while the oxygen detection is almost constant. This difference causes an increase in the Faradaic efficiency from 75(2)% (x=1) to 96(5)% (x=0.25), although the total disk current decreases with an increase in the manganese oxidation state. This may lead to the assumption, that the delithiation process could remove the Mn_T^{2+} shell of the pristine particles (x=1), which was observed by Schönewald et al..[14] However, EELS experiments on the modified particles confirmed, that the core-shell structure remains unchanged throughout the delithiation process. In this thesis, the activity was correlated with the manganese valence, to gain further insights in the correlation of activity and material properties, EXAFS could provide beneficial structural information about the nominal manganese bonding environment (e.g., Mn-Mn and Mn-O bonding distances). This could be an important step for the use of descriptors, as it was shown by Schönewald et al.[14], that the e_g occupancy is not a universal descriptor for OER activity. This structural information may adjust and reconcile the model of descriptors and could be a systematically contribution to the studies of Sun et al.[12], as they provide a descriptor model based on the covalency competition of the M_T-O-M_O lattice motif.

Therefore, to conclude on the point of the third hypothesis, the determination of the Faradaic efficiency may help to identify model catalysts, which do not have a significant side reaction current contribution. This is important, as corrosion and catalysis are often concurring processes. Accordingly, the Faradaic efficiency can be used as a material property to identify these catalysts and provide a fundamental mechanistic insight in the OER, as no side reactions may interfere with the OER mechanism.

A. Appendix

A.1. Supporting information of chapter 3

This section covers the supporting information of chapter 3.

Ink casting

The solid components of the ink are washed up in tetrahydrofuran (THF) A.1 and has been put in a ultrasonic bath for 30 min. Two droplets (5 μL each) are applied on a clean and polished glassy carbon disk electrode by Single-Channel Pipette. By this, we are realizing a loading of 50 μg of active material.

Table A.1.: Ink composition

Quantity	**Chemical**
10 mg	$LiMn_2O_4$
2 mg	carbon black[1]
2 mL	THF

[1] acid treated [107]

A.2. Supporting information of chapter 4

This section covers the supporting information of chapter 4.

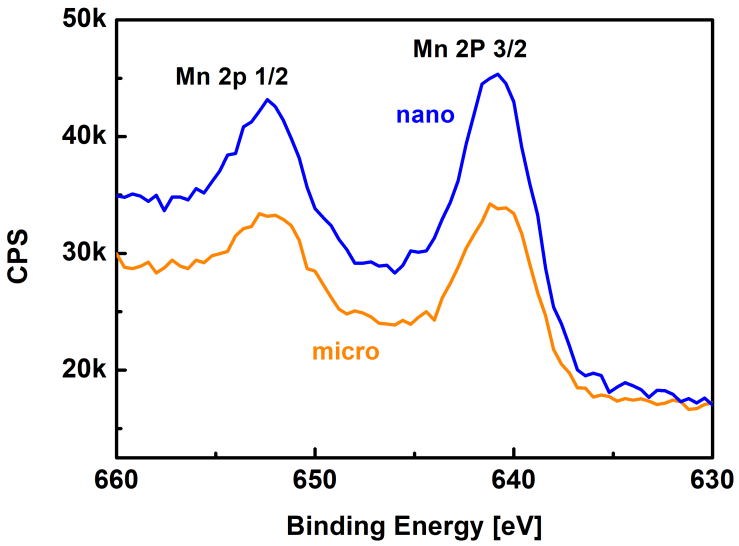

Figure A.1.: Mn2p XPS of nano and micro-sized particles. The spectra were recorded on a PHI 5000 VersaProbe II and energy calibrated to carbon. No background subtraction was performed.

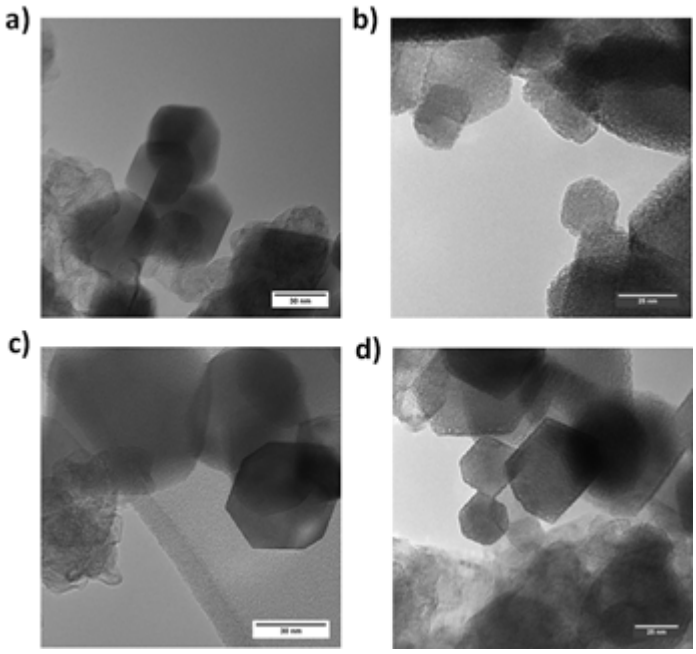

Figure A.2.: Additional TEM images of nano-sized particles (a,c) before cycling and (b,d) after cycling.

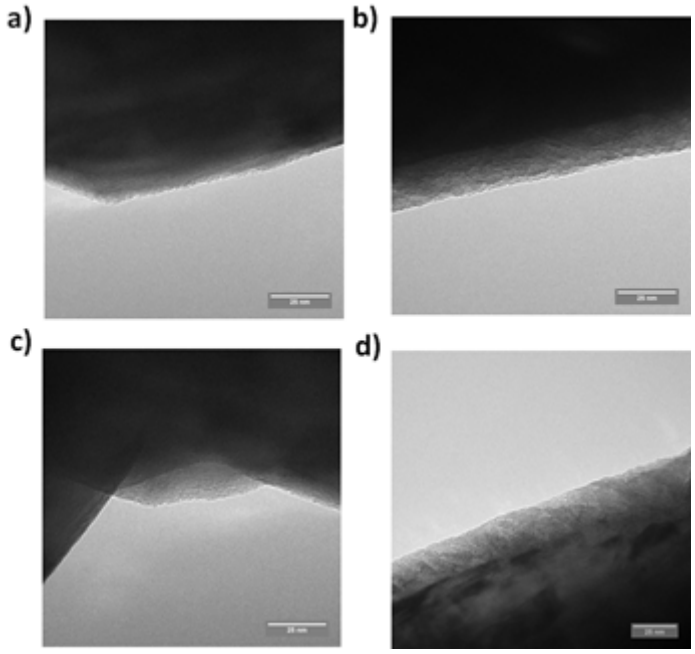

Figure A.3.: Additional TEM images of micro-sized particles, (a, c) before cycling and (b, d) after cycling.

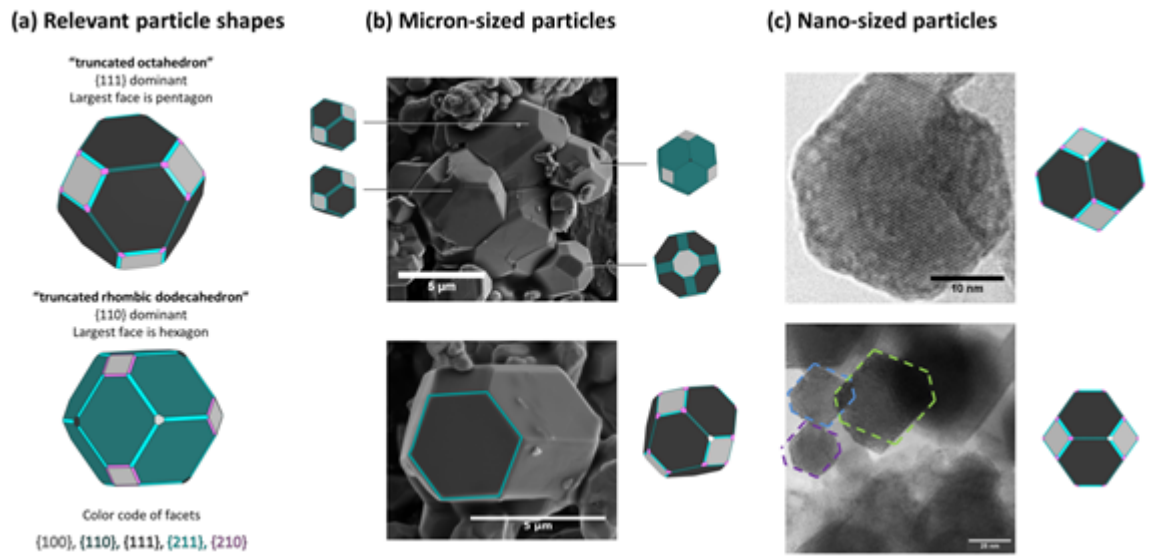

Figure A.4.: (a) Geometry of relevant particles shapes and assignment of facets (structure generated by Vesta[25]. (b) SEM images of micro particles to identify the dominant facets. (c) TEM images of nano-sized particles to identify the dominant facets.

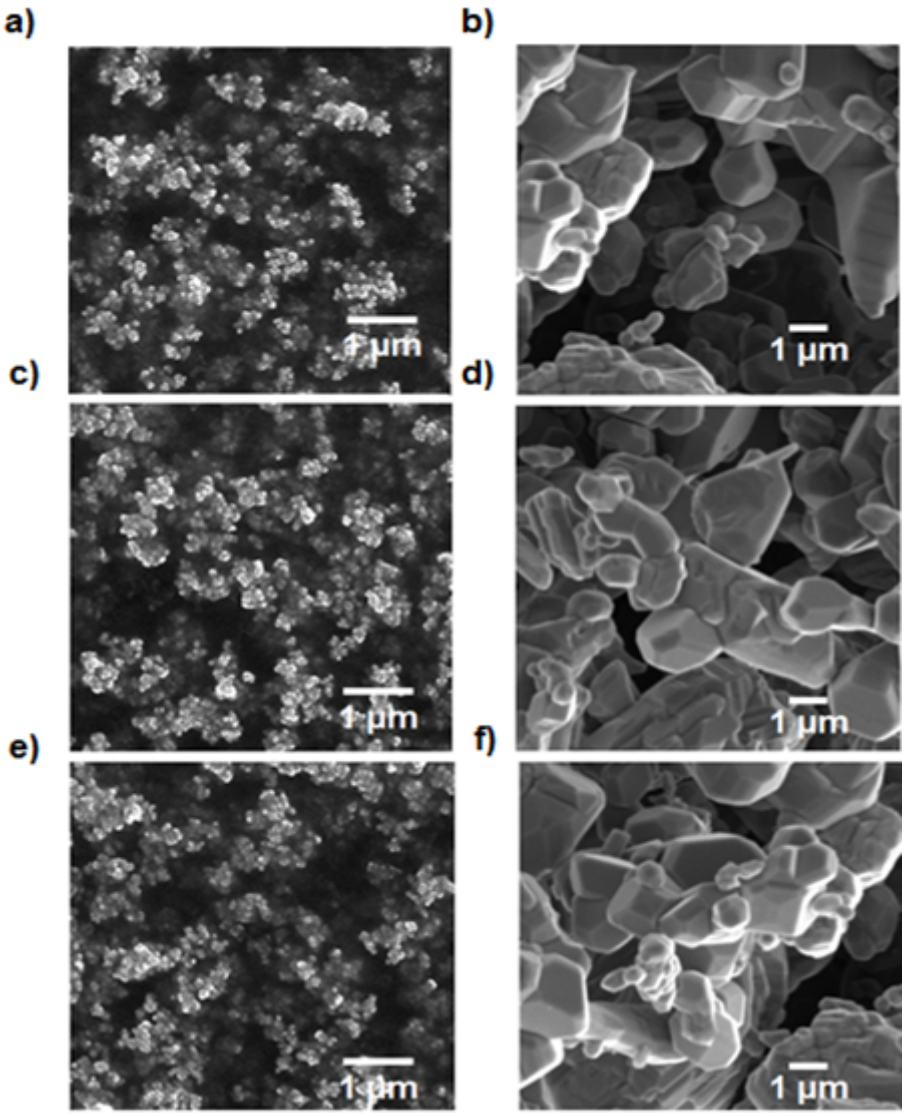

Figure A.5.: Additional SEM images of (a, c, e) the nano-sized particles and (b, d, f) micro-sized particles.

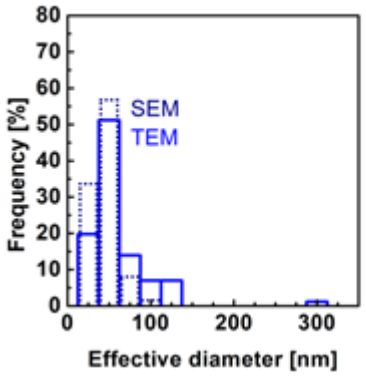

Figure A.6.: Particle distributions of nano-sized $LiMn_2O_4$ obtained by TEM (solid line) and SEM (dotted line; same data as Fig. 4.2c of the main text).

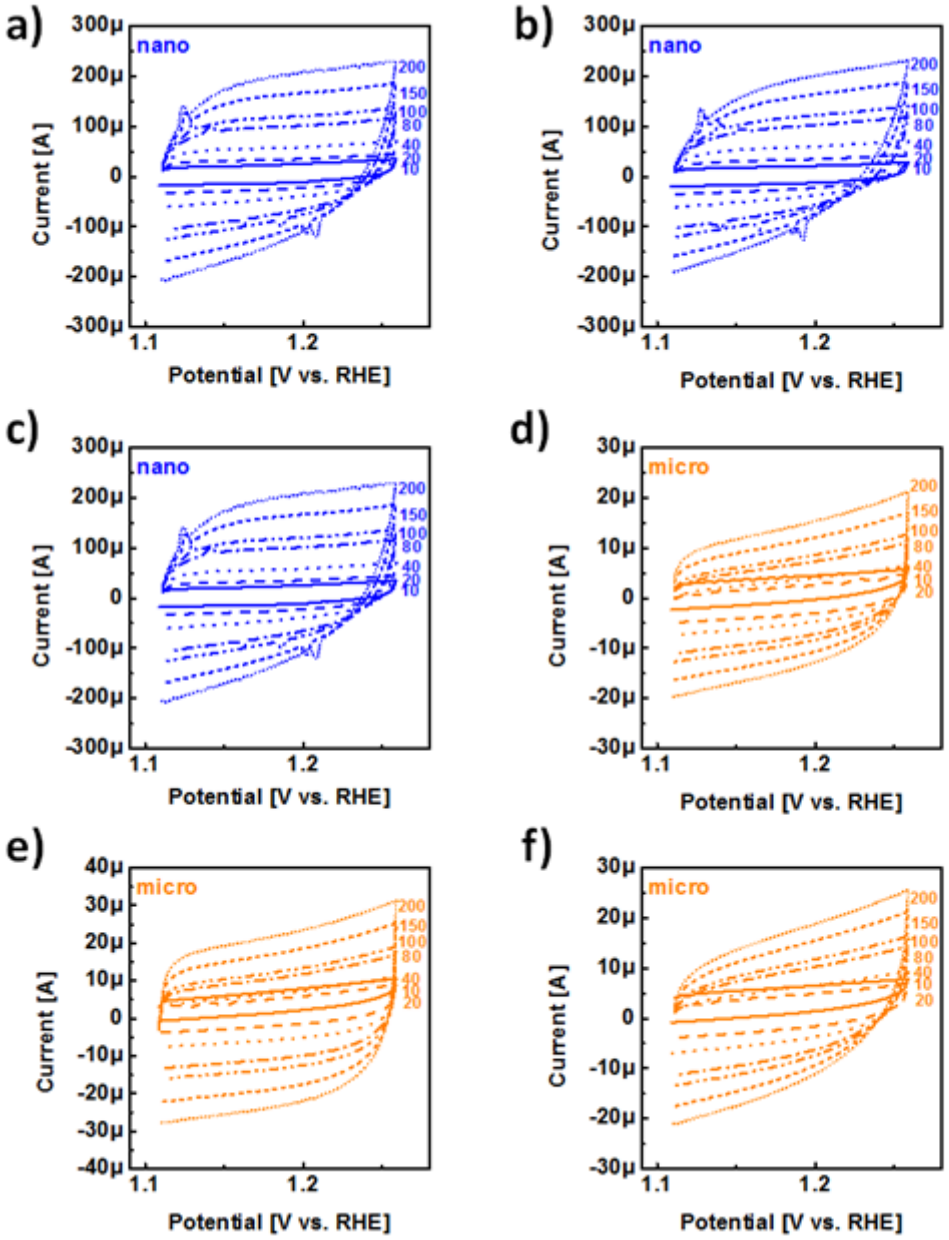

Figure A.7.: Representative CV between 1.1 and 1.25 V vs SCE to determine the double layer capacitance of (a-c) nano (d-f) micro particles

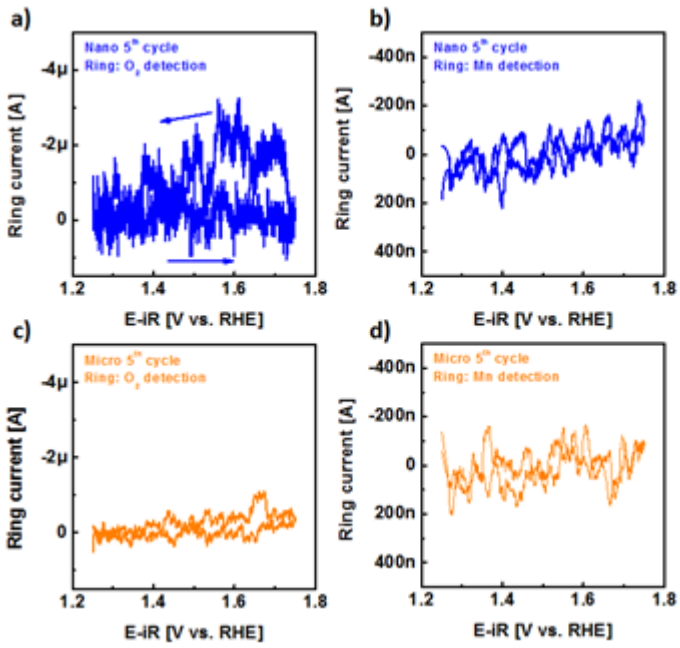

Figure A.8.: Investigation of cross talk between disk and ring electrode: (a) Oxygen detection at ring electrode at 0.4 V vs. RHE of a nano-particle casted disk electrode without any rotation. During the backward half cycle, oxygen was detected due to bubble formation which pushes the produced oxygen to the outer part of the electrode to the ring electrode. (b) Manganese detection at ring electrode at 1.2 V vs. RHE of a nano-particle casted disk electrode without any rotation. (c) Oxygen detection at ring electrode at 0.4 V vs. RHE of a micro-particle casted disk electrode without any rotation. (d) Manganese detection at ring electrode at 1.2 V vs. RHE of a micro-particle casted disk electrode without any rotation.

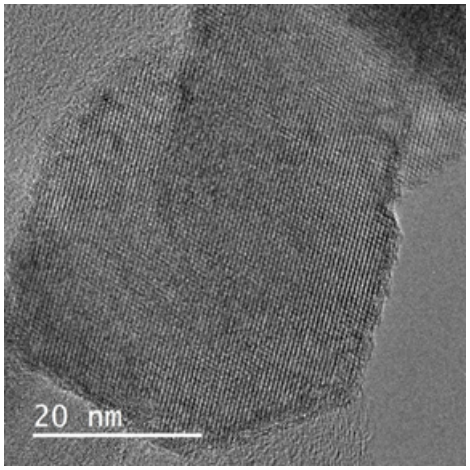

Figure A.9.: Additional HRTEM on post-cycle nano-sized powder in an image-corrected FEI Titan affirms that the material is not amorphized on the surface.

Table A.2.: R^2 of capacitance fit

Data points	**R^2 micro anodic / cathodic**	**R^2 nano anodic / cathodic**
1-7	0.95171/0.94644	0.98479/0.9441
1-6	0.92043/0.94714	0.99218/0.9599
1-5	0.85417/0.95083	0.9975/0.97333
1-4	0.64999/0.92461	0.99691/0.97986
2-7	0.99277/0.97365	0.98383/0.94986
2-6	0.99008/0.97645	0.99117/0.9659
2-5	0.9877/0.98282	0.99694/0.9795

Table A.3.: Various current densities of the $LiMn_2O_4$ powders at 1.68 V vs. RHE applied to disk during 5^{th} cycle.

Normalization	**disk**$_{mciro}$	**ring**$_{mciro}$	**disk**$_{nano}$	**ring**$_{nano}$
Disk area (A/cm^2_{disk})	0.60(5)m	8(2)μ	1.48(5)m	60(1)μ
Mass loading (A/g)	1.51(1)	0.06(1)	3.72(1)	0.15(4)
SEM area ($\mu A/cm^2_{SEM}$)	38.16(3)	0.1(4)	3.08(9)	0.13(3)
ECSA ($\mu A/cm^2_{ECSA}$)	205(2)	-2.0(7)	36(4)	-1.3(2)
Oxygen ($\mu A/cm^2_{ECSA}$)	n/a	40(14)	n/a	26(5)
Manganese ($\mu A/cm^2_{ECSA}$)	n/a	19(12)	n/a	8(7)

Table A.4.: Linear combination analysis of the current densities of the $LiMn_2O_4$ powders at 1.68 V vs. RHE

Coefficient	**Nano**	**Micro**
c_{O2}	-20.3(4)	-20.3(4)
c_{Mn}	-269(4)	-269(4)
R^2	0.9996	-

Note that the coefficients should be negative because the ring currents are negative but product currents (and the disk current) are positive. Fitting the coefficients of the micropowder yielded an unreasonable positive c_{O2} coefficient.

Table A.5.: Various current densities of the $LiMn_2O_4$ powders at 1.58 V vs. RHE applied to disk.

Catalyst	**SEM** ($\mathbf{mA/cm^2_{SEM}}$)	**ECSA** ($\mu\mathbf{A/cm^2_{ECSA}}$)	**Geometric** ($\mu\mathbf{A/cm^2_{geo}}$)	**Mass activity(A/g)**
Micro disk (this work)[1]	0.006(1)	34(3)	99(7)	0.25(2)
Micro O_2 yield (this work)[1]	40(3) nA/cm^2_{SEM}	4.0(4)	0.63(5)	0.002(4)
Nano disk (this work)[1]	0.0005(33)	5.8(4)	245(13)	0.62(4)
Nano O_2 yield (this work)[1]	3.1(6) nA/cm^2_{SEM}	1(5)	1.5(3)	0.004
Mn_2O_3 [104]	-	16(3)	160(30)	0.39(2)
MnO [104]	-	31(25)	220(18)	(0.53(9)
MnO_2 [104]	-	100(86)	440(35)	1.00(4)
Mn_3O_2 [104]	-	180(122)	720(49)	1.76(4)

We note that 1.58 V is very close to the onset of the OER on $LiMn_2O_4$ and thus produces large errors.

[1] 5^{th} cylce

A.3. Supporting information of chapter 5

This section covers the supporting information of chapter 5.

Electrochemical protocol

1. Ar purge at OCP 15 min
2. Disk EIS 100 kHz – 1 Hz; OCP
3. Ring CA: O2 Detection hold 0.4 V vs. RHE until Disk CV finishes OR Ring CA: Mn Detectioion hold 1.2 V vs. RHE until Disk CV finishes
4. Disk CV: OER (pH 12) hold 0.90 V for 5 min, then 0.9 – 1.79 vs. RHE; 10 mV/s; 10 cycles OR Disk CV: OER (all others) hold 1.25 V for 5 min, then 1.25 – 1.75 vs. RHE; 10 mV/s; 10 cycles
5. Disk OCP: Conditioning 300 sec
6. Disk EIS 100 kHz – 1 Hz, OCP

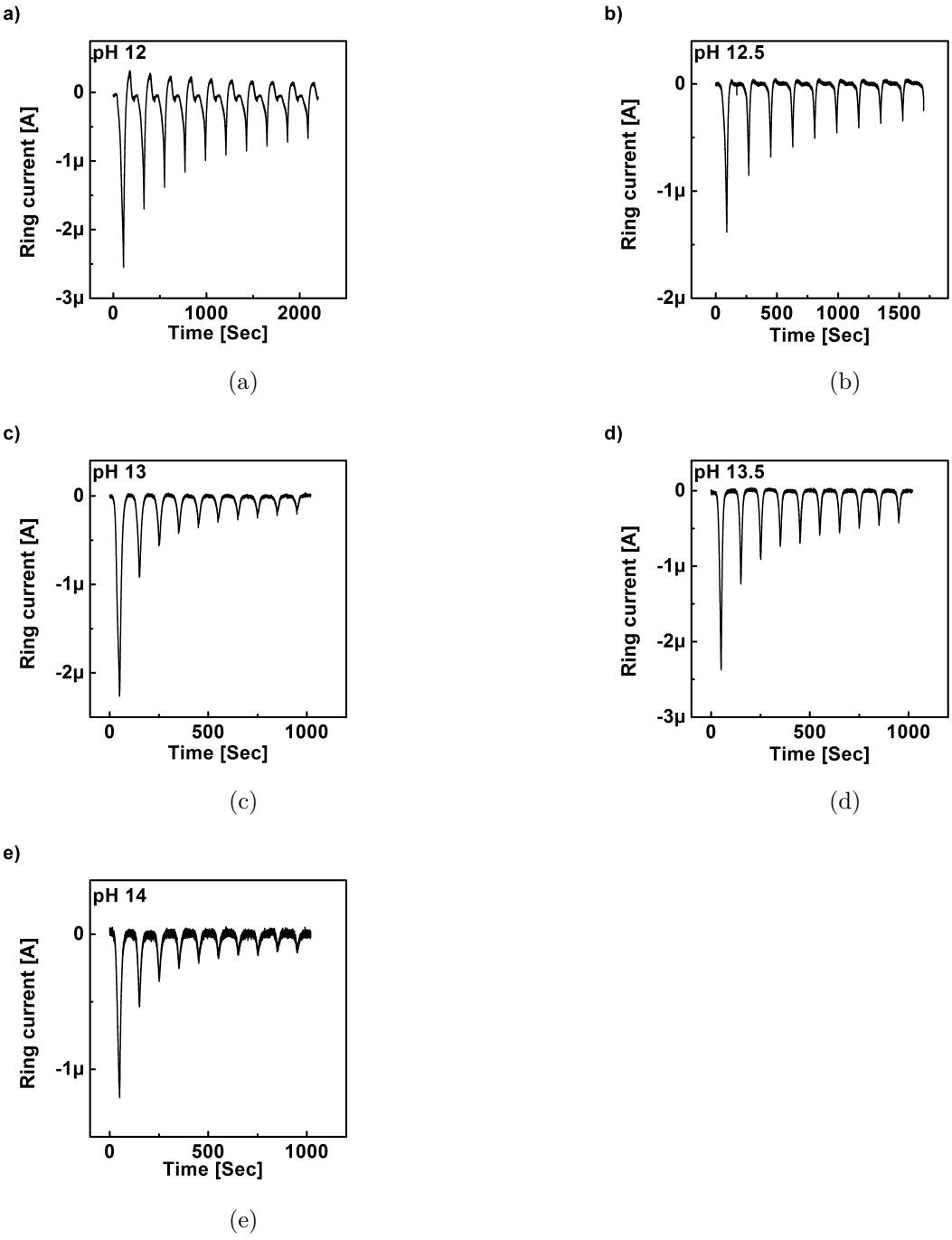

Figure A.10.: Representative ring currents to detect Mn-loss during cycling for all pH. The ring was set to 1.2 V vs. RHE and rotated at 1600 rpm.

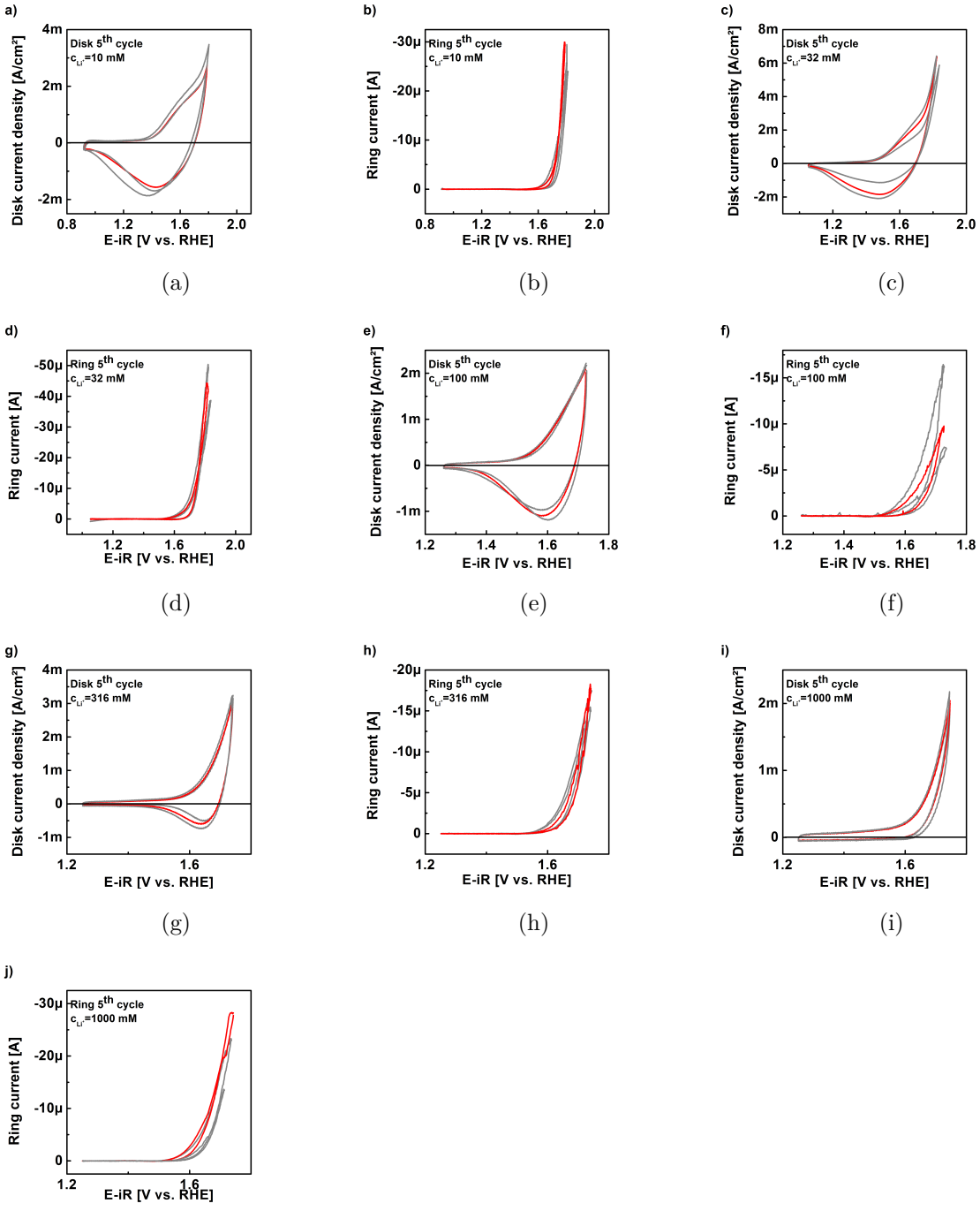

Figure A.11.: (a,c,e,g,i) CV at disk electrode and (b,d,f,h,j) corresponding ring at each lithium concentration (detection potential 0.4 V vs. RHE; 1600 rpm rotation). The representative CVs selected for the main text are shown in red.

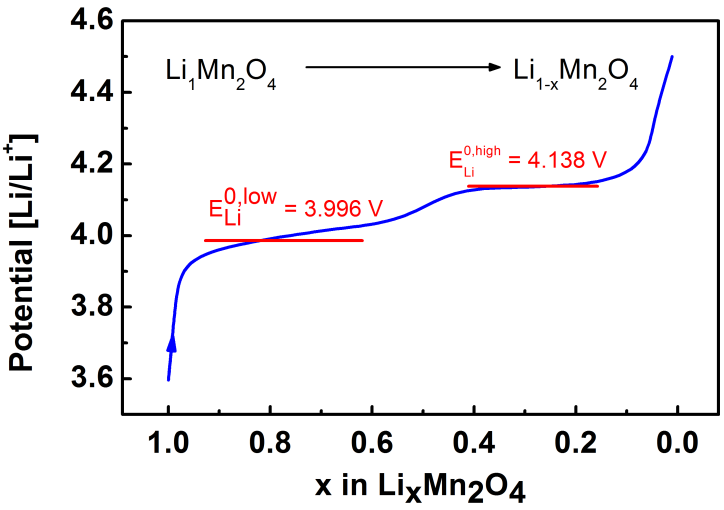

Figure A.12.: Delithiation of $Li_1Mn_2O_4$ towards $Li_0Mn_2O_4$ in 1 M $LiPF_6$ EC/DMC (50:50) electrolyte using C/12-rate. The cathode contained 83% active material and 17% carbon black. The anode and reference electrode were Li metal. Measurements were performed in a glovebox with < 1 ppm O_2 and water.

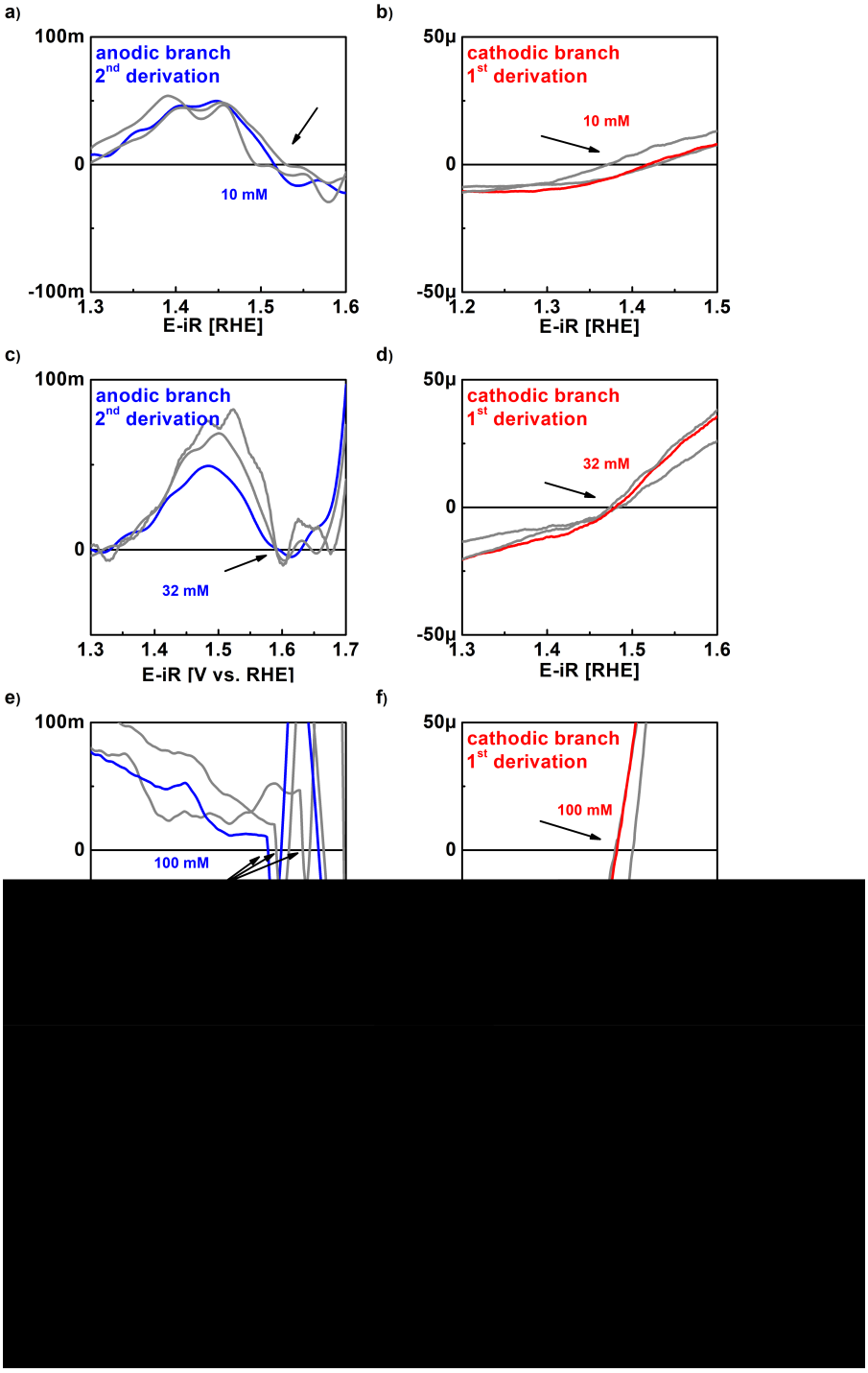

Figure A.13.: Second derivatives (a,c,e,g,i) of the anodic branch of the CV and (b,d,f,h,j) of the cathodic branch to determine the positions of shoulders and peaks in the CV.

Table A.6.: Key voltages (in V vs. RHE) of the E^{RHE}-pH diagram in Fig 5.3a

pH	**anodic**	**cathodic**	**midpoint**	**OER onset at -5 μA (ring)**
12	1.66(1)	1.40(3)	1.53(1)	1.73(1)
12.5	1.65(5)	1.479(5)	1.568(3)	1.729(3)
13	1.680(7)	1.58(1)	1.633(6)	1.69(1)
13.5	1.709(3)	1.638(5)	1.673(3)	1.689(5)
14	-	-	-	1.65(1)
Nernst slope	12(9) mV/pH[1]	200(20) mV/pH[1]	116(25) mV/pH[1]	-40(4) mV/pH[2]

[1]determined between and including pH 12 to pH 13
[2]determined between and including pH 12 to pH 14

A.4. Supporting information of chapter 6

This section covers the supporting information of chapter 6.

Table A.7.: Electrochemical parameters and chemical composition of $Li_xMn_2O_4$ synthesis in a purpose-built battery cell

Sample	**Amount of chemicals [mg]**		**Time [h]**	**Current [μA]**	**Cell potential after assembly [V]**
	$LiMn_2O_4$	carbon black			
x=0.25	97.1	20.0	12	898	3.58
x=0.51	96.3	19.8	12	594	3.57

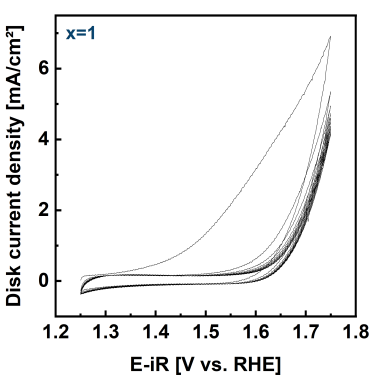

(a)

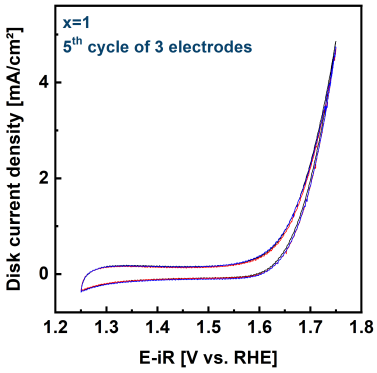

(b)

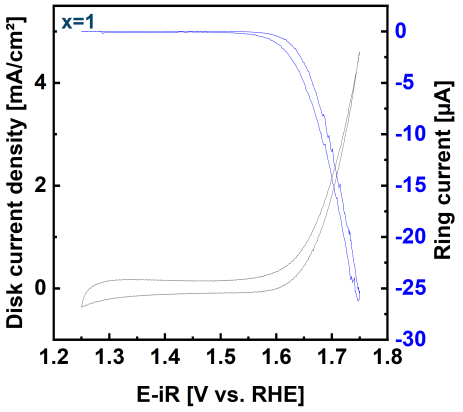

(c)

Figure A.14.: (a) 1^{st} to 10^{th} cycle of initial (x=1) $LiMn_2O_4$ (b) 5^{th} cycle of three electrodes to check the reproducibility (c) avg. 5^{th} cycle with corresponding oxygen detection current at the ring electrode

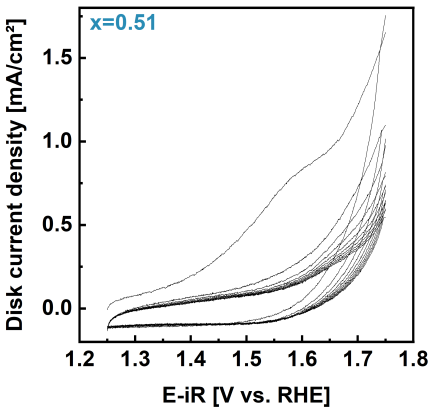

(a)

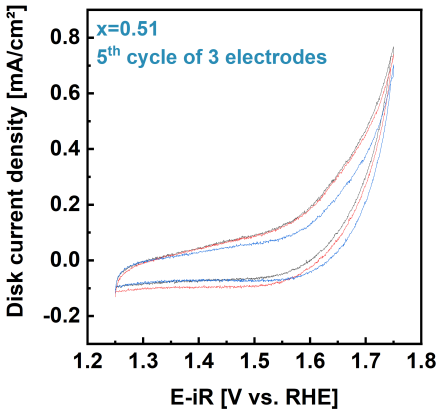

(b)

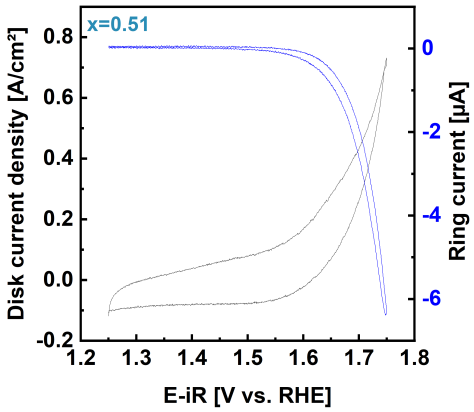

(c)

Figure A.15.: (a) 1^{st} to 10^{th} cycle of initial (x=0.51) $LiMn_2O_4$ (b) 5^{th} cycle of three electrodes to check the reproducibility (c) avg. 5^{th} cycle with corresponding oxygen detection current at the ring electrode

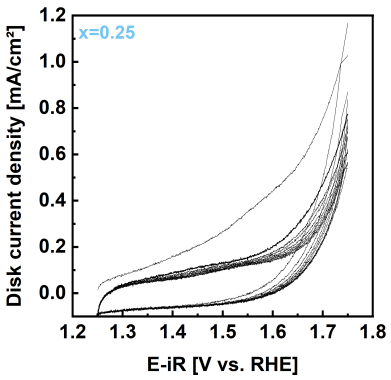

(a)

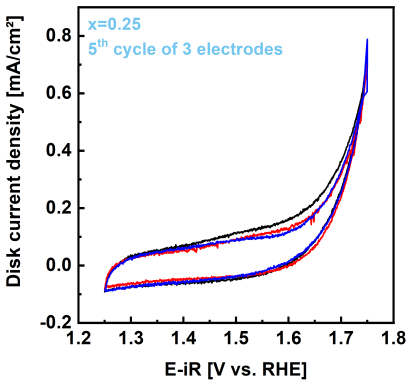

(b)

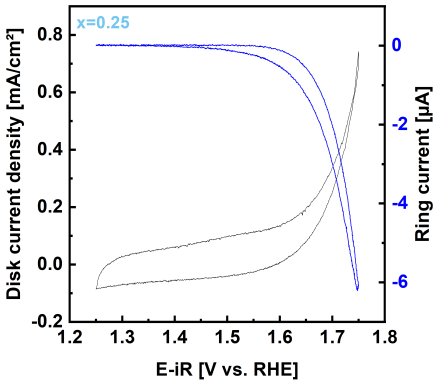

(c)

Figure A.16.: (a) 1^{st} to 10^{th} cycle of initial (x=0.25) $LiMn_2O_4$ (b) 5^{th} cycle of three electrodes to check the reproducibility (c) avg. 5^{th} cycle with corresponding oxygen detection current at the ring electrode

Table A.8.: Coefficients for the measured reaction currents at the ring electrode

Sample	$\mathbf{c}_{O2}$	$\mathbf{c}_{Mn}$
0.25	-25.2	-180
0.51	-23.7	-201
1	-20.3	-269

Bibliography

[1] Verne, Jules: The Mysterious Island. CreateSpace Independent Publishing Platform, 2015. – 596 S. – ISBN 978–1515248606

[2] Faunce, Thomas A. ; Lubitz, Wolfgang ; Rutherford, A. W. ; MacFarlane, Douglas ; Moore, Gary F. ; Yang, Peidong ; Nocera, Daniel G. ; Moore, Tom A. ; Gregory, Duncan H. ; Fukuzumi, Shunichi ; Yoon, Kyung B. ; Armstrong, Fraser A. ; Wasielewski, Michael R. ; Styring, Stenbjorn: Energy and environment policy case for a global project on artificial photosynthesis. In: Energy and Environmental Science 6 (2013), Nr. 3, S. 695–698. http://dx.doi.org/10.1039/c3ee00063j. – DOI 10.1039/c3ee00063j. – ISSN 17545692

[3] Armaroli, Nicola ; Balzani, Vincenzo: The future of energy supply: Challenges and opportunities. In: Angewandte Chemie - International Edition 46 (2007), Nr. 1-2, S. 52–66. http://dx.doi.org/10.1002/anie.200602373. – DOI 10.1002/anie.200602373. – ISBN 0512099456

[4] Smith, Rodney D. ; Prévot, Mathieu S. ; Fagan, Randal D. ; Trudel, Simon ; Berlinguette, Curtis P.: Water oxidation catalysis: Electrocatalytic response to metal stoichiometry in amorphous metal oxide films containing iron, cobalt, and nickel. In: Journal of the American Chemical Society 135 (2013), Nr. 31, S. 11580–11586. http://dx.doi.org/10.1021/ja403102j. – DOI 10.1021/ja403102j. – ISSN 00027863

[5] Han, Lei ; Dong, Shaojun ; Wang, Erkang: Transition-Metal (Co, Ni, and Fe)-Based Electrocatalysts for the Water Oxidation Reaction. In: Advanced Materials 28 (2016), Nr. 42, S. 9266–9291. http://dx.doi.org/10.1002/adma.201602270. – DOI 10.1002/adma.201602270. – ISSN 15214095

[6] Risch, Marcel ; Stoerzinger, Kelsey A. ; Han, Binghong ; Regier, Tom Z. ; Peak, Derek ; Sayed, Sayed Y. ; Wei, Chao ; Xu, Zhichuan ; Shao-Horn,

Yang: Redox Processes of Manganese Oxide in Catalyzing Oxygen Evolution and Reduction: An in Situ Soft X-ray Absorption Spectroscopy Study. In: Journal of Physical Chemistry C 121 (2017), Nr. 33, S. 17682–17692. http://dx.doi.org/10.1021/acs.jpcc.7b05592. – DOI 10.1021/acs.jpcc.7b05592. – ISSN 19327455

[7] Takashima, Toshihiro ; Hashimoto, Kazuhito ; Nakamura, Ryuhei: Mechanisms of pH-Dependent Activity for Water Oxidation to Molecular Oxygen by MnO 2 Electrocatalysts. In: Journal of the American Chemical Society 134 (2012), jan, Nr. 3, 1519–1527. http://dx.doi.org/10.1021/ja206511w. – DOI 10.1021/ja206511w. – ISSN 0002–7863

[8] Ooka, Hideshi ; Takashima, Toshihiro ; Yamaguchi, Akira ; Hayashi, Toru ; Nakamura, Ryuhei: Element strategy of oxygen evolution electrocatalysis based on in situ spectroelectrochemistry. In: Chemical Communications 53 (2017), Nr. 53, 7149–7161. http://dx.doi.org/10.1039/C7CC02204B. – DOI 10.1039/C7CC02204B. – ISSN 1359–7345

[9] Ramírez, Alejandra ; Hillebrand, Philipp ; Stellmach, Diana ; May, Matthias M. ; Bogdanoff, Peter ; Fiechter, Sebastian: Evaluation of MnOx, Mn2O3, and Mn 3O4 electrodeposited films for the oxygen evolution reaction of water. In: Journal of Physical Chemistry C 118 (2014), Nr. 26, S. 14073–14081. http://dx.doi.org/10.1021/jp500939d. – DOI 10.1021/jp500939d. – ISSN 19327455

[10] Suntivich, Jin ; May, Kevin J. ; Gasteiger, Hubert a. ; Goodenough, John B. ; Shao-Horn, Yang: A Perovskite Oxide Optimized for Oxygen Evolution Catalysis from Molecular Orbital Principles. In: Science 334 (2011), dec, Nr. 6061, 1383–1385. http://dx.doi.org/10.1126/science.1212858. – DOI 10.1126/science.1212858. – ISBN 10.1126/science.1212858

[11] Wei, Chao ; Rao, Reshma R. ; Peng, Jiayu ; Huang, Botao ; Stephens, Ifan E. ; Risch, Marcel ; Xu, Zhichuan J. ; Shao-Horn, Yang: Recommended Practices and Benchmark Activity for Hydrogen and Oxygen Electrocatalysis in Water Splitting and Fuel Cells. In: Advanced Materials 1806296 (2019), S. 1–24. http://dx.doi.org/10.1002/adma.201806296. – DOI 10.1002/adma.201806296. – ISSN 15214095

[12] Sun, Yuanmiao ; Liao, Hanbin ; Wang, Jiarui ; Chen, Bo ; Sun, Shengnan ; Ong, Samuel Jun H. ; Xi, Shibo ; Diao, Caozheng ; Du, Yonghua ; Wang, Jia-Ou ; Breese, Mark B. H. ; Li, Shuzhou ; Zhang, Hua ; Xu, Zhichuan J.: Covalency competition dominates the water oxidation structure–activity relationship on spinel oxides. In: Nature Catalysis (2020), jun. http://dx.doi.org/10.1038/s41929-020-0465-6. – DOI 10.1038/s41929–020–0465–6. – ISSN 2520–1158

[13] Shafirovich, V. Y. ; Khannanov, N. K. ; Shilov, A. E.: Inorganic models of photosystem II of plant photosynthesis. Catalytic and photocatalytic oxidation of water with participation of manganese compounds. In: Journal of Inorganic Biochemistry 15 (1981), Nr. 2, S. 113–129. http://dx.doi.org/10.1016/S0162-0134(00)80296-2. – DOI 10.1016/S0162–0134(00)80296–2. – ISSN 01620134

[14] Schönewald, Florian ; Eckhoff, Marco ; Baumung, Max ; Risch, Marcel ; Blöchl, Peter E. ; Behler, Jörg ; Volkert, Cynthia A.: A criticial view on eg occupancy as a descriptor for oxygen evolution catalytic activity in LiMn2O4 nanoparticles. (2020), jul. http://arxiv.org/abs/2007.04217

[15] Baumung, Max ; Schönewald, Florian ; Erichsen, Torben ; Volkert, Cynthia A. ; Risch, Marcel: Influence of particle size on the apparent electrocatalytic activity of LiMn 2 O 4 for oxygen evolution. In: Sustainable Energy & Fuels 3 (2019), Nr. 9, 2218–2226. http://dx.doi.org/10.1039/C8SE00551F. – DOI 10.1039/C8SE00551F. – ISSN 2398–4902

[16] Baumung, Max ; Kollenbach, Leon ; Xi, Lifei ; Risch, Marcel: Undesired Bulk Oxidation of LiMn 2 O 4 Increases Overpotential of Electrocatalytic Water Oxidation in Lithium Hydroxide Electrolytes. In: ChemPhysChem 20 (2019), nov, Nr. 22, 2981–2988. http://dx.doi.org/10.1002/cphc.201900601. – DOI 10.1002/cphc.201900601. – ISSN 1439–4235

[17] Hamann, Carl H. ; Vielstich, Wolf: Elektrochemie. 4. vollstä. Weinheim : Wiley-VCH Verlag GmbH & Co KGaA, 2005. – ISBN 978–3–527–21100–5

[18] Izgorodin, Alex ; Winther-Jensen, Orawan ; MacFarlane, Douglas R.: On the stability of water oxidation catalysts: Challenges and prospects. In: Australian Journal of Chemistry 65 (2012), Nr. 6, S. 638–642. http://dx.doi.org/10.1071/CH12024. – DOI 10.1071/CH12024. – ISSN 00049425

[19] Tan, Shu M. ; Pumera, Martin: Composition-Graded MoWS x Hybrids with Tailored Catalytic Activity by Bipolar Electrochemistry. In: ACS Applied Materials & Interfaces 9 (2017), dec, Nr. 48, 41955–41964. http://dx.doi.org/10.1021/acsami.7b09435. – DOI 10.1021/acsami.7b09435. – ISSN 1944–8244

[20] Lewis, Nathan S. ; Nocera, Daniel G.: Powering the planet: Chemical challenges in solar energy utilization. In: Proceedings of the National Academy of Sciences of the United States of America 103 (2006), Nr. 43, S. 15729–15735. http://dx.doi.org/10.1073/pnas.0603395103. – DOI 10.1073/pnas.0603395103. – ISSN 00278424

[21] Hong, Wesley T. ; Risch, Marcel ; Stoerzinger, Kelsey A. ; Grimaud, Alexis ; Suntivich, Jin ; Shao-Horn, Yang: Toward the rational design of non-precious transition metal oxides for oxygen electrocatalysis. In: Energy & Environmental Science 8 (2015), Nr. 5, 1404–1427. http://dx.doi.org/10.1039/C4EE03869J. – DOI 10.1039/C4EE03869J. – ISSN 1754–5692

[22] McCrory, Charles C. L. ; Jung, Suho ; Peters, Jonas C. ; Jaramillo, Thomas F.: Benchmarking Heterogeneous Electrocatalysts for the Oxygen Evolution Reaction. In: Journal of the American Chemical Society 135 (2013), nov, Nr. 45, 16977–16987. http://dx.doi.org/10.1021/ja407115p. – DOI 10.1021/ja407115p. – ISSN 0002–7863

[23] Dau, Holger ; Limberg, Christian ; Reier, Tobias ; Risch, Marcel ; Roggan, Stefan ; Strasser, Peter: The Mechanism of Water Oxidation: From Electrolysis via Homogeneous to Biological Catalysis. In: ChemCatChem 2 (2010), jun, Nr. 7, 724–761. http://dx.doi.org/10.1002/cctc.201000126. – DOI 10.1002/cctc.201000126. – ISSN 18673880

[24] Wei, Chao ; Feng, Zhenxing ; Scherer, Günther G. ; Barber, James ; Shao-Horn, Yang ; Xu, Zhichuan J.: Cations in Octahedral Sites: A Descriptor for Oxygen Electrocatalysis on Transition-Metal Spinels. In: Advanced Materials 1606800 (2017), jun, 1–8. http://dx.doi.org/10.1002/adma.201606800. – DOI 10.1002/adma.201606800. – ISSN 09359648

[25] Momma, Koichi ; Izumi, Fujio: VESTA 3 for three-dimensional visualization of crystal, volumetric and morphology data. In: Journal of Applied Crystallography 44

(2011), dec, Nr. 6, 1272–1276. http://dx.doi.org/10.1107/S0021889811038970. – DOI 10.1107/S0021889811038970. – ISSN 0021–8898

[26] Kobussen, A.G.C. ; Broers, G.H.J.: The oxygen evolution on La0.5Ba0.5CoO3. In: Journal of Electroanalytical Chemistry and Interfacial Electrochemistry 126 (1981), sep, Nr. 1-3, 221–240. http://dx.doi.org/10.1016/S0022-0728(81)80430-5. – DOI 10.1016/S0022–0728(81)80430–5. – ISSN 00220728

[27] Willems, H. ; Kobussen, A.G.C. ; De Wit, J.H.W. ; Broers, G.H.J.: The oxygen evolution reaction on cobalt. In: Journal of Electroanalytical Chemistry and Interfacial Electrochemistry 170 (1984), jul, Nr. 1-2, 227–242. http://dx.doi.org/10.1016/0022-0728(84)80046-7. – DOI 10.1016/0022–0728(84)80046–7. – ISSN 00220728

[28] Bockris, J. O.: Kinetics of Activation Controlled Consecutive Electrochemical Reactions: Anodic Evolution of Oxygen. In: The Journal of Chemical Physics 24 (1956), apr, Nr. 4, 817–827. http://dx.doi.org/10.1063/1.1742616. – DOI 10.1063/1.1742616. – ISSN 0021–9606

[29] Wohlfahrt-Mehrens, M. ; Heitbaum, J.: Oxygen evolution on Ru and RuO2 electrodes studied using isotope labelling and on-line mass spectrometry. In: Journal of Electroanalytical Chemistry and Interfacial Electrochemistry 237 (1987), nov, Nr. 2, 251–260. http://dx.doi.org/10.1016/0022-0728(87)85237-3. – DOI 10.1016/0022–0728(87)85237–3. – ISSN 00220728

[30] Antipin, Denis ; Risch, Marcel: Trends of epitaxial perovskite oxide films catalyzing the oxygen evolution reaction in alkaline media. In: Journal of Physics: Energy 2 (2020), may, Nr. 3, 032003. http://dx.doi.org/10.1088/2515-7655/ab812f. – DOI 10.1088/2515–7655/ab812f. – ISSN 2515–7655

[31] Risch, Marcel ; Ringleb, Franziska ; Kohlhoff, Mike ; Bogdanoff, Peter ; Chernev, Petko ; Zaharieva, Ivelina ; Dau, Holger: Water oxidation by amorphous cobalt-based oxides: In situ tracking of redox transitions and mode of catalysis. In: Energy and Environmental Science 8 (2015), Nr. 2, S. 661–674. http://dx.doi.org/10.1039/c4ee03004d. – DOI 10.1039/c4ee03004d. – ISSN 17545706

[32] Grimaud, Alexis ; May, Kevin J. ; Carlton, Christopher E. ; Lee, Yueh-Lin ; Risch, Marcel ; Hong, Wesley T. ; Zhou, Jigang ; Shao-Horn, Yang: Double

perovskites as a family of highly active catalysts for oxygen evolution in alkaline solution. In: Nature Communications 4 (2013), dec, Nr. 1, 2439. http://dx.doi.org/10.1038/ncomms3439. – DOI 10.1038/ncomms3439. – ISSN 2041–1723

[33] Greeley, Jeffrey: Theoretical Heterogeneous Catalysis: Scaling Relationships and Computational Catalyst Design. In: Annual Review of Chemical and Biomolecular Engineering 7 (2016), jun, Nr. 1, 605–635. http://dx.doi.org/10.1146/annurev-chembioeng-080615-034413. – DOI 10.1146/annurev–chembioeng–080615–034413. – ISSN 1947–5438

[34] Craig, Michael J. ; Coulter, Gabriel ; Dolan, Eoin ; Soriano-López, Joaquín ; Mates-Torres, Eric ; Schmitt, Wolfgang ; García-Melchor, Max: Universal scaling relations for the rational design of molecular water oxidation catalysts with near-zero overpotential. In: Nature Communications 10 (2019), dec, Nr. 1, 4993. http://dx.doi.org/10.1038/s41467-019-12994-w. – DOI 10.1038/s41467–019–12994–w. – ISSN 2041–1723

[35] Man, Isabela C. ; Su, Hai-Yan ; Calle-Vallejo, Federico ; Hansen, Heine A. ; Martínez, José I. ; Inoglu, Nilay G. ; Kitchin, John ; Jaramillo, Thomas F. ; Nørskov, Jens K. ; Rossmeisl, Jan: Universality in Oxygen Evolution Electrocatalysis on Oxide Surfaces. In: ChemCatChem 3 (2011), jul, Nr. 7, 1159–1165. http://dx.doi.org/10.1002/cctc.201000397. – DOI 10.1002/cctc.201000397. – ISSN 1867–3880

[36] Goodenough, John B.: Perspective on engineering transition-metal oxides. In: Chemistry of Materials 26 (2014), Nr. 1, S. 820–829. http://dx.doi.org/10.1021/cm402063u. – DOI 10.1021/cm402063u. – ISSN 08974756

[37] Karakaya, Irmak ; Karadas, Ferdi ; Ulgut, Burak ; Dag, Omer: Modification of Mesoporous LiMn2O4 and LiMn2xCoxO4 by SILAR Method for Highly Efficient Water Oxidation Electrocatalysis. In: Advanced Materials Technologies 2000353 (2020), jun, 2000353. http://dx.doi.org/10.1002/admt.202000353. – DOI 10.1002/admt.202000353. – ISSN 2365–709X

[38] Matsumoto, Y. ; Sato, E.: Electrocatalytic properties of transition metal oxides for oxygen evolution reaction. In: Materials Chemistry and Physics 14 (1986), may, Nr. 5, 397–426. http://dx.doi.org/10.1016/0254-0584(86)90045-3. – DOI 10.1016/0254–0584(86)90045–3. – ISSN 02540584

[39] Zhang, Biaobiao ; Sun, Licheng: Why nature chose the Mn 4 CaO 5 cluster as water-splitting catalyst in photosystem II: a new hypothesis for the mechanism of O–O bond formation. In: Dalton Transactions 47 (2018), Nr. 41, 14381–14387. http://dx.doi.org/10.1039/C8DT01931B. – DOI 10.1039/C8DT01931B. – ISSN 1477–9226

[40] Mierwaldt, Daniel ; Mildner, Stephanie ; Arrigo, Rosa ; Knop-Gericke, Axel ; Franke, Emanuel ; Blumenstein, Andreas ; Hoffmann, Jörg ; Jooss, Christian: In Situ XANES/XPS Investigation of Doped Manganese Perovskite Catalysts. In: Catalysts 4 (2014), Nr. 2, S. 129–145. http://dx.doi.org/10.3390/catal4020129. – DOI 10.3390/catal4020129

[41] Mierwaldt, Daniel ; Roddatis, Vladimir ; Risch, Marcel ; Scholz, Julius ; Geppert, Janis ; Abrishami, Majid E. ; Jooss, Christian: Environmental TEM Investigation of Electrochemical Stability of Perovskite and Ruddlesden-Popper Type Manganite Oxygen Evolution Catalysts. In: Advanced Sustainable Systems 1 (2017), dec, Nr. 1700109, 1–10. http://dx.doi.org/10.1002/adsu.201700109. – DOI 10.1002/adsu.201700109. – ISSN 23667486

[42] Scholz, Julius ; Risch, Marcel ; Stoerzinger, Kelsey A. ; Wartner, Garlef ; Shao-Horn, Yang ; Jooss, Christian: Rotating Ring–Disk Electrode Study of Oxygen Evolution at a Perovskite Surface: Correlating Activity to Manganese Concentration. In: The Journal of Physical Chemistry C 120 (2016), dec, Nr. 49, 27746–27756. http://dx.doi.org/10.1021/acs.jpcc.6b07654. – DOI 10.1021/acs.jpcc.6b07654. – ISSN 1932–7447

[43] Jooss, Ch ; Wu, L. ; Beetz, T. ; Klie, R. F. ; Beleggia, M. ; Schofield, M. A. ; Schramm, S. ; Hoffmann, J. ; Zhu, Y.: Polaron melting and ordering as key mechanisms for colossal resistance effects in manganites. In: Proceedings of the National Academy of Sciences 104 (2007), aug, Nr. 34, 13597–13602. http://dx.doi.org/10.1073/pnas.0702748104. – DOI 10.1073/pnas.0702748104. – ISSN 0027–8424

[44] Wei, Chao ; Rao, Reshma R. ; Peng, Jiayu ; Huang, Botao ; Stephens, Ifan E. ; Risch, Marcel ; Xu, Zhichuan J. ; Shao-Horn, Yang: Recommended Practices and Benchmark Activity for Hydrogen and Oxygen Electrocatalysis in Water Splitting and Fuel Cells. In: Advanced Materials (2019).

http://dx.doi.org/10.1002/adma.201806296. – DOI 10.1002/adma.201806296. – ISSN 15214095

[45] Cady, Clyde W. ; Gardner, Graeme ; Maron, Zachary O. ; Retuerto, Maria ; Go, Yong B. ; Segan, Shreeda ; Greenblatt, Martha ; Dismukes, G. C.: Tuning the Electrocatalytic Water Oxidation Properties of AB 2 O 4 Spinel Nanocrystals: A (Li, Mg, Zn) and B (Mn, Co) Site Variants of LiMn 2 O 4. In: ACS Catalysis 5 (2015), jun, Nr. 6, 3403–3410. http://dx.doi.org/10.1021/acscatal.5b00265. – DOI 10.1021/acscatal.5b00265. – ISSN 2155–5435

[46] Maitra, Urmimala ; Naidu, B. S. ; Govindaraj, A. ; Rao, C. N. R.: Importance of trivalency and the eg1 configuration in the photocatalytic oxidation of water by Mn and Co oxides. In: Proceedings of the National Academy of Sciences 110 (2013), jul, Nr. 29, 11704–11707. http://dx.doi.org/10.1073/pnas.1310703110. – DOI 10.1073/pnas.1310703110. – ISSN 0027–8424

[47] Robinson, David M. ; Go, Yong B. ; Greenblatt, Martha ; Dismukes, G. C.: Water Oxidation by λ-MnO2: Catalysis by the Cubical Mn4O4 Subcluster Obtained by Delithiation of Spinel LiMn2O4. In: Journal of the American Chemical Society 132 (2010), Nr. 33, S. 11467–11469. http://dx.doi.org/10.1021/ja1055615. – DOI 10.1021/ja1055615. – ISSN 00027863

[48] Köhler, Lennart ; Ebrahimizadeh Abrishami, Majid ; Roddatis, Vladimir ; Geppert, Janis ; Risch, Marcel: Mechanistic Parameters of Electrocatalytic Water Oxidation on LiMn 2 O 4 in Comparison to Natural Photosynthesis. In: ChemSusChem 10 (2017), nov, Nr. 22, 4479–4490. http://dx.doi.org/10.1002/cssc.201701582. – DOI 10.1002/cssc.201701582. – ISSN 18645631

[49] Robinson, David M. ; Go, Yong B. ; Mui, Michelle ; Gardner, Graeme ; Zhang, Zhijuan ; Mastrogiovanni, Daniel ; Garfunkel, Eric ; Li, Jing ; Greenblatt, Martha ; Dismukes, G. C.: Photochemical Water Oxidation by Crystalline Polymorphs of Manganese Oxides: Structural Requirements for Catalysis. In: Journal of the American Chemical Society 135 (2013), mar, Nr. 9, 3494–3501. http://dx.doi.org/10.1021/ja310286h. – DOI 10.1021/ja310286h. – ISSN 0002–7863

[50] Hunter, James C.: Preparation of a new crystal form of manganese dioxide: λ-MnO2. In: Journal of Solid State Chemistry 39 (1981), sep, Nr. 2, 142–

147. http://dx.doi.org/10.1016/0022-4596(81)90323-6. – DOI 10.1016/0022–4596(81)90323–6. – ISSN 00224596

[51] Thackeray, M.M. ; Johnson, P.J. ; Picciotto, L.A. de ; Bruce, P.G. ; Goodenough, J.B.: Electrochemical extraction of lithium from LiMn2O4. In: Materials Research Bulletin 19 (1984), feb, Nr. 2, 179–187. http://dx.doi.org/10.1016/0025-5408(84)90088-6. – DOI 10.1016/0025–5408(84)90088–6. – ISSN 00255408

[52] Thackeray, Michael M.: Manganese oxides for lithium batteries. In: Progress in Solid State Chemistry 25 (1997), jan, Nr. 1-2, 1–71. http://dx.doi.org/10.1016/S0079-6786(97)81003-5. – DOI 10.1016/S0079–6786(97)81003–5. – ISSN 00796786

[53] Kim, Do K. ; Muralidharan, P. ; Lee, Hyun-Wook ; Ruffo, Riccardo ; Yang, Yuan ; Chan, Candace K. ; Peng, Hailin ; Huggins, Robert A. ; Cui, Yi: Spinel LiMn 2 O 4 Nanorods as Lithium Ion Battery Cathodes. In: Nano Letters 8 (2008), nov, Nr. 11, 3948–3952. http://dx.doi.org/10.1021/nl8024328. – DOI 10.1021/nl8024328. – ISSN 1530–6984

[54] Li, W. ; McKinnon, W. R. ; Dahn, J. R.: Lithium Intercalation from Aqueous Solutions. In: Journal of The Electrochemical Society 141 (1994), Nr. 9, 2310–2316. http://dx.doi.org/10.1557/PROC-369-69. – DOI 10.1557/PROC–369–69. – ISSN 1946–4274

[55] Li, W. ; Dahn, J. R.: Lithium-Ion Cells with Aqueous Electrolytes. In: Journal of The Electrochemical Society 142 (1995), Nr. 6, 1742–1746. http://dx.doi.org/10.1149/1.2044187. – DOI 10.1149/1.2044187. – ISSN 00134651

[56] Thackeray, M. M. ; Croy, J. R. ; Lee, Eungje ; Gutierrez, A. ; He, Meinan ; Park, Joong S. ; Yonemoto, B. T. ; Long, B. R. ; Blauwkamp, J. D. ; Johnson, C. S. ; Shin, Youngho ; David, W. I.: The quest for manganese-rich electrodes for lithium batteries: Strategic design and electrochemical behavior. In: Sustainable Energy and Fuels 2 (2018), Nr. 7, S. 1375–1397. http://dx.doi.org/10.1039/c8se00157j. – DOI 10.1039/c8se00157j. – ISSN 23984902

[57] Thackeray, Michael M.: Structural Fatigue in Spinel Electrodes in High Voltage (4 V) Li/Li[sub x]Mn[sub 2]O[sub 4] Cells. In: Electrochemical and Solid-State Letters 1 (1999), Nr. 1, S. 7. http://dx.doi.org/10.1149/1.1390617. – DOI 10.1149/1.1390617. – ISSN 10990062

[58] Croguennec, Laurence ; Deniard, Philippe ; Brec, Raymond ; Lecerf, André: Nature of the stacking faults in orthorhombic LiMnO2. In: Journal of Materials Chemistry 7 (1997), Nr. 3, 511–516. http://dx.doi.org/10.1039/a604947h. – DOI 10.1039/a604947h. – ISSN 09599428

[59] Julien, Christian ; Mauger, Alain ; Zaghib, Karim ; Groult, Henri: Comparative Issues of Cathode Materials for Li-Ion Batteries. In: Inorganics 2 (2014), mar, Nr. 1, 132–154. http://dx.doi.org/10.3390/inorganics2010132. – DOI 10.3390/inorganics2010132. – ISSN 2304–6740

[60] Eckhoff, Marco ; Schönewald, Florian ; Risch, Marcel ; Volkert, Cynthia A. ; Blöchl, Peter E. ; Behler, Jörg: Closing the Gap between Theory and Experiment for Lithium Manganese Oxide Spinels Using a High-Dimensional Neural Network Potential. (2020), jul, 1–20. http://arxiv.org/abs/2007.00327

[61] Gao, Jian ; Shi, Si Q. ; Li, Hong: Brief overview of electrochemical potential in lithium ion batteries. In: Chinese Physics B 25 (2015), Nr. 1. http://dx.doi.org/10.1088/1674-1056/25/1/018210. – DOI 10.1088/1674–1056/25/1/018210. – ISSN 20583834

[62] Helmholtz, Hermann: Studien über electrische Grenzschichten. In: Annalen der Physik und Chemie 243 (1879), Nr. 7, 337–382. http://dx.doi.org/10.1002/andp.18792430702. – DOI 10.1002/andp.18792430702. – ISSN 00033804

[63] Gouy, M.: Sur la constitution de la charge électrique à la surface d'un électrolyte. In: Journal de Physique Théorique et Appliquée 9 (1910), Nr. 1, 457–468. http://dx.doi.org/10.1051/jphystap:019100090045700. – DOI 10.1051/jphystap:019100090045700. – ISSN 0368–3893

[64] Chapman, David L.: LI. A contribution to the theory of electrocapillarity . In: The London, Edinburgh, and Dublin Philosophical Magazine and Journal of Science 25 (1913), Nr. 148, S. 475–481. http://dx.doi.org/10.1080/14786440408634187. – DOI 10.1080/14786440408634187. – ISSN 1941–5982

[65] Stern, Otto: ZUR THEORIE DER ELEKTROLYTISCHEN DOPPELSCHICHT. In: Zeitschrift für Elektrochemie und angewandte physikalische Chemie 30 (1924), 508–516. http://dx.doi.org/https://onlinelibrary.wiley.com/doi/epdf/10.1002/bbpc.192400182. – DOI https://onlinelibrary.wiley.com/doi/epdf/10.1002/bbpc.192400182

[66] Connor, Paula ; Schuch, Jona ; Kaiser, Bernhard ; Jaegermann, Wolfram: The Determination of Electrochemical Active Surface Area and Specific Capacity Revisited for the System MnOx as an Oxygen Evolution Catalyst. In: Zeitschrift für Physikalische Chemie (2020), jan. http://dx.doi.org/10.1515/zpch-2019-1514. – DOI 10.1515/zpch–2019–1514. – ISSN 2196–7156

[67] Watzele, Sebastian ; Bandarenka, Aliaksandr S.: Quick Determination of Electroactive Surface Area of Some Oxide Electrode Materials. In: Electroanalysis 28 (2016), oct, Nr. 10, 2394–2399. http://dx.doi.org/10.1002/elan.201600178. – DOI 10.1002/elan.201600178. – ISSN 10400397

[68] Watzele, Sebastian ; Hauenstein, Pascal ; Liang, Yunchang ; Xue, Song ; Fichtner, Johannes ; Garlyyev, Batyr ; Scieszka, Daniel ; Claudel, Fabien ; Maillard, Frédéric ; Bandarenka, Aliaksandr S.: Determination of Electroactive Surface Area of Ni-, Co-, Fe-, and Ir-Based Oxide Electrocatalysts. In: ACS Catalysis (2019), sep, 9222–9230. http://dx.doi.org/10.1021/acscatal.9b02006. – DOI 10.1021/acscatal.9b02006. – ISSN 2155–5435

[69] Binninger, T. ; Fabbri, E. ; Kötz, R. ; Schmidt, T. J.: Determination of the Electrochemically Active Surface Area of Metal-Oxide Supported Platinum Catalyst. In: Journal of The Electrochemical Society 161 (2014), Nr. 3, S. H121–H128. http://dx.doi.org/10.1149/2.055403jes. – DOI 10.1149/2.055403jes. – ISSN 0013–4651

[70] Morales, Dulce M. ; Risch, Marcel: Seven steps to reliable cyclic voltammetry measurements for the determination of double layer capacitance. (2020), dec, Nr. December. http://arxiv.org/abs/2012.00801

[71] Atkins, Peter W. ; De Paula, Julio: Physikalische Chemie. 4., vollst. Weinheim : Wiley-VCH Verlag GmbH & Co KGaA, 2007. – ISBN 978–3–527–31828–5

[72] Bard, Allen J. ; Faulkner, Larry R.: Electrochemical Methods: Fundamentals and Applicati Second Edi. John Wiley & Sons, Inc, 2001. – ISBN 978–0–471–04372–0

[73] Fletcher, Stephen: Tafel slopes from first principles. In: Journal of Solid State Electrochemistry 13 (2009), Nr. 4, S. 537–549. http://dx.doi.org/10.1007/s10008-008-0670-8. – DOI 10.1007/s10008–008–0670–8. – ISBN 1000800806

[74] Fang, Ya-Hui ; Liu, Zhi-Pan: Tafel Kinetics of Electrocatalytic Reactions: From Experiment to First-Principles. In: ACS Catalysis 4 (2014), dec, Nr. 12, 4364–4376. http://dx.doi.org/10.1021/cs501312v. – DOI 10.1021/cs501312v. – ISSN 2155–5435

[75] Gerken, James B. ; McAlpin, J. G. ; Chen, Jamie Y. C. ; Rigsby, Matthew L. ; Casey, William H. ; Britt, R. D. ; Stahl, Shannon S.: Electrochemical Water Oxidation with Cobalt-Based Electrocatalysts from pH 0–14: The Thermodynamic Basis for Catalyst Structure, Stability, and Activity. In: Journal of the American Chemical Society 133 (2011), sep, Nr. 36, 14431–14442. http://dx.doi.org/10.1021/ja205647m. – DOI 10.1021/ja205647m. – ISSN 0002–7863

[76] Dalton, Frank: ECS Classics: Historical Origins of the Rotating Ring-Disk Electrode. In: Interface magazine 25 (2016), jan, Nr. 3, 50–59. http://dx.doi.org/10.1149/2.F03163if. – DOI 10.1149/2.F03163if. – ISSN 1064–8208

[77] Bruckenstein, Stanley ; Nagai, Toyoshi: The Rotated, Mercury-Coated Platinum Electrode. In: Analytical Chemistry 33 (1961), aug, Nr. 9, 1201–1209. http://dx.doi.org/10.1021/ac60177a023. – DOI 10.1021/ac60177a023. – ISSN 0003–2700

[78] Frumkin, A. ; Nekrasov, L. ; Levich, B. ; Ivanov, Ju.: Die anwendung der rotierenden scheibenelektrode mit einem ringe zur untersuchung von zwischenprodukten elektrochemischer reaktionen. In: Journal of Electroanalytical Chemistry (1959) 1 (1959), aug, Nr. 1, 84–90. http://dx.doi.org/10.1016/0022-0728(59)80012-7. – DOI 10.1016/0022–0728(59)80012–7. – ISSN 03681874

[79] Elgrishi, Noémie ; Rountree, Kelley J. ; McCarthy, Brian D. ; Rountree, Eric S. ; Eisenhart, Thomas T. ; Dempsey, Jillian L.: A Practical Beginner's Guide to Cyclic Voltammetry. In: Journal of Chemical Education 95 (2018), feb, Nr. 2, 197–206. http://dx.doi.org/10.1021/acs.jchemed.7b00361. – DOI 10.1021/acs.jchemed.7b00361. – ISSN 0021–9584

[80] Lim, Jongwoo ; Li, Yiyang ; Alsem, Daan H. ; So, Hongyun ; Lee, Sang C. ; Bai, Peng ; Cogswell, Daniel A. ; Liu, Xuzhao ; Jin, Norman ; Yu, Young S. ; Salmon, Norman J. ; Shapiro, David A. ; Bazant, Martin Z. ; Tyliszczak, Tolek ; Chueh, William C.: Origin and hysteresis of lithium compositional spatiodynamics within battery primary particles. In: Science 353 (2016), Nr. 6299,

S. 566–571. http://dx.doi.org/10.1126/science.aaf4914. – DOI 10.1126/science.aaf4914. – ISSN 10959203

[81] Eckhoff, Marco ; Blöchl, Peter E. ; Behler, Jörg: A Hybrid Density Functional Theory Benchmark Study on Lithium Manganese Oxides. (2020), 1–18. http://arxiv.org/abs/2001.10975

[82] Newville, M.: Fundamentals of XAFS. In: Reviews in Mineralogy and Geochemistry 78 (2014), jan, Nr. 1, 33–74. http://dx.doi.org/10.2138/rmg.2014.78.2. – DOI 10.2138/rmg.2014.78.2. – ISSN 1529–6466

[83] Dau, Holger ; Liebisch, Peter ; Haumann, Michael: X-ray absorption spectroscopy to analyze nuclear geometry and electronic structure of biological metal centers?potential and questions examined with special focus on the tetranuclear manganese complex of oxygenic photosynthesis. In: Analytical and Bioanalytical Chemistry 376 (2003), jul, Nr. 5, 562–583. http://dx.doi.org/10.1007/s00216-003-1982-2. – DOI 10.1007/s00216–003–1982–2. – ISSN 1618–2642

[84] Zaharieva, I. ; González-Flores, D. ; Asfari, B. ; Pasquini, C. ; Mohammadi, M. R. ; Klingan, K. ; Zizak, I. ; Loos, S. ; Chernev, P. ; Dau, H.: Water oxidation catalysis – role of redox and structural dynamics in biological photosynthesis and inorganic manganese oxides. In: Energy & Environmental Science 9 (2016), Nr. 7, 2433–2443. http://dx.doi.org/10.1039/C6EE01222A. – DOI 10.1039/C6EE01222A. – ISSN 1754–5692

[85] Meschede, Dieter: Gerthsen Physik. 23. Berlin : Springer, 2005 https://www.bibsonomy.org/bibtex/2a7f97728143e4634cee40eed3a2d2ab4/two. – ISBN 978–3–642–12893–8

[86] Baer, Donald R. ; Artyushkova, Kateryna ; Richard Brundle, Christopher ; Castle, James E. ; Engelhard, Mark H. ; Gaskell, Karen J. ; Grant, John T. ; Haasch, Richard T. ; Linford, Matthew R. ; Powell, Cedric J. ; Shard, Alexander G. ; Sherwood, Peter M. A. ; Smentkowski, Vincent S.: Practical guides for x-ray photoelectron spectroscopy: First steps in planning, conducting, and reporting XPS measurements. In: Journal of Vacuum Science & Technology A 37 (2019), may, Nr. 3, 031401. http://dx.doi.org/10.1116/1.5065501. – DOI 10.1116/1.5065501. – ISSN 0734–2101

[87] Vesborg, Peter C. ; Jaramillo, Thomas F.: Addressing the terawatt challenge: Scalability in the supply of chemical elements for renewable energy. In: RSC Advances 2 (2012), Nr. 21, S. 7933–7947. http://dx.doi.org/10.1039/c2ra20839c. – DOI 10.1039/c2ra20839c. – ISSN 20462069

[88] Schlögl, Robert: Sustainable Energy Systems: The Strategic Role of Chemical Energy Conversion. In: Topics in Catalysis 59 (2016), may, Nr. 8-9, 772–786. http://dx.doi.org/10.1007/s11244-016-0551-9. – DOI 10.1007/s11244–016–0551–9. – ISSN 1022–5528

[89] Dufo-López, Rodolfo ; Bernal-Agustín, José L. ; Contreras, Javier: Optimization of control strategies for stand-alone renewable energy systems with hydrogen storage. In: Renewable Energy 32 (2007), jun, Nr. 7, 1102–1126. http://dx.doi.org/10.1016/j.renene.2006.04.013. – DOI 10.1016/j.renene.2006.04.013. – ISSN 09601481

[90] Qi, Jing ; Zhang, Wei ; Cao, Rui: Solar-to-Hydrogen Energy Conversion Based on Water Splitting. In: Advanced Energy Materials 8 (2018), feb, Nr. 5, 1701620. http://dx.doi.org/10.1002/aenm.201701620. – DOI 10.1002/aenm.201701620. – ISSN 16146832

[91] Weibel, A. ; Bouchet, R. ; Boulc'h, F. ; Knauth, P.: The big problem of small particles: A comparison of methods for determination of particle size in nanocrystalline anatase powders. In: Chemistry of Materials 17 (2005), Nr. 9, S. 2378–2385. http://dx.doi.org/10.1021/cm0403762. – DOI 10.1021/cm0403762. – ISSN 08974756

[92] Akimoto, Junji ; Takahashi, Yasuhiko ; Gotoh, Yoshito ; Mizuta, Susumu: Single Crystal X-ray Diffraction Study of the Spinel-type LiMn 2 O 4. In: Chemistry of Materials 12 (2000), nov, Nr. 11, 3246–3248. http://dx.doi.org/10.1021/cm0003673. – DOI 10.1021/cm0003673. – ISSN 0897–4756

[93] Thackeray, MM ; Kock, A de ; David, W.I.F.: Synthesis and structural characterization of defect spinels in the lithium-manganese-oxide system. In: Materials Research Bulletin 28 (1993), oct, Nr. 10, 1041–1049. http://dx.doi.org/10.1016/0025-5408(93)90142-Z. – DOI 10.1016/0025–5408(93)90142–Z. – ISSN 00255408

[94] Strobel, P. ; Le Cras, F. ; Seguin, L. ; Anne, M. ; Tarascon, J.M.: Oxygen Nonstoichiometry in Li–Mn–O Spinel Oxides: A Powder Neutron Diffraction Study.

In: Journal of Solid State Chemistry 135 (1998), jan, Nr. 1, 132–139. http://dx.doi.org/10.1006/jssc.1997.7611. – DOI 10.1006/jssc.1997.7611. – ISSN 00224596

[95] Karim, Altaf ; Fosse, Sonia ; Persson, Kristin A.: Surface structure and equilibrium particle shape of the LiMn 2O4 spinel from first-principles calculations. In: Physical Review B - Condensed Matter and Materials Physics 87 (2013), Nr. 7, S. 25–28. http://dx.doi.org/10.1103/PhysRevB.87.075322. – DOI 10.1103/PhysRevB.87.075322. – ISSN 10980121

[96] Kölbach, Moritz ; Fiechter, Sebastian ; Krol, Roel van d. ; Bogdanoff, Peter: Evaluation of electrodeposited α-Mn 2 O 3 as a catalyst for the oxygen evolution reaction. In: Catalysis Today 290 (2017), jul, 2–9. http://dx.doi.org/10.1016/j.cattod.2017.03.030. – DOI 10.1016/j.cattod.2017.03.030. – ISSN 09205861

[97] Vesztergom, Soma ; Barankai, Norbert ; Kovács, N. ; Ujvári, M. ; Broekmann, Peter ; Siegenthaler, Hans ; Láng, G.G.: Electrical cross-talk in rotating ring–disk experiments. In: Electrochemistry Communications 68 (2016), jul, Nr. 11, 54–58. http://dx.doi.org/10.1016/j.elecom.2016.04.012. – DOI 10.1016/j.elecom.2016.04.012. – ISSN 13882481

[98] Gao, Qiang ; Ranjan, Chinmoy ; Pavlovic, Zoran ; Blume, Raoul ; Schlögl, Robert: Enhancement of Stability and Activity of MnO x /Au Electrocatalysts for Oxygen Evolution through Adequate Electrolyte Composition. In: ACS Catalysis 5 (2015), dec, Nr. 12, 7265–7275. http://dx.doi.org/10.1021/acscatal.5b01632. – DOI 10.1021/acscatal.5b01632. – ISSN 2155–5435

[99] Risch, Marcel ; Grimaud, Alexis ; May, Kevin J. ; Stoerzinger, Kelsey A. ; Chen, Tina J. ; Mansour, Azzam N. ; Shao-Horn, Yang: Structural Changes of Cobalt-Based Perovskites upon Water Oxidation Investigated by EXAFS. In: The Journal of Physical Chemistry C 117 (2013), may, Nr. 17, 8628–8635. http://dx.doi.org/10.1021/jp3126768. – DOI 10.1021/jp3126768. – ISSN 1932–7447

[100] May, Kevin J. ; Carlton, Christopher E. ; Stoerzinger, Kelsey A. ; Risch, Marcel ; Suntivich, Jin ; Lee, Yueh-Lin ; Grimaud, Alexis ; Shao-Horn, Yang: Influence of Oxygen Evolution during Water Oxidation on the Surface of Perovskite Oxide Catalysts. In: The Journal of Physical Chemistry Letters 3

(2012), nov, Nr. 22, 3264–3270. http://dx.doi.org/10.1021/jz301414z. – DOI 10.1021/jz301414z. – ISSN 1948–7185

[101] Han, Binghong ; Risch, Marcel ; Lee, Yueh-Lin ; Ling, Chen ; Jia, Hongfei ; Shao-Horn, Yang: Activity and stability trends of perovskite oxides for oxygen evolution catalysis at neutral pH. In: Physical Chemistry Chemical Physics 17 (2015), Nr. 35, 22576–22580. http://dx.doi.org/10.1039/C5CP04248H. – DOI 10.1039/C5CP04248H. – ISSN 1463–9076

[102] Hu, Wei ; Wang, Yaqin ; Hu, Xiaohong ; Zhou, Yuanquan ; Chen, Shengli: Three-dimensional ordered macroporous IrO2 as electrocatalyst for oxygen evolution reaction in acidic medium. In: Journal of Materials Chemistry 22 (2012), Nr. 13, S. 6010–6016. http://dx.doi.org/10.1039/c2jm16506f. – DOI 10.1039/c2jm16506f. – ISSN 13645501

[103] Frydendal, Rasmus ; Paoli, Elisa A. ; Knudsen, Brian P. ; Wickman, Björn ; Malacrida, Paolo ; Stephens, Ifan E. ; Chorkendorff, Ib: Benchmarking the Stability of Oxygen Evolution Reaction Catalysts: The Importance of Monitoring Mass Losses. In: ChemElectroChem 1 (2014), Nr. 12, S. 2075–2081. http://dx.doi.org/10.1002/celc.201402262. – DOI 10.1002/celc.201402262. – ISSN 21960216

[104] Jung, Jae-Il ; Risch, Marcel ; Park, Seungkyu ; Kim, Min G. ; Nam, Gyutae ; Jeong, Hu-Young ; Shao-Horn, Yang ; Cho, Jaephil: Optimizing nanoparticle perovskite for bifunctional oxygen electrocatalysis. In: Energy & Environmental Science 9 (2016), Nr. 1, 176–183. http://dx.doi.org/10.1039/C5EE03124A. – DOI 10.1039/C5EE03124A. – ISSN 1754–5692

[105] Wang, Jiangwei ; Fan, Feifei ; Liu, Yang ; Jungjohann, Katherine L. ; Lee, Seung W. ; Mao, Scott X. ; Liu, Xiaohua ; Zhu, Ting: Structural Evolution and Pulverization of Tin Nanoparticles during Lithiation-Delithiation Cycling. In: Journal of The Electrochemical Society 161 (2014), Nr. 11, S. F3019–F3024. http://dx.doi.org/10.1149/2.0041411jes. – DOI 10.1149/2.0041411jes. – ISSN 0013–4651

[106] Trócoli, Rafael ; Erinmwingbovo, Collins ; La Mantia, Fabio: Optimized Lithium Recovery from Brines by using an Electrochemical Ion-Pumping Process Based on λ-MnO 2 and Nickel Hexacyanoferrate. In: ChemElectroChem 4

(2017), Nr. 1, S. 143–149. http://dx.doi.org/10.1002/celc.201600509. – DOI 10.1002/celc.201600509. – ISSN 21960216

[107] Suntivich, Jin ; Gasteiger, Hubert A. ; Yabuuchi, Naoaki ; Shao-Horn, Yang: Electrocatalytic Measurement Methodology of Oxide Catalysts Using a Thin-Film Rotating Disk Electrode. In: Journal of The Electrochemical Society 157 (2010), Nr. 8, B1263. http://dx.doi.org/10.1149/1.3456630. – DOI 10.1149/1.3456630. – ISSN 00134651

[108] Trasatti, Sergio ; Petrii, O.A.: Real surface area measurements in electrochemistry. In: Journal of Electroanalytical Chemistry 327 (1992), jun, Nr. 1-2, 353–376. http://dx.doi.org/10.1016/0022-0728(92)80162-W. – DOI 10.1016/0022–0728(92)80162–W. – ISSN 15726657

[109] Kim, Haegyeom ; Hong, Jihyun ; Park, Kyu-Young ; Kim, Hyungsub ; Kim, Sung-Wook ; Kang, Kisuk: Aqueous Rechargeable Li and Na Ion Batteries. In: Chemical Reviews 114 (2014), Nr. 23, S. 11788–11827. http://dx.doi.org/10.1021/cr500232y. – DOI 10.1021/cr500232y. – ISSN 0009–2665

[110] Kanoh, Hirofumi ; Tang, Weiping ; Makita, Yoji ; Ooi, Kenta: Electrochemical Intercalation of Alkali-Metal Ions into Birnessite-Type Manganese Oxide in Aqueous Solution. In: Langmuir 13 (2002), Nr. 25, S. 6845–6849. http://dx.doi.org/10.1021/la970767d. – DOI 10.1021/la970767d. – ISSN 0743–7463

[111] Jayalakshmi, M. ; Rao, M. M. ; Scholz, F.: Electrochemical behavior of solid lithium manganate (LiMn2O4) in aqueous neutral electrolyte solutions. In: Langmuir 19 (2003), Nr. 20, S. 8403–8408. http://dx.doi.org/10.1021/la0340448. – DOI 10.1021/la0340448. – ISSN 07437463

[112] Hasan, Mohammed F. ; Chen, Chien-Fan ; Shaffer, Christian E. ; Mukherjee, Partha P.: Analysis of the Implications of Rapid Charging on Lithium-Ion Battery Performance. In: Journal of The Electrochemical Society 162 (2015), Nr. 7, S. A1382–A1395. http://dx.doi.org/10.1149/2.0871507jes. – DOI 10.1149/2.0871507jes. – ISSN 0013–4651

[113] Kheirmand, Mehdi ; Ghasemi, Abdolmajid: LiMn2O4 nanoparticles as cathode in aqueous lithium-ion battery. In: Surface Engineering and Applied Electrochemistry 52 (2016), Nr. 5, S. 480–486. http://dx.doi.org/10.3103/s1068375516050069. – DOI 10.3103/s1068375516050069. – ISSN 1068–3755

[114] Tang, W. ; Tian, S. ; Liu, L.L. ; Li, L. ; Zhang, H.P. ; Yue, Y.B. ; Bai, Y. ; Wu, Y.P. ; Zhu, K.: Nanochain LiMn2O4 as ultra-fast cathode material for aqueous rechargeable lithium batteries. In: Electrochemistry Communications 13 (2011), feb, Nr. 2, 205–208. http://dx.doi.org/10.1016/j.elecom.2010.12.015. – DOI 10.1016/j.elecom.2010.12.015. – ISSN 13882481

[115] Ruffo, Riccardo ; Wessells, Colin ; Huggins, Robert A. ; Cui, Yi: Electrochemical behavior of LiCoO2 as aqueous lithium-ion battery electrodes. In: Electrochemistry Communications 11 (2009), Nr. 2, 247–249. http://dx.doi.org/10.1016/j.elecom.2008.11.015. – DOI 10.1016/j.elecom.2008.11.015. – ISSN 13882481

[116] Koningsberger, D C. ; Mojet, B L. ; Dorssen, G E. ; Ramaker, D E.: XAFS spectroscopy; fundamental principles and data analysis. In: Topics In Catalysis 10 (2000), Nr. 3-4, S. 143–155

[117] George, G. N. ; Hedman, B. ; Hodgson, K. O.: An edge with XAS. In: Nature Structural Biology 5 (1998), Nr. 8 SUPPL., S. 645–647. http://dx.doi.org/10.1038/1336. – DOI 10.1038/1336. – ISSN 10728368

[118] Henke, B.L. ; Gullikson, E.M. ; Davis, J.C.: X-Ray Interactions: Photoabsorption, Scattering, Transmission, and Reflection at E = 50-30,000 eV, Z = 1-92. In: Atomic Data and Nuclear Data Tables 54 (1993), jul, Nr. 2, 181–342. http://dx.doi.org/10.1006/adnd.1993.1013. – DOI 10.1006/adnd.1993.1013. – ISSN 0092640X

[119] Gilbert, B. ; Frazer, B. H. ; Belz, A. ; Conrad, P. G. ; Nealson, K. H. ; Haskel, D. ; Lang, J. C. ; Srajer, G. ; De Stasio, G.: Multiple scattering calculations of bonding and X-ray absorption spectroscopy of manganese oxides. In: Journal of Physical Chemistry A 107 (2003), Nr. 16, S. 2839–2847. http://dx.doi.org/10.1021/jp021493s. – DOI 10.1021/jp021493s. – ISSN 10895639

[120] Zaharieva, Ivelina ; Chernev, Petko ; Risch, Marcel ; Klingan, Katharina ; Kohlhoff, Mike ; Fischer, Anna ; Dau, Holger: Electrosynthesis, functional, and structural characterization of a water-oxidizing manganese oxide. In: Energy & Environmental Science 5 (2012), Nr. 5, 7081–7089. http://dx.doi.org/10.1039/c2ee21191b. – DOI 10.1039/c2ee21191b. – ISSN 1754–5692

[121] Zaharieva, I. ; Chernev, P. ; Risch, M. ; Gerencser, L. ; Berggren, G. ; Shevchenko, D. ; Anderlund, M. ; Weng, T. C. ; Haumann, M. ; Dau, H.: Towards a comprehensive X-ray approach for studying the photosynthetic manganese complex–XANES, Kα/Kβ/Kβ-satellite emission lines, RIXS, and comparative computational approaches for selected model complexes. In: Journal of Physics: Conference Series 190 (2009), nov, 012142. http://dx.doi.org/10.1088/1742-6596/190/1/012142. – DOI 10.1088/1742–6596/190/1/012142. – ISSN 1742–6596

[122] Schlörb, H. ; Bungs, M. ; Plieth, W.: Synthesis and electrochemical studies of manganese oxides with spinel structure in aqueous electrolyte (9 M KOH). In: Electrochimica Acta 42 (1997), Nr. 17, S. 2619–2625. http://dx.doi.org/10.1016/S0013-4686(96)00445-8. – DOI 10.1016/S0013–4686(96)00445–8. – ISSN 00134686

[123] Christensen, Rune ; Hansen, Heine A. ; Dickens, Colin F. ; Nørskov, Jens K. ; Vegge, Tejs: Functional Independent Scaling Relation for ORR/OER Catalysts. In: Journal of Physical Chemistry C 120 (2016), Nr. 43, S. 24910–24916. http://dx.doi.org/10.1021/acs.jpcc.6b09141. – DOI 10.1021/acs.jpcc.6b09141. – ISSN 19327455

[124] Urbansky, Edward T. ; Schock, Michael R.: Understanding, Deriving, and Computing Buffer Capacity. In: Journal of Chemical Education 77 (2009), Nr. 12, S. 1640–1644. http://dx.doi.org/10.1021/ed077p1640. – DOI 10.1021/ed077p1640. – ISSN 0021–9584

[125] Licht, Stuart: pH Measurement in Concentrated Alkaline Solutions. In: Analytical Chemistry 57 (1985), Nr. 2, S. 514–519. http://dx.doi.org/10.1021/ac50001a045. – DOI 10.1021/ac50001a045. – ISSN 15206882

[126] Elliot, A.John ; Chenier, Monique P. ; Ouellette, Denis C.: Solubilities of hydrogen and oxygen in concentrated lithium salt solutions. In: Fusion Engineering and Design 13 (1990), aug, Nr. 1, 29–31. http://dx.doi.org/10.1016/0920-3796(90)90029-6. – DOI 10.1016/0920–3796(90)90029–6. – ISSN 09203796

[127] Giordano, Livia ; Han, Binghong ; Risch, Marcel ; Hong, Wesley T. ; Rao, Reshma R. ; Stoerzinger, Kelsey A. ; Shao-Horn, Yang: pH dependence of

OER activity of oxides: Current and future perspectives. In: Catalysis Today 262 (2016), mar, 2–10. http://dx.doi.org/10.1016/j.cattod.2015.10.006. – DOI 10.1016/j.cattod.2015.10.006. – ISSN 09205861

[128] Grimaud, Alexis ; Diaz-Morales, Oscar ; Han, Binghong ; Hong, Wesley T. ; Lee, Yueh L. ; Giordano, Livia ; Stoerzinger, Kelsey A. ; Koper, Marc T. ; Shao-Horn, Yang: Activating lattice oxygen redox reactions in metal oxides to catalyse oxygen evolution. In: Nature Chemistry 9 (2017), Nr. 5, 457–465. http://dx.doi.org/10.1038/nchem.2695. – DOI 10.1038/nchem.2695. – ISSN 17554349

[129] Yang, Chunzhen ; Batuk, Maria ; Jacquet, Quentin ; Rousse, Gwenaëlle ; Yin, Wei ; Zhang, Leiting ; Hadermann, Joke ; Abakumov, Artem M. ; Cibin, Giannantonio ; Chadwick, Alan ; Tarascon, Jean M. ; Grimaud, Alexis: Revealing pH-Dependent Activities and Surface Instabilities for Ni-Based Electrocatalysts during the Oxygen Evolution Reaction. In: ACS Energy Letters 3 (2018), Nr. 12, S. 2884–2890. http://dx.doi.org/10.1021/acsenergylett.8b01818. – DOI 10.1021/acsenergylett.8b01818. – ISSN 23808195

[130] Stoerzinger, Kelsey A. ; Rao, Reshma R. ; Wang, Xiao R. ; Hong, Wesley T. ; Rouleau, Christopher M. ; Shao-Horn, Yang: The Role of Ru Redox in pH-Dependent Oxygen Evolution on Rutile Ruthenium Dioxide Surfaces. In: Chem 2 (2017), Nr. 5, S. 668–675. http://dx.doi.org/10.1016/j.chempr.2017.04.001. – DOI 10.1016/j.chempr.2017.04.001. – ISSN 24519294

[131] Ohzuku, Tsutomu: Electrochemistry of Manganese Dioxide in Lithium Nonaqueous Cell. In: Journal of The Electrochemical Society 137 (1990), Nr. 3, 769. http://dx.doi.org/10.1149/1.2086552. – DOI 10.1149/1.2086552. – ISSN 00134651

[132] Koper, Marc T.: Thermodynamic theory of multi-electron transfer reactions: Implications for electrocatalysis. In: Journal of Electroanalytical Chemistry 660 (2011), sep, Nr. 2, 254–260. http://dx.doi.org/10.1016/j.jelechem.2010.10.004. – DOI 10.1016/j.jelechem.2010.10.004. – ISSN 15726657

[133] Nicholson, Richard S.: Theory and Application of Cyclic Voltammetry for Measurement of Electrode Reaction Kinetics. In: Analytical Chemistry 37

(1965), Nr. 11, S. 1351–1355. http://dx.doi.org/10.1021/ac60230a016. – DOI 10.1021/ac60230a016. – ISSN 15206882

[134] Rehr, J. J. ; Albers, R. C.: Theoretical approaches to x-ray absorption fine structure. In: Reviews of Modern Physics 72 (2000), jul, Nr. 3, 621–654. http://dx.doi.org/10.1103/RevModPhys.72.621. – DOI 10.1103/RevModPhys.72.621. – ISSN 0034–6861

[135] Henderson, G. S. ; Groot, F. M. F. ; Moulton, B. J. A.: X-ray Absorption Near-Edge Structure (XANES) Spectroscopy. In: Reviews in Mineralogy and Geochemistry 78 (2014), jan, Nr. 1, 75–138. http://dx.doi.org/10.2138/rmg.2014.78.3. – DOI 10.2138/rmg.2014.78.3. – ISSN 1529–6466

[136] Pfalzer, P. ; Urbach, J. P. ; Klemm, M. ; Horn, S. ; Den Boer, Marten L. ; Frenkel, Anatoly I. ; Kirkland, J. P.: Elimination of self-absorption in fluorescence hard-x-ray absorption spectra. In: Physical Review B - Condensed Matter and Materials Physics 60 (1999), Nr. 13, S. 9335–9339. http://dx.doi.org/10.1103/PhysRevB.60.9335. – DOI 10.1103/PhysRevB.60.9335. – ISSN 1550235X

[137] Booth, C. H. ; Bridges, F.: Improved self-absorption correction for fluorescence measurements of extended x-ray absorption fine-structure. (2003), jun, 8–11. http://arxiv.org/abs/cond-mat/0306252

[138] Risch, Marcel ; Stoerzinger, Kelsey A. ; Han, Binghong ; Regier, Tom Z. ; Peak, Derek ; Sayed, Sayed Y. ; Wei, Chao ; Xu, Zhichuan ; Shao-Horn, Yang: Redox Processes of Manganese Oxide in Catalyzing Oxygen Evolution and Reduction: An in Situ Soft X-ray Absorption Spectroscopy Study. In: Journal of Physical Chemistry C 121 (2017), Nr. 33, S. 17682–17692. http://dx.doi.org/10.1021/acs.jpcc.7b05592. – DOI 10.1021/acs.jpcc.7b05592. – ISSN 19327455

[139] Tesch, Marc F. ; Bonke, Shannon A. ; Jones, Travis E. ; Shaker, Maryam N. ; Xiao, Jie ; Skorupska, Katarzyna ; Mom, Rik ; Melder, Jens ; Kurz, Philipp ; Knop-Gericke, Axel ; Schlögl, Robert ; Hocking, Rosalie K. ; Simonov, Alexandr N.: Evolution of Oxygen–Metal Electron Transfer and Metal Electronic States During Manganese Oxide Catalyzed Water Oxidation Revealed with In Situ Soft X-Ray Spectroscopy. In: Angewandte Chemie - International Edition 58 (2019), Nr. 11, S. 3426–3432. http://dx.doi.org/10.1002/anie.201810825. – DOI 10.1002/anie.201810825. – ISSN 15213773

[140] Huynh, Michael ; Shi, Chenyang ; Billinge, Simon J. ; Nocera, Daniel G.: Nature of Activated Manganese Oxide for Oxygen Evolution. In: Journal of the American Chemical Society 137 (2015), Nr. 47, S. 14887–14904. http://dx.doi.org/10.1021/jacs.5b06382. – DOI 10.1021/jacs.5b06382. – ISSN 15205126

[141] Xi, Lifei ; Schwanke, Christoph ; Xiao, Jie ; Abdi, Fatwa F. ; Zaharieva, Ivelina ; Lange, Kathrin M.: In Situ L-Edge XAS Study of a Manganese Oxide Water Oxidation Catalyst. In: Journal of Physical Chemistry C 121 (2017), Nr. 22, S. 12003–12009. http://dx.doi.org/10.1021/acs.jpcc.7b02331. – DOI 10.1021/acs.jpcc.7b02331. – ISSN 19327455

[142] Sherman, David M.: The electronic structures of manganese oxide minerals. In: American Mineralogist 69 (1984), aug, Nr. 7-8, S. 788–799. – ISSN 0003–004X

[143] Ebrahimizadeh Abrishami, Majid ; Risch, Marcel ; Scholz, Julius ; Roddatis, Vladimir ; Osterthun, Norbert ; Jooss, Christian: Oxygen Evolution at Manganite Perovskite Ruddlesden-Popper Type Particles: Trends of Activity on Structure, Valence and Covalence. In: Materials 9 (2016), nov, Nr. 11, 921. http://dx.doi.org/10.3390/ma9110921. – DOI 10.3390/ma9110921. – ISSN 1996–1944

[144] Khan, Munirah ; Xiao, Jie ; Zhou, Fengling ; Yablonskikh, Mikhail ; MacFarlane, Douglas R. ; Spiccia, Leone ; Aziz, Emad F.: On the Origin of the Improvement of Electrodeposited MnO x Films in Water Oxidation Catalysis Induced by Heat Treatment. In: ChemSusChem 8 (2015), jun, Nr. 11, 1980–1985. http://dx.doi.org/10.1002/cssc.201500330. – DOI 10.1002/cssc.201500330. – ISSN 18645631

[145] Khan, Munirah ; Suljoti, Edlira ; Singh, Archana ; Bonke, Shannon A. ; Brandenburg, Tim ; Atak, Kaan ; Golnak, Ronny ; Spiccia, Leone ; Aziz, Emad F.: Electronic structural insights into efficient MnOx catalysts. In: Journal of Materials Chemistry A 2 (2014), Nr. 43, S. 18199–18203. http://dx.doi.org/10.1039/c4ta04185b. – DOI 10.1039/c4ta04185b. – ISSN 20507496

[146] Huynh, Michael ; Bediako, D. K. ; Liu, Yi ; Nocera, Daniel G.: Nucleation and growth mechanisms of an electrodeposited manganese oxide oxygen evolution catalyst. In: Journal of Physical Chemistry C 118 (2014), Nr. 30, S. 17142–

17152. http://dx.doi.org/10.1021/jp501768n. – DOI 10.1021/jp501768n. – ISSN 19327455

[147] Hong, Wesley T. ; Welsch, Roy E. ; Shao-Horn, Yang: Descriptors of Oxygen-Evolution Activity for Oxides: A Statistical Evaluation. In: Journal of Physical Chemistry C 120 (2016), Nr. 1, S. 78–86. http://dx.doi.org/10.1021/acs.jpcc.5b10071. – DOI 10.1021/acs.jpcc.5b10071. – ISSN 19327455

[148] Raabe, Stephanie ; Mierwaldt, Daniel ; Ciston, Jim ; Uijttewaal, Matthé ; Stein, Helge ; Hoffmann, Jörg ; Zhu, Yimei ; Blöchl, Peter ; Jooss, Christian: In situ electrochemical electron microscopy study of oxygen evolution activity of doped manganite perovskites. In: Advanced Functional Materials 22 (2012), Nr. 16, S. 3378–3388. http://dx.doi.org/10.1002/adfm.201103173. – DOI 10.1002/adfm.201103173. – ISSN 1616301X

[149] Man, Isabela C. ; Su, Hai Y. ; Calle-Vallejo, Federico ; Hansen, Heine A. ; Martínez, José I. ; Inoglu, Nilay G. ; Kitchin, John ; Jaramillo, Thomas F. ; Nørskov, Jens K. ; Rossmeisl, Jan: Universality in Oxygen Evolution Electrocatalysis on Oxide Surfaces. In: ChemCatChem 3 (2011), Nr. 7, S. 1159–1165. http://dx.doi.org/10.1002/cctc.201000397. – DOI 10.1002/cctc.201000397. – ISSN 18673880

[150] Koper, Marc T. M.: Volcano Activity Relationships for Proton-Coupled Electron Transfer Reactions in Electrocatalysis. In: Topics in Catalysis 58 (2015), Nr. 18-20, S. 1153–1158. http://dx.doi.org/10.1007/s11244-015-0489-3. – DOI 10.1007/s11244–015–0489–3. – ISBN 1124401504

[151] Su, Hai Y. ; Gorlin, Yelena ; Man, Isabela C. ; Calle-Vallejo, Federico ; Norskov, Jens K. ; Jaramillo, Thomas F. ; Rossmeisl, Jan: Identifying active surface phases for metal oxide electrocatalysts: A study of manganese oxide bifunctional catalysts for oxygen reduction and water oxidation catalysis. In: Physical Chemistry Chemical Physics 14 (2012), Nr. 40, S. 14010–14022. http://dx.doi.org/10.1039/c2cp40841d. – DOI 10.1039/c2cp40841d. – ISSN 14639076

[152] Pourbaix, Marcel: Atlas of electrochemical equilibria in aqueous solutions. In: Houston, Tex. : National Association of Corrosion Engineers 2 (1974)

[153] Gorlin, Yelena ; Lassalle-Kaiser, Benedikt ; Benck, Jesse D. ; Gul, Sheraz ; Webb, Samuel M. ; Yachandra, Vittal K. ; Yano, Junko ; Jaramillo,

Thomas F.: In Situ X-ray Absorption Spectroscopy Investigation of a Bifunctional Manganese Oxide Catalyst with High Activity for Electrochemical Water Oxidation and Oxygen Reduction. In: Journal of the American Chemical Society 135 (2013), jun, Nr. 23, 8525–8534. http://dx.doi.org/10.1021/ja3104632. – DOI 10.1021/ja3104632. – ISSN 0002–7863

[154] Van Oversteeg, Christina H. ; Doan, Hoang Q. ; De Groot, Frank M. ; Cuk, Tanja: In situ X-ray absorption spectroscopy of transition metal based water oxidation catalysts. In: Chemical Society Reviews 46 (2017), Nr. 1, S. 102–125. http://dx.doi.org/10.1039/c6cs00230g. – DOI 10.1039/c6cs00230g. – ISSN 14604744

[155] Jin, Kyoungsuk ; Seo, Hongmin ; Hayashi, Toru ; Balamurugan, Mani ; Jeong, Donghyuk ; Go, Yoo K. ; Hong, Jung S. ; Cho, Kang H. ; Kakizaki, Hirotaka ; Bonnet-Mercier, Nadège ; Kim, Min G. ; Kim, Sun H. ; Nakamura, Ryuhei ; Nam, Ki T.: Mechanistic Investigation of Water Oxidation Catalyzed by Uniform, Assembled MnO Nanoparticles. In: Journal of the American Chemical Society 139 (2017), feb, Nr. 6, 2277–2285. http://dx.doi.org/10.1021/jacs.6b10657. – DOI 10.1021/jacs.6b10657. – ISSN 0002–7863

[156] Lassalle-Kaiser, Benedikt ; Gul, Sheraz ; Kern, Jan ; Yachandra, Vittal K. ; Yano, Junko: In situ/Operando studies of electrocatalysts using hard X-ray spectroscopy. In: Journal of Electron Spectroscopy and Related Phenomena 221 (2017), nov, 18–27. http://dx.doi.org/10.1016/j.elspec.2017.05.001. – DOI 10.1016/j.elspec.2017.05.001. – ISSN 03682048

[157] Yoshida, Masaaki ; Yomogida, Takumi ; Mineo, Takehiro ; Nitta, Kiyofumi ; Kato, Kazuo ; Masuda, Takuya ; Nitani, Hiroaki ; Abe, Hitoshi ; Takakusagi, Satoru ; Uruga, Tomoya ; Asakura, Kiyotaka ; Uosaki, Kohei ; Kondoh, Hiroshi: In situ observation of carrier transfer in the Mn-oxide/Nb:SrTiO 3 photoelectrode by X-ray absorption spectroscopy. In: Chemical Communications 49 (2013), Nr. 71, S. 7848–7850. http://dx.doi.org/10.1039/c3cc43584a. – DOI 10.1039/c3cc43584a. – ISBN 8145566169

[158] Lima, Fabio H. ; Calegaro, Marcelo L. ; Ticianelli, Edson A.: Electrocatalytic activity of manganese oxides prepared by thermal decomposition for oxygen reduction. In: Electrochimica Acta 52 (2007), mar, Nr. 11, 3732–3738. http://dx.doi.

org/10.1016/j.electacta.2006.10.047. – DOI 10.1016/j.electacta.2006.10.047. – ISSN 00134686

[159] Liu, Yayuan ; Wang, Haotian ; Lin, Dingchang ; Liu, Chong ; Hsu, Po C. ; Liu, Wei ; Chen, Wei ; Cui, Yi: Electrochemical tuning of olivine-type lithium transition-metal phosphates as efficient water oxidation catalysts. In: Energy and Environmental Science 8 (2015), Nr. 6, 1719–1724. http://dx.doi.org/10.1039/c5ee01290b. – DOI 10.1039/c5ee01290b. – ISSN 17545706

[160] Lu, Zhiyi ; Jiang, Kun ; Chen, Guangxu ; Wang, Haotian ; Cui, Yi: Lithium Electrochemical Tuning for Electrocatalysis. In: Advanced Materials 30 (2018), Nr. 48, S. 1–8. http://dx.doi.org/10.1002/adma.201800978. – DOI 10.1002/adma.201800978. – ISSN 15214095

[161] Maiyalagan, Thandavarayan ; Jarvis, Karalee A. ; Therese, Soosairaj ; Ferreira, Paulo J. ; Manthiram, Arumugam: Spinel-type lithium cobalt oxide as a bifunctional electrocatalyst for the oxygen evolution and oxygen reduction reactions. In: Nature Communications 5 (2014), Nr. May, 1–8. http://dx.doi.org/10.1038/ncomms4949. – DOI 10.1038/ncomms4949. – ISSN 20411723

[162] Lu, Zhiyi ; Wang, Haotian ; Kong, Desheng ; Yan, Kai ; Hsu, Po C. ; Zheng, Guangyuan ; Yao, Hongbin ; Liang, Zheng ; Sun, Xiaoming ; Cui, Yi: Electrochemical tuning of layered lithium transition metal oxides for improvement of oxygen evolution reaction. In: Nature Communications 5 (2014), 1–7. http://dx.doi.org/10.1038/ncomms5345. – DOI 10.1038/ncomms5345. – ISSN 20411723

[163] Lee, Seung W. ; Carlton, Christopher ; Risch, Marcel ; Surendranath, Yogesh ; Chen, Shuo ; Furutsuki, Sho ; Yamada, Atsuo ; Nocera, Daniel G. ; Shao-Horn, Yang: The nature of lithium battery materials under oxygen evolution reaction conditions. In: Journal of the American Chemical Society 134 (2012), Nr. 41, S. 16959–16962. http://dx.doi.org/10.1021/ja307814j. – DOI 10.1021/ja307814j. – ISSN 00027863

[164] Beaumont, Simon K.: Soft XAS as an in situ technique for the study of heterogeneous catalysts. In: Physical Chemistry Chemical Physics 22 (2020), Nr. 34, 18747–18756. http://dx.doi.org/10.1039/D0CP00657B. – DOI 10.1039/D0CP00657B. – ISSN 1463–9076

[165] Wei, Chao ; Feng, Zhenxing ; Scherer, Günther G. ; Barber, James ; Shao-Horn, Yang ; Xu, Zhichuan J.: Cations in Octahedral Sites: A Descriptor for Oxygen Electrocatalysis on Transition-Metal Spinels. In: Advanced Materials 29 (2017), Nr. 23, S. 1–8. http://dx.doi.org/10.1002/adma.201606800. – DOI 10.1002/adma.201606800. – ISSN 15214095

[166] Calle-Vallejo, Federico ; Díaz-Morales, Oscar A. ; Kolb, Manuel J. ; Koper, Marc T. M.: Why Is Bulk Thermochemistry a Good Descriptor for the Electrocatalytic Activity of Transition Metal Oxides? In: ACS Catalysis 5 (2015), feb, Nr. 2, 869–873. http://dx.doi.org/10.1021/cs5016657. – DOI 10.1021/cs5016657. – ISSN 2155–5435

[167] Odrobina, Jann ; Scholz, Julius ; Pannwitz, Andrea ; Francàs, Laia ; Dechert, Sebastian ; Llobet, Antoni ; Jooss, Christian ; Meyer, Franc: Backbone Immobilization of the Bis(bipyridyl)pyrazolate Diruthenium Catalyst for Electrochemical Water Oxidation. In: ACS Catalysis 7 (2017), mar, Nr. 3, 2116–2125. http://dx.doi.org/10.1021/acscatal.6b02860. – DOI 10.1021/acscatal.6b02860. – ISSN 2155–5435

[168] Odrobina, Jann ; Scholz, Julius ; Risch, Marcel ; Dechert, Sebastian ; Jooss, Christian ; Meyer, Franc: Chasing the Achilles' Heel in Hybrid Systems of Diruthenium Water Oxidation Catalysts Anchored on Indium Tin Oxide: The Stability of the Anchor. In: ACS Catalysis 7 (2017), sep, Nr. 9, 6235–6244. http://dx.doi.org/10.1021/acscatal.7b01883. – DOI 10.1021/acscatal.7b01883. – ISSN 2155–5435

[169] Rajabi, Sheida ; Ebrahimi, Fatemeh ; Lole, Gaurav ; Odrobina, Jann ; Dechert, Sebastian ; Jooss, Christian ; Meyer, Franc: Water Oxidizing Diruthenium Electrocatalysts Immobilized on Carbon Nanotubes: Effects of the Number and Positioning of Pyrene Anchors. In: ACS Catalysis (2020), sep, 10614–10626. http://dx.doi.org/10.1021/acscatal.0c01577. – DOI 10.1021/acscatal.0c01577. – ISSN 2155–5435

[170] Diaz-Morales, Oscar ; Raaijman, Stefan ; Kortlever, Ruud ; Kooyman, Patricia J. ; Wezendonk, Tim ; Gascon, Jorge ; Fu, W. T. ; Koper, Marc T. M.: Iridium-based double perovskites for efficient water oxidation in acid media. In: Nature Communications 7 (2016), nov, Nr. 1, 12363. http://dx.doi.org/10.1038/ncomms12363. – DOI 10.1038/ncomms12363. – ISSN 2041–1723

[171] Rabe, Martin ; Toparli, Cigdem ; Chen, Ying-Hsuan ; Kasian, Olga ; Mayrhofer, Karl J. J. ; Erbe, Andreas: Alkaline manganese electrochemistry studied by in situ and operando spectroscopic methods – metal dissolution, oxide formation and oxygen evolution. In: Physical Chemistry Chemical Physics 21 (2019), Nr. 20, 10457–10469. http://dx.doi.org/10.1039/C9CP00911F. – DOI 10.1039/C9CP00911F. – ISSN 1463–9076

[172] Siewert, Inke ; Gałęzowska, Joanna: Cobalt Catalyst with a Proton-Responsive Ligand for Water Oxidation. In: Chemistry - A European Journal 21 (2015), feb, Nr. 7, 2780–2784. http://dx.doi.org/10.1002/chem.201405020. – DOI 10.1002/chem.201405020. – ISBN 5513933373

[173] Melder, Jens ; Bogdanoff, Peter ; Zaharieva, Ivelina ; Fiechter, Sebastian ; Dau, Holger ; Kurz, Philipp: Water-Oxidation Electrocatalysis by Manganese Oxides: Syntheses, Electrode Preparations, Electrolytes and Two Fundamental Questions. In: Zeitschrift für Physikalische Chemie 234 (2020), may, Nr. 5, 925–978. http://dx.doi.org/10.1515/zpch-2019-1491. – DOI 10.1515/zpch–2019–1491. – ISSN 2196–7156

[174] Lee, Min-Joon ; Lee, Sanghan ; Oh, Pilgun ; Kim, Youngsik ; Cho, Jaephil: High Performance LiMn 2 O 4 Cathode Materials Grown with Epitaxial Layered Nanostructure for Li-Ion Batteries. In: Nano Letters 14 (2014), feb, Nr. 2, 993–999. http://dx.doi.org/10.1021/nl404430e. – DOI 10.1021/nl404430e. – ISSN 1530–6984

[175] Thackeray, Michael M. ; Kang, Sun H. ; Johnson, Christopher S. ; Vaughey, John T. ; Benedek, Roy ; Hackney, S. A.: Li<inf>2</inf>MnO<inf>3</inf>-stabilized LiMO<inf>2</inf> (M = Mn, Ni, Co) electrodes for lithium-ion batteries. In: Journal of Materials Chemistry 17 (2007), Nr. 30, S. 3112–3125. http://dx.doi.org/10.1039/b702425h. – DOI 10.1039/b702425h. – ISSN 13645501

List of Figures

List of Tables

Author Contributions

The main results of this thesis presented in the chapter 4 and 5 are original research by the author and have been published:

Chapter 4

Influence of particle size on the apparent electrocatalytic activity of $LiMn_2O_4$ for oxygen evolution

Max Baumung, Florian Schönewald, Torben Erichsen, Cynthia A. Volkert and Marcel Risch
Sustainable Energy Fuels, 2019,3, 2218-2226; DOI 10.1039/C8SE00551F

All shown experimental data were collected at the Institute for Materials Physics, University Göttingen. The author contribution of this article is the following:
Pre-characterization of the catalyst's particles by SEM and XRD was performed by author. Additional TEM investigation was performed and associated evaluation by Florian Schönewald, under the supervision of Torben Erichsen. All electrocatalytic experiments were conduced by the author. The manuscript was written by the author in collaboration with Marcel Risch.

Chapter 5

Undesired Bulk Oxidation of $LiMn_2O_4$ Increases Overpotential of Electrocatalytic Water Oxidation in Lithium Hydroxide Electrolyte

Max Baumung, Leon Kollenbach, Lifei Xi and Marcel Risch
ChemPhysChem 2019, 20, 2981. ; DOI 10.1002/cphc.201900601

The electrochatalytic data were collected at the Institute for Materials Physics, University Göttingen by the author and by Leon Kollenbach under the supervision of the author. Besides, synchroton measruements were performed by Lifei Xi at BESSY II, Berlin. The manuscript was written by the author in collaboration with Marcel Risch.

Chapter 6

Oxidation by delithation of a $Li_xMn_2O_4$ model catalyst for the OER causes an increase in the faradaic efficiency concurrenting a decrease in catalytic activty

The experimental results were supported by STEM-EELS data (Fig. 6.5a-c) by Florian Schönewald.

Acknowledgments

This thesis is the result of hard work, chances, passion, patience, friendship, not giving up and support - so I have to thank all the people who shared these extraordinary years with me: motivated me, helped me, worked with me. But some of them have to be mentioned here by name.
First of all, I have to thank Dr. Marcel Risch for giving me the chance to do my PhD in his group, discussed results and plans as well as mentoring me. As his first PhD-student it must have been a new situation for both of us and we have mastered is well. I also like to thank Prof. Cynthia A. Volkert, PhD and Prof. Dr. Sven Schneider for being in my advisory committee. Prof. Dr. Christian Jooß, Prof. Dr. Wolfram Kollatschny, Prof. Dr. Hans-Christian Hofsäss and Prof. Dr. Vasily Moshnyaga for agreeing to be part of the examination board. Christian Jooß has also be thanked for allowing me to be part of his group as well.

Thanks to Torben Erichsen for many coffees, discussions, his expertise, his dark humour and a smooth transition to the next generation of PhD students within the C05 project. He always provides beneficial insights in our project and was a great help to me. I also like to thank my counterpart in the C05 project, Florian Schönewald, for his supporting TEM work.
My fellow PhD-students and friends Birte Kressdorf, Danny Schwarzbach, Daniel Mierwaldt, Frederik Stender, Mona Maaß, Torben Erichsen and Mohsen Satoudeh did a fantastic job in supporting and motivating me. Besides the scientific work, these people were always there when something went wrong or has to be celebrated - thank you for that!
I also have to thank the "second" half of my group located in Berlin. Even separated by a distance of 321 km by car, I got all the needed support and feedback - Dulce, Javier, Denis and Joaquín: spot on, thank you! I like to thank Birte Kressdorf, Niklas Weber, Mona Maaß and Jörg Hoffmann for their time to read this thesis and giving me feedback. Thank you Birte, that you always remind me that not everyone is familiar with my topic, you are great and we should find more slots for coffee!!

Many thanks to all technicians (Karin, Micha, Mike, Frank, Conni, Tobi, Thomas, Denny) for making things possible in the first way. Karin Ahlborn has to be mentioned twice: for all the fast and uncomplicated support and help, as well for coffee breaks and cake, to keep me well prepared for my work in the lab.
I like to thank the CIC energiGUNE, Vitoria-Gasteiz in the Basque Country - especially Nagore Ortiz-Vitoriano and her team: Damien Saurel, Begoña Silván, who allowed us to prepare our beamtime, to get an insight in battery research and for their great hospitality.
I also like to thank my bachelor students Leon, Rajka, Justus, Vanessa for their work.
Many thanks to the co-authors of my publications and for our accomplishments. The organisation of ALBA synchrotron, Spain and BESSY II, Berlin for providing beamtime.
I thank the Deutsche Forschungsgemeinschaft for funding and their financial support of the CRC 1073.
My friends outside of the university many thanks for their motivation and a big *"thank you"* to my family and especially my parents for their support and motivation.

So finally, I like to close this final chapter of this thesis with the phrase I often used in the past years: "Alles wird gut!" and I thank all of you...